From the Institute for Cardiogenetics
at the University of Lübeck
under direction of Prof. Dr. Jeanette Erdmann

Impact of the CAD risk locus 9p21 on vascular calcification – development of an iPSC-based model

Dissertation for Fulfillment of Requirements for the Doctoral Degree
at the University of Lübeck
from the Department of Natural Sciences
submitted by

Anja Trillhaase

from Breitenfelde

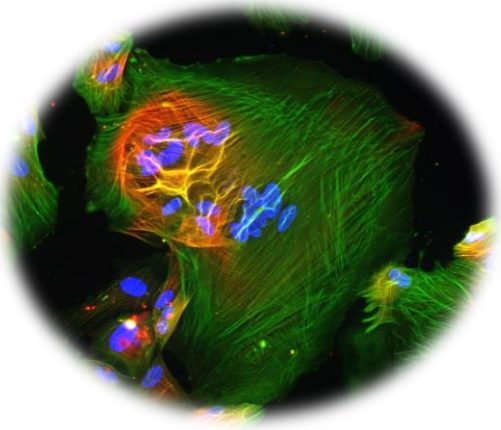

Lübeck, 2020

1. Berichterstatterin: Prof. Dr. rer. nat. J. Erdmann
2. Berichterstatter/In: Prof. Dr. rer. nat. J. Rohwedel
3. Tag der mündlichen Prüfung: 06.10.2020
4. Zum Druck genehmigt: Lübeck, den 07.10.2020

Table of Contents

Acknowledgments

I want to thank many people who supported me or enabled me to accomplish the task of writing this thesis.

First, and foremost, I want to thank **Prof. Dr. Jeanette Erdmann**, for providing me with this fascinating, yet tough project. Even though I struggled a lot, the topic was interesting and challenging on personal as well as professional level. Furthermore, I want to thank you for giving me the opportunity to develop my skills and educate myself in any way I desired.

Further, I want to thank **Dr. Zouhair Aherrahrou** for supervising my progress and for discussing various topics whenever I needed help.

Special thanks go to **Annett Liebers**, **Maren Behrensen**, **Sandra Wrobel**, **Petra Bruse**, **Lisa Paurat**, and **Sabine Stark** for their, sometimes needed, help on carrying out experiments, cell culture maintenance or helpful advice, and some fun time in the lab. I loved the warm and familial atmosphere everywhere and every time, and I'm grateful for the help and advice I received at any time.

I also want to thank **Beatrice Schmidt** for the great time we had together in the iPSC culture and our friendship that build along the way. You supported me when needed and we went through hard times together that I probably would not have pulled through like I did without knowing you where there. Thank you.

Further, I want to thank **Dr. Tobias Reinberger** and **Marlon Märtens** for their great companionship, their assistance and for teaching me to question myself and my work in a critical, scientific way. A thank you also goes to the whole **ICG** team for the familial atmosphere and it has been great working together.

I'd like to thank the **Leducq Consortia CADgenomics** and **PlaqOmics,** as well as the **NCCR** and **DZHK** for integrating me in these extraordinary "families" and providing me with fruitful advice and critically discussing my work.

Finally, I want to thank my **family** who supported my whenever I struggled and who enabled me to accomplish this journey in my life. And finally, thank you to my soon-to-be husband **Stefan** for your love and an open ear, even though you often didn't know what I was talking about. Thank you

List of Figures

List of Tables

Abbreviations

acLDL	acetylated Low-density Lipoprotein
ACS	Acute coronary syndrome
ADAM	a disintegrin and metalloproteinase with thrombospondin motifs family
ADAMTS7	ADAM metallopeptidase with thrombospondin 1 motif 7
AKT	AKT serine/threonine kinase 1
ANG-II	angiotensin II
ANRIL	Antisense non-coding RNA in the INK4/Arf-locus
AP/ALPL	Alkaline phosphatase; biomineralization associated
APS	ammonium persulfate
ARS	Alizarin Red S
bFGF	basic fibroblast growth factor
BMI	Body mass index
BMP2	Bone morphogenic protein 2
BMP4	Bone morphogenic protein 4
bp	basepair
BSA	bovine serum albumin
Ca	Calcium
CaCl2	Calcium chloride
CAD	Coronary artery disease
CALD1	Caldesmon 1
cAMP	3',5'-cyclic adenosine monophosphate
CaP	Calcium phosphate
Cas	CRISPR-associated
CDK	cyclin-dependent kinase
CDKN	cyclin-dependent kinase inhibitor
CDM	chemically defined medium
cDNA	complementary DNA
cGMP	current good manufacturing practice
c-MYC	v-Myc avian myelocytomatosis viral oncogene homolog
CNN1	Calponin 1
CNV	copy number variation
COL1	Collagen 1
CRISPR	clustered regularly interspaced short palindromic repeats
CSF1	colony stimulating factor 1
Cts	threshold cycles
CTSK	cathepsin K
d	day
DAPI	4',6-diamidino-2-phenylindole
DLX5	Distal-less homeobox 5
DMEM	Dulbeccos Modified Eagle's Medium
DMSO	Dimethylsulfoxide

DNA	Deoxyribonucleic acid
dNTPs	2'-Deoxyribonucleosid-5'-triphosphates
DSB	double strand break
DTT	Dithiothreitol
EB	embryoid body
EC	Endothelial cell
ECM	extracellular matrix
EDTA	Ethylenediaminetetraacidic acid
EGF	epidermal growth factor
EM	early mesoderm
ER	endoplasmatic reticulum
ERK	extracellular signal-regulated kinase
ESC	Embryonic stem cell
ESCa	European Society of Cardiology
ESRD	End-stage renal disease
FBS	Fetal bovine serum
FGF2-IS	Fibroblast growth factor 2 - improved sequence
g	gram
GAPDH	glyceraldehyde 3-phosphate dehydrogenase
gRNA	guide RNA
GWAS	Genome-wide association studies
h	hour/s
H2O2	hydrogen peroxide
HASMCs	Human aortic smooth muscle cells
HCl	hydrochloric acid
HR	Homologous recombination
HRP	horseradish-peroxidase
ICM	Inner cell mass
IF	Immunoflurescence staining
IGF	insulin-like growth factor
IMDM	Iscove's Modified Dulbeccos Medium
iPSCs	induced pluripotent stem cells
KI	knock-in
Ki67	(MKI67) Marker of proliferation Ki-67
KLF4	Kruppel-like factor 4
KO	knock-out
L	Litres
L-AP	L-Ascorbic acid phosphate
LDL	low-density lipoprotein
LET-7	lethal-7
LIN28	lin28-homolog A
LM	lateral mesoderm
MEF	mouse embryonic fibroblast
mg	milligramms
MI	Myocardial infarction
mins	minutes

miRNA	micro RNA
mL	millilitre
mM	millimolar
MMPs	Matrix metallproteinases
mRNA	messenger RNA
MTAP	Methylthioadenosine phosphorylase
MYH10	myosin heavxy chain 10
NaCl	Sodium chloride
NANOG	Nanog homeobox
NCBI	National Center of Biotechnology Information
NEAA	Non-essential amino acids
ng	nanogram
NHEJ	non-homologous end joining
nM	nanomolar
nm	nanometer
NPC	Sodium-dependent phosphate cotransporter
NR	Non-risk
O2	oxygen
OCL	Osteocalcin
OCT4	Octamer-binding transcription factor 4
OPN/SSP	Osteopontin/secreted phosphoprotein 1
oxLDL	oxidative low density lipoprotein
P	Phosphate/phosphorus
PAM	protospacer adacent motif
PBS	Phosphate buffered saline
PCR	Polymerase chain reaction
PCs	Pericytes
PDGF-BB	platelet derived growth factor BB
PEO	Pro-epicardial organ
PFA	Paraformaldehyde
PHACTR1	phosphatase and actin regulator 1
PhC	phase contrast
Pi	inorganic phosphate
PIT-1	POU class 1 homeobox 1
PLCγ	phospholipase C gamma
PM	somitic/paraxial mesoderm
PMSF	phenylmethane sulfonyl fluoride
PPi	inorganic pyrophosphate
PSC	Pluripotent stem cell
PVA	Polyvenyl alcohol
PVDF	Polyvinylidene difluoride
qPCR	quantitative PCR
R	risk
RA	Retinoic acid (all trans)
RBP1	retinol binding protein 1
RNA	Ribonucleic acid

ROS	Reactive Oxygen Species
RUNX2	Runt related transcription factor 2
RVD	repeat-variable di-residue
SCAD	Stable CAD
SD	Standard deviation
SDS	sodium dodecyl sulfate
SHF	secondary heart field
SMCs	smooth muscle cells
SMTN	smoothelin
SMαA	smooth muscle alpha actin
SNP	Single nucleotide polymorphism
SOX2	Sex-determining region Y-box 2
SP7	SP7 transcription factor (Osterix)
T	thymidine
TAGLN	transgelin
TALEN	transcription activator-like effector nuclease
TBE	TRIS-Borat-EDTA buffer
TBS	TRIS-buffered saline
TGFβ	Transforming growth factor beta
TNFSF11	TNF superfamily member 11 (RANKL)
TNFα	tumor necrosis factor alpha
TPM4	tropomyosin 4
VIM	vimentin
VSMCs	Vascular smooth muscle cells
WB	Western Blot
Wnt	Wingless-type MMTV integration site family member
WT	wild-type
ZFN	zinc-finger nuclease
β-GP	beta Glycerophosphat
µg	microgram
µL	microlitre
µM	micromolar
µm	micrometer

Abstract

Coronary artery disease (CAD), and one of its basic complications coronary artery calcification (CAC) are still leading causes for death worldwide. Besides environmental risk factors like smoking, lack of exercise and dietary malnutrition, the role of genetics evolved as being an important factor within the last couple of years. Using genome-wide association studies (GWAS) over 160 genetic risk variants were identified to be associated with CAD. One of the risk loci that was identified in the early GWA studies is 9p21. Variants located in this locus were strongly associated with CAD as well as CAC. Interestingly, the 9p21 risk region does not contain protein coding genes, but an antisense RNA known as antisense non-coding RNA in the INK4 locus (ANRIL).

In order to investigate the influence of the 9p21 risk locus on CAC an induced-pluripotent stem cell (iPSC)-based approach was established at the Institute for Cardiogenetics to perform and examine vascular calcification under the influence of the 9p21 risk region. Human iPSCs of healthy (nonrisk, NR) and 9p21 risk (R) patients each containing (WT) or lacking (KO) the 9p21 risk interval were used to differentiate into vascular smooth muscle cells (VSMCs) following an origin-specific differentiation protocol. The iPSCs used for the differentiation as well as the resulting VSMCs were checked for various characteristics such as morphology, marker expression on RNA level as well as protein expression and localization. All those characteristics did not show differences in the absence or presence of the 9p21 risk variants. Therefore, we concluded that the 9p21 risk locus does not have an influence on cell identity or differentiation efficiency. However, when looking at VSMC behavior such as proliferation and migration, we observed higher proliferation rates and higher migration rates in 9p21 R cells. These results reflect, what was published recently. Therefore, we are able to confirm these previously published results, and the protocol works fine in our hands too. For the calcification we were able to show that NR WT cells did not calcify while NR KO as well as R WT and R KO showed positive calcification stainings and a rather increased expression of calcification markers even though biological replicates showed high variations within and in between experiments. We therefore concluded that the absence of or variants within the 9p21 risk locus trigger calcification in VSMCs. Concluding, patients carrying variants in the 9p21 locus are of higher risk of suffering from CAC.

Zusammenfassung

Die koronare Herzkrankheit (KHK) und eine ihrer hauptsächlichen Grunderkrankungen, die koronare Arterienverkalkung (KAV), sind noch immer die Haupttodesursachen weltweit. Neben klassischen Risikofaktoren wie Rauchen, Bewegungsmangel und falscher Ernährung rückt auch die Genetik in den vergangenen Jahren immer weiter in den Fokus. Mithilfe sogenannter Genomweiter Assoziationsstudien (GWAS) wurden bis heute etwa 200 genetische Risikovarianten entdeckt, die mit KHK assoziiert sind. Einer der ersten Loci der in den GWA Studien entdeckt wurde ist 9p21. Genetische Varianten in diesem Locus sind sehr stark sowohl mit KHK als auch mit KAV assoziiert. Interessant an diesem Lokus ist, dass sich im Risikobereich keine protein-kodierenden Gene befinden, sondern nur eine Anti-sense RNA, bekannt als “antisense non-coding RNA in the INK4 locus” (ANRIL).

Um den Einfluss des 9p21 Risikolocus auf die KAV zu untersuchen wurde im Institut für Kardiogenetik ein induziert-pluripotentes Stammzellmodell (iPSZ) entwickelt, mit dem die vaskuläre Verkalkung unter Einfluss des 9p21 Locus untersucht werden sollte. Humane iPSZs eines gesunden (Nicht-Risiko, NR) Spenders und eines Patienten mit Risikovarianten im 9p21 Locus (R) sowohl mit (WT) als auch ohne (KO) den entsprechenden Risikobereich wurden in vaskuläre glatte Muskelzellen (VGMZs) differenziert. Dafür wurde ein linienspezifisches Protokoll verwendet, um nur VGMZs einer bestimmten embryologischen Herkunft zu generieren. Sowohl die iPSZs als auch die VGMZs wurden auf bestimmte Charakteristika, wie Zellmorphologie, RNA Expression und Protein Expression sowie -lokalisation untersucht, und es konnten keine Unterschiede zwischen den Genotypen festgestellt werden. Demnach haben Varianten im 9p21 Risikolocus keinen Einfluss auf die Zellidentität oder die Differenzierungseffizienz. Wo wir allerdings Unterschiede festgestellt haben ist im Verhalten der VGMZs. So zeigen Zellen mit der Risikovariante eine erhöhte Proliferations- und Migrationsrate. Dies bestätigt Ergebnisse, die bereits publiziert wurden und zeigen, dass das Protokoll auch in unseren Händen gut funktioniert. Für die Verkalkung der entsprechenden Zellen konnten wir zeigen, dass die NR WT Zellen nicht verkalken. Dies zeigten sowohl die spezifischen Färbungen als auch die Expressionsdaten. Zellen, die entweder einen KO der Risikoregion hatten oder die Risikovariante enthielten zeigten positive Verkalkungen in den Färbungen und der

RNA Expression. Somit konnten wir zeigen, dass sowohl das Fehlen als auch das Tragen von Risikovarianten im 9p21 Lokus dazu führt, dass VGMZs verkalken. Abschließend kann also geschlussfolgert werden, dass Patienten, die Risikovarianten im 9p21 Lokus tragen, eher an KAV erkranken können.

1. Introduction

1.1 Coronary artery disease (CAD) and myocardial infarction (MI)

CAD and its main complication MI are the leading causes for deaths worldwide including low- & middle-income countries (Nabel and Braunwald, 2012; The CARDIoGRAMC4D Consortium 2013). In the guidelines of the European Society of Cardiology (ESCa) for CADs (2013), CAD is defined "by episodes of reversible myocardial demand/supply mismatch, related to ischemia or hypoxia, which are usually inducible by exercise, emotion or other stress and reproducible – but, which may also be occurring spontaneously (Montalescot et al., 2013). Such episodes of ischemia/hypoxia are commonly associated with transient chest discomfort (Angina pectoris). Stable CAD (SCAD) also includes the stabilized, often asymptomatic, phases that follow acute coronary syndrome (ACS)." (Montalescot et al., 2013). The epidemiology and severity of CADs increases with age in both sexes. In middle aged men (45 – 65 years) the annual incidence of uncomplicated Angina pectoris strikes about 1%, in women below 65 years of age slightly more are affected (Montalescot et al., 2013). The effect is inverted in men and women aged 75 to 84 years, where almost 4% are affected (Montalescot et al., 2013).

Physical mechanisms leading to MI beneath plaque-related obstruction of epicardial arteries and focal or diffuse spasms of normal or plaque-diseased arteries, are microvascular dysfunctions as well as left-ventricular dysfunctions caused by acute myocardial necrosis and/or hibernation (Montalescot et al., 2013). Hibernation here "implies an adaptive reduction of energy expenditure" where in times of reduced energy availability the cellular activity is reduced (Heusch, 1997).

Atherosclerosis is known to be a major risk factor for the development of CAD/MI. Various factors are known to influence the formation of atherosclerosis including hyperphosphatemia, smoking, obesity, lack of exercise, diabetes, and hypertension (Torpy et al., 2009; Wilson et al., 1998). For a long time it was assumed that atherosclerosis was the product of lipid depositions in the vessels (Libby et al., 2009). Today it is known, that deposition of lipids, especially low-density lipoprotein (LDL)-cholesterol, initiates an inflammatory immune response leading to the activation of

various cells types forming an atherosclerotic plaque (Libby et al., 2009). Partly, those accumulating cells originate from the vessel wall itself.

Anatomically, the vessel wall includes three layers (Fig.1): the inner layer, the tunica intima, consists of a single cell layer of endothelial cells (ECs). The middle layer, tunica media, is made up of various layers of vascular smooth muscle cells (VSMCs). The outer layer, tunica externa, contains fibroblasts, perivascular cells, collagen and nerve endings (Zhao et al., 2015).

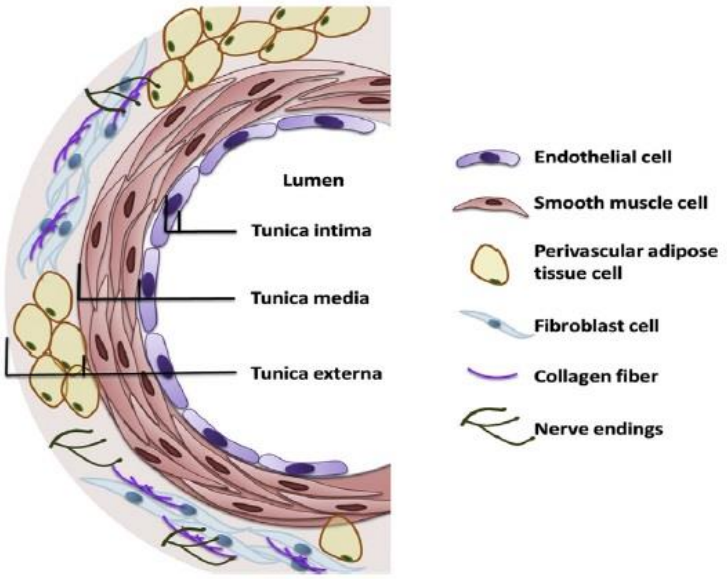

FIGURE 1: Structure of the vessel wall (Zhao et al., 2015)
The vessel wall is composed of three layers. The inner layer, tunica intima, consists of a monolayer of endothelial cells. Tunica media consists of various layers of VSMCs and the outer layer, tunica externa, is composed of various cell types, like fibroblasts, pericytes and nerve cells.

Atherosclerosis initiates as response to inflammation. After macrophages invade the lipid accumulations, other cell types, like dendritic cells, foam cells or platelets are recruited to the sceneries or accumulate at the forming plaque, making it even bigger (Hansson and Libby, 2006). Activated VSMCs from the tunica media then start proliferating and invade the plaque, too (Fig. 2).

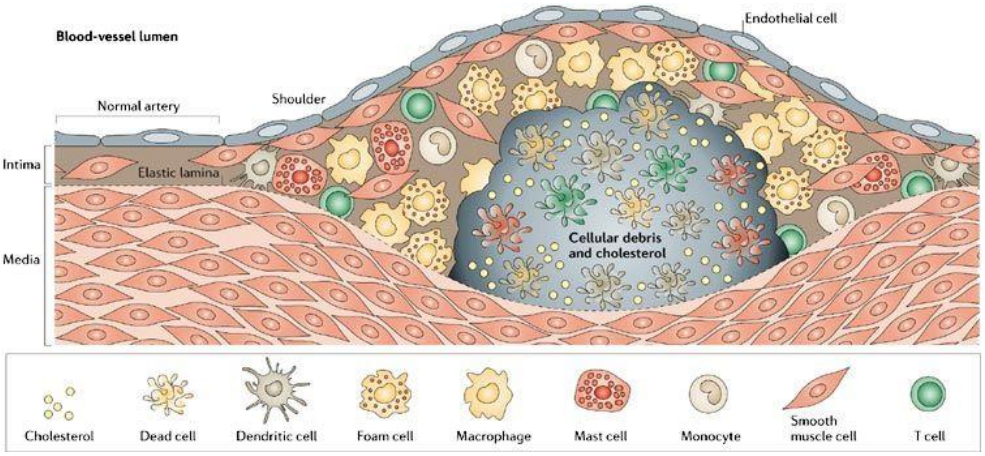

FIGURE 2: Composition of atherosclerotic plaque (Hansson and Libby, 2006)
Atherosclerotic plaques are composed of various cell types, some of them originating from the vascular walls. In atherosclerotic plaque SMCs from the media migrate into the intima. Further, monocytes, macrophages, foam cells and T-cells beneath others are recruited and invade the plaque. In the plaque center dead cells and cholesterol accumulate within the necrotic core.

During the progress of lesion formation, vascular calcification occurs through processes similar to bone formation (Libby and Theroux, 2005) leading to plaque formation in the vessels. Especially, the secreted matrix metalloproteinases (MMPs) modulate various functions of vascular cells and, therefore pave the way to atherosclerosis (Libby and Theroux, 2005). Finally, the plaque is able to rupt, possibly causing thrombosis anywhere in the body, resulting in MI or stroke.

1.2 Genetics of CAD and MI

As mentioned above, conventional risk factors like hypertension, hypercholesterolemia, diabetes, a sedentary lifestyle, obesity, smoking and family history contribute to the risk of developing CAD (Montalescot et al., 2013). In the last years of research it has been described that CAD have a heritability of up to 50% (McPherson and Tybjaerg-Hansen, 2016, The CARDIoGRAMC4D Consortium 2013). Very early hints for the heritability of CAD, and therefore the influence of genetics on the disease, were first reported in family and twin studies. Family based studies can be carried out in three different set-ups: 1) single affected family member, 2) sib-pairs, or 3) extended families (Mayer et al., 2007). The Framingham heart study stated that premature MI in a family increases the risk of CAD depending on CAD in the parents or siblings (Myers et al., 1990). Further the authors stated, that a disease onset in

younger age in affected relatives inevitably leads to an increased familial risk of inheriting the disease (Myers et al., 1990). On the other hand, twin studies were used to examine the risk and heritability of CAD for quite a while. Classical twin studies are based on the analogy in the phenotype between monozygotic or dizygotic twins. Twin studies are consulted to estimate the contribution of the genetic and environmental variation to the phenotypic variation of the disease (Mangino and Spector, 2013). As twins are exposed to consistent pre- as well as postnatal environmental factors they are the ideal model to identify the genetic origins of a disease (Mangino and Spector, 2013). Simultaneously, errors caused by e.g. different fathers is eliminated (Mangino and Spector, 2013). The Swedish twin study identified an increased risk of mortality in monozygotic twins compared to dizygotic twins. In identical twins multiple MI events were reported, leading to the insight that a family history of MI events increased the risk of death due to MI before the age of 55 by 8-fold when the other twin was affected in early age as well (Marenberg et al., 1994).

For almost 20 years candidate gene studies were performed in order to solve the question whether a selected gene is related to a disease. However, this analysis is based on prior knowledge of the function of the gene, as well as the pathophysiology of the disease (Mayer et al., 2007). Since the 1990s over 5000 studies have analyzed candidate genes whereof only 58% are consistent across studies. Problems occurring here could be small study populations, false-positive associations and different ethnicities tested across those studies (Mayer et al., 2007).

In 2007, the concept of genome-wide association studies (GWAS) changed the field of complex genetics dramatically. This era of “gold rush of genomic discovery” (Topol et al., 2007) was preceded by characterisation of the full human DNA sequence, annotation of multiple common single nucleotide polymorphisms (SNPs), and development of arrays that allow simultaneous typing of millions such SNPs at relatively low cost. Based on these assets, GWAS compare the allele frequency of SNPs across the entire genome, with dense coverage of all chromosomes, between cases and controls (Hirschhorn and Daly, 2005). A stringent statistical correction to account for false-positives was proposed by Risch and Merikangas namely the Bonferroni correction derived by dividing 1 million SNPs into 0.05 giving a *P*-value of $5x10^{-8}$. This *P*-value of $5x10^{-8}$ is now referred to as genome-wide significant (Risch and Merikangas, 1996). For high resolution and an unbiased view on the entire

genome hundred thousand of individuals have been studied in this fashion. In order to meet this goal the research community formed international consortia and shared information for subsequent meta-analyses (Schunkert et al., 2019).

Until now, GWASs identified 163 risk loci for MI and CAD (App.C) (Erdmann et al., 2018). One of the first loci to be identified was 9p21 (Helgadottir et al., 2007; McPherson et al., 2007; Samani et al., 2007). Other genes identified recently are e.g. *GUCY1A1*, *ADAMTS7*, *PHACTR1*, and *MRAS* and others. It was shown that most of the disease-associated variants are typically common and located in non-coding regions (Myocardial Infarction Genetics and CARDIoGRAM Exome Consortia Investigators, 2016). These identified risk alleles were thought to explain only 10% of the heritability of CAD (The CARDIoGRAMC4D Consortium, 2013). However, recent studies suggest a heritability of 40 – 60% (Björkegren et al., 2015). Due to high significance levels in GWAS and small effects of single SNPs higher heritability levels might not have been picked up in the data sets (Björkegren et al., 2015).

1.3 Atherosclerosis and Calcification

Calcification deposits may occur as result of progressed atherosclerosis and thus is considered as pathological calcification. Atherosclerotic lesions are usually accompanied by calcium phosphate (CaP) deposits and display the histological appearance of fully formed mineralized bone tissue (Byon et al., 2008; Doherty et al., 2003). Atherosclerotic lesions developing in coronary arteries display an increased total CaP content of 10 to 80-fold, that is also known as hyperphosphatemia (Demer et al., 1994). Pathological hyperphosphatemia is represented by phosphorus concentrations between 1.5 to 2 mM or above (Jono et al., 2000a, 2000b; Lanzer et al., 2014). Cardiovascular calcification is described as the deposition of CaP mineral, usually as hydroxyapatite, in cardiovascular tissues, like arteries, heart valves and the cardiac muscle (Jono et al., 2000a). It is associated with the development of atherosclerotic intimal lesions and a common consequence of aging (Jono et al., 2000b). Vascular calcification is associated with a three to four fold increase in the risk of cardiovascular morbidity and mortality (Alam et al., 2009). Furthermore, calcification is the major cause for failures of native and prosthetic heart valves affecting 1 to 2%

of the aging population (Jono et al., 2000b). For some time, it is known, that calcification of coronary arteries correlates with a high risk to suffer from an MI event through ischemia (Thompson and Towler, 2012). Further, the degree of vascular calcification is nowadays a potent predictor for future cardiovascular events in asymptomatic patients (Proudfoot et al., 2000).

Today, various different terminologies are used to describe vascular calcification. Two major classes of calcification are described. The first class of calcification is dystrophic calcification. Dystrophic calcification describes the pathological deposition of calcium (Ca) salts resembling tooth or bone mineralization in soft tissues, mainly in combination with injury of the respective tissue under normal blood calcium and phosphate homeostasis (Wada et al., 1999). Atherosclerotic plaques and calcific heart valves represent this class of calcification. Metastatic calcification on the other hand, develops in healthy tissues due to hyperphosphatemia and hypercalcemia leading to deposition of insolubilized Ca and phosphate (P), as seen in kidneys, lung or pulmonary veins (Alfrey, 2004; Lanzer et al., 2014).

Another possibility, especially in terms of atherosclerosis, is the classification of calcification according to the anatomical localization. Intimal calcification represents the “classical” form of vascular calcification, displaying calcifying events inside the atherosclerotic plaque. Medial calcification, however can occur in the medial layer of the vessel without existing plaque. In this case, the smooth muscle cells in the tunica media undergo a phenotypic switch towards osteoblastic differentiation, excreting CaP into the extracellular matrix (ECM) (Amann, 2008). Strikingly, patients with pathological end-stage renal disease (ESRD) showed a high degree of intimal calcification but no medial calcification in coronary arteries (Lanzer et al., 2014). Vasuri and colleagues reported in 2014, that the calcification of the tunica intima was associated with atherosclerosis and therefore, is the most common form of calcification, while medial calcifications, that were firstly described by Mönckeberg, showed no associations with atherosclerosis (Vasuri et al., 2014).

Lanzer and colleagues further specify the different types of calcification. First of all, they define vascular calcification as an actively regulated process that is initiated by various signaling pathways and displays similar mineral compositions like bone tissue (Lanzer et al., 2014). Further, they define medial calcifications as deposits of hydroxyapatite with a high degree of crystallization. Medial calcification can be found

in elastic arteries, like the ascending aorta, in medium sized visceral and kidney arteries, as well as in small transitional arteries such as coronary, temporal or uterine arteries (Lanzer et al., 2014).

Already in 1863, Rudolf Ludwig Karl Virchow described the calcification of the arterial wall as “ossification”, giving a first indication on the underlying mechanisms involved in vascular calcification (Demer et al., 1994). Since then, vascular calcification was assumed to be a passive occurrence (Alam et al., 2009; Doherty et al., 2003; Jono et al., 2000b). During this process, apoptotic cell fragments and cholesterol crystals form crystallization locations, where mineralization appears when the local ionic concentration exceeds the salt solubility product (Doherty et al., 2003). Further, Ca depositions occur when the calcification inhibitors are no longer able to prevent Ca precipitation (Doherty et al., 2003). One of these inhibitors are extracellular inorganic pyrophosphates (PPi) as they prevent the formation of CaP coupling and its deposition in the vessels (Villa-Bellosta and Sorribas, 2013)

Ca deposits located in vessels, as mentioned above, are usually calcium apatites, like hydroxyapatite. This mineral is normally present in bones and therefore, points towards an actively regulated process (Proudfoot et al., 2000). As it is known today, vascular calcification is an active, cell-regulated process similar to bone or teeth formation (Alam et al., 2009; Balderman et al., 2012; Doherty et al., 2003; Jono et al., 2000b; Reynolds et al., 2004). Nevertheless, it is not known for sure whether VSMCs or ECs are the procuring cells in arterial calcification (Doherty et al., 2003).

Generally, the differentiation process of VSMCs is mediated by microenvironmental and mechanical stimuli. Cells growing on stiff substrates, like fibronectin, are mediated towards an osteochondrogenic development. On the other hand, flexible substrates, like laminin promote the VSMC and adipogenic development (Vasuri et al., 2014). Another component strongly contributing to calcification is the VSMC phenotype. During calcification processes VSMCs lose their expression of smooth muscle cell (SMC)-typical genes like smooth muscle alpha actin (*SmαA),* Calponin (*CNN1*) or transgelin (*TAGLN)*, and start expressing osteogenic markers, such as osteocalcin (*OCL*), and deposit bone-like minerals in the ECM (Alam et al., 2009; Balderman et al., 2012; Byon et al., 2008; Tintut et al., 2003). The reasons, how and why this phenotypic transdifferentiation of VSMCs to osteoblastic cells occurs are not yet fully understood (Alam et al., 2009). The phenotypic switch and their calcification *in vitro* might be

induced by hyperphosphatemia, probably via upregulation of POU class 1 homeobox 1 (*PIT-1*) and SP7 transcription factor, also known as osterix (*SP7*), as suggested by Alam and colleagues (Alam et al., 2009). *SP7* is the master gene for mesenchymal differentiation whereof later osteoblasts originate (Vasuri et al., 2014). On the other hand, different experiments indicated calcification might occur independently from P, making other factors responsible for the induction for calcification of the vasculature in addition to hyperphosphatemia (Alam et al., 2009).

Osteoblast-like, multinucleated osteoclast-like or chondrocyte-like cells have been detected in diseased arteries but not in healthy vessels, confirming the assumption that vascular calcification occurs similar to bone formation (Vasuri et al., 2014). In healthy human vessels, the expression of various proteins associated with bone formation can be detected at a relatively low level. In plaques however, extremely high levels of these proteins are expressed, especially in regions were calcification processes are taking place (Doherty et al., 2003). Similar to these processes, it has been observed that circulating bone marrow-derived or resident stem cells or progenitors might have an influence on vascular calcification (Vasuri et al., 2014).

SMCs of the vascular system possess a sodium-dependent P uptake system that regulates the mineralization of secreted matrix due to elevated P levels, leading to increased inorganic phosphate (Pi). This mineralization process is dependent on the function of a type III sodium-dependent phosphate Co-transporter (NPC) (Jono et al., 2000a). The phosphate uptake by the NPC, encoded by *PIT-1*, leads to increased expression of runt related transcription factor 2 (*RUNX2*) and distal-less homeobox 5 (*DLX5*). The increased level of *RUNX2* and *DLX5* then result in evolvement of promineralizing matrix expressing osteopontin (*OPN*), *OCL,* and cathepsin K (*CTSK*) (Fig. 3) (Giachelli, 2009).

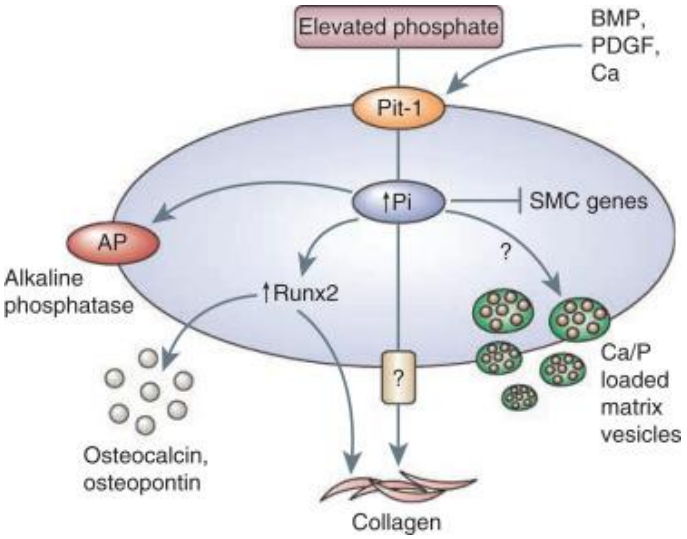

FIGURE 3: Key mechanisms leading to VSMC-calcification (Giachelli, 2009)
Elevated phosphate leads to increased inorganic phosphate (Pi) that then increases alkaline phosphatase (*AP)* and *RUNX2* expression. Increased *RUNX2* expression induces the expression of *OCL* and *OPN*, and increases the excretion of ECM.

OCL is exclusively synthesized by osteoblasts that make up around 2% of the bone matrix (Vasuri et al., 2014). The protein is capable of binding hydroxyapatite that then influences cell signaling leading to the recruitment of additional osteoblasts and osteoclasts (Vasuri et al., 2014). Vitamin D3 tightly regulates the transcription of *OCL* (Vasuri et al., 2014).

Today, *RUNX2* is thought to be the master transcription factor of calcification also inducing osteoblastic and chondrocytic differentiation (Balderman et al., 2012). In healthy VSMCs cultured under standard conditions *RUNX2* is not expressed, which can also be seen in mouse and human tissues (Balderman et al., 2012; Byon et al., 2008). Nevertheless, under procalcifying conditions, like inflammation, oxidative stress or bone morphogenic protein 2 (BMP2) exposure, *RUNX2* expression is upregulated (Balderman et al., 2012; Lin et al., 2015; Sun et al., 2012). *RUNX2* also induces alkaline phosphatase (*ALPL*) activity and upregulates the expression of other bone matrix protein-coding genes such as *OCL*, Collagen I (*COL1*), *OPN* and others. Further, *RUNX2* mediates the mineralization of immature mesenchymal and osteoblastic cells *in vitro* (Byon et al., 2008; Vasuri et al., 2014). On the other hand, in osteoblast-like SMCs *RUNX2* is expressed, indicating that a *RUNX2* upregulation results in VSMC-to-osteoblastic transition (Balderman et al., 2012).

Additionally, hydrogen peroxide (H_2O_2) treatment of cells *in vitro* leads to an increase of osteogenic markers like *ALPL*, collagen 1 (*COL1),* colony stimulating factor 1

(CSF1), TNF superfamily member 11 *(TNFSF11/RANKL)* and *OCL* in a concentration-dependent manner, while expression of SMC-specific genes such as *SMαA* or *TAGLN* are decreasing (Byon et al., 2008). H_2O_2 treated cells furthermore, show elevated levels of *RUNX2* transcripts suggesting a correlation between both factors. H_2O_2 was reported to stimulate the activation of extracellular signal-regulated kinase (ERK), AKT serine/threonine kinase 1 (AKT) and phospholipase C gamma (PLCγ) pathways which are all important mediators of intracellular calcium signaling (Byon et al., 2008). Byon et al. also described that *RUNX2* is required for oxidative-stress induced calcification of VSMCs *in vitro* (Byon et al., 2008). Reactive oxygen species (ROS), like H_2O_2, and nitrogen species are produced by vascular cells via oxidases in the endothelium, the tunica media and the adventitia when stimulated. Especially, H_2O_2 is produced by those oxidases which leads to increased exposure of VSMCs to the ROSs that finally influences the intracellular signaling and results in calcification processes in vessels (Byon et al., 2008).

As mentioned before, *OPN* is one of the markers for calcification. This bone matrix protein is expressed in atherosclerosis (Doherty et al., 2003). *OPN* is also found in mineralized tissues such as teeth and bones as well as kidney, urine and epithelial linings of numerous organs (Jono et al., 2000b). Various diseases, like Mönckbergs sclerosis, aortic stenosis, prosthetic valves calcification, renal stones and tumor-associated calcifications showed high expression of *OPN*. However, calcification sites of atherosclerotic plaques and calcified aortic valves lack *OPN* expression (Jono et al., 2000b). Cell adhesion and migration as well as hydroxyapatite formation are influenced by *OPN*. The synthesized protein is able to exist in various forms depending on the extent of post-translational modification such as sulfation, glycosylation, transglutamination and phosphorylation. Highly phosphorylated *OPN* was isolated from mineralized ECM of bone tissue where it has been synthesized by osteoblasts and had bound Ca (Jono et al., 2000b). Also, ECs and macrophages are capable of expressing *OPN* (Vasuri et al., 2014). When phosphorylation of *OPN* is inhibited *in vitro* calcification of human VSMCs was prevented (Jono et al., 2000b).

Besides the genes described above, tumor necrosis factor α (TNFα) needs to be mentioned as it is known to be involved in vascular and bone pathophysiology. TNFα is secreted from macrophages in response to oxidative low-density lipoprotein (oxLDL), acetylated LDL (acLDL), physically damaged ECM and bacteria (Tintut et al.,

2000). *In vivo*, TNFα was shown to increase the permeability of ECs, monocyte adhesion, macrophage differentiation and foam cell formation. Atherosclerotic lesions in coronary arteries are induced by TNFα, and bone turnover is regulated by this factor as well. Finally, osteoblastic function is inhibited by TNFα and it stimulates bone resorption (Tintut et al., 2000). In calcification, TNFα promotes the mineralization by modulation of the ECM formation and mineralization-associated genes like the 3',5'-cyclic adenosine monophosphate (cAMP) pathway and overall induction of transcription of genes involved in osteogenic differentiation (Tintut et al., 2000).

Beneath the ability of VSMCs to transdifferentiate into osteo-chondrogenic-like cells, VSMCs are able to generate nucleation sites for deposition of CaP. The activation of osteogenic gene expression leads to endocytosis of nanoparticles, around 30 to 500 nanometers (nm) in size that are subsequently accumulated in the lysosomes where the crystals then get dissolved. Therefore, the CaP concentration in the cells rises and leads to apoptotic and necrotic processes (Lanzer et al., 2014). The latest hypothesis thereafter implements, that apoptotic bodies (50 to 5000 nm) get released from the VSMCs and then act as nucleation scene for crystallizations within the aortic wall (Lanzer et al., 2014; Reynolds et al., 2004). Already in 2000, Proudfoot and his team suggested that dying cells produced apoptotic matrix vesicles that might contribute to calcification. They reported, that inhibition of apoptosis in cells also inhibited calcification (Proudfoot et al., 2000). As apoptotic bodies are capable of accumulating and crystallizing Ca, it can be said that apoptosis induces vascular calcification (Proudfoot et al., 2000). Only recently, matrix vesicles have been identified to induce calcification of the tunica intima and media (Vasuri et al., 2014).

Further, the combination of various calcifying reagents have been published to induce calcification in SMCs of different species, such as β-GP, L-AP, insulin, and dexamethasone *in vitro* (Alves et al., 2014; Tziakas et al., 2019). However, the precise mechanism is not yet fully understood.

1.4 CAD risk locus Chr9p21

In 2007 the chromosomal region 9p21 was first reported as a CAD risk locus (Burton et al., 2007; Helgadottir et al., 2007; McPherson et al., 2007; Samani et al., 2007) (Fig.

4). The calcification of coronary arteries and the aorta is one major risk factor for CAD and MI independent of “classical” risk factors like cholesterol levels, body mass index (BMI), smoking, hypertension, age, gender and family history (van Setten et al., 2013). With around 50% allele frequency the 9p21 locus is a fairly common and highly heritable risk locus (van Setten et al., 2013). Holdt and Teupser reported that there is a conferred increase of CAD risk of around 30% for carriers of one allele and more than 60% for carriers of two alleles (Holdt and Teupser, 2012). In various GWA studies CAD risk genes were tested for their association to aortic and coronary artery calcification (Helgadottir et al., 2007; McPherson and Tybjaerg-Hansen, 2016; Samani et al., 2007). The 9p21 locus was replicated in individuals with European, Korean, Japanese, Chinese and Pakistani origin, as well as in US-Hispanics, where its association with CAD was consistent (Holdt and Teupser, 2013). Only in African blacks, differing haplotype structure and divergent relationships to CAD were observed (Holdt and Teupser, 2012).

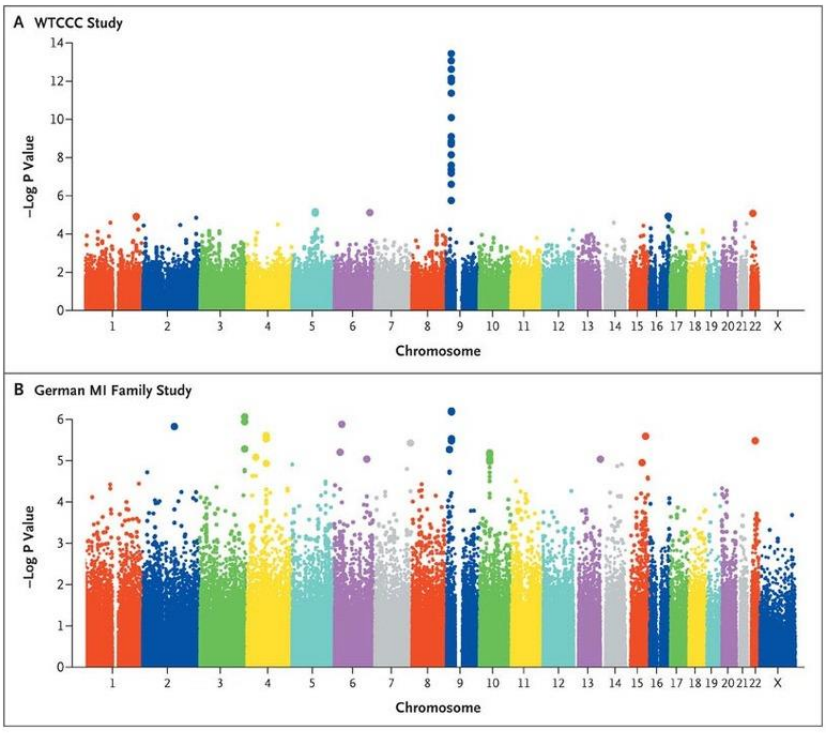

FIGURE 4: Manhattan Plot of GWASs identifying 9p21 as risk locus for CAD (Samani et al., 2007) GWASs show CAD associated risk loci. 9p21 shows the strongest association in the WTCCC (A) and the German MI Family study (B).

In addition, the 9p21 locus has been associated with various heart related traits like carotid artery plaque, stroke, aneurysms, peripheral artery disease, heart failure and

cardiovascular mortality, which pointed towards a role of 9p21 in vascular pathology (Holdt and Teupser, 2012). As no associations of 9p21 with common risk factors, such as lipid levels or hypertension were identified, it was proposed that the 9p21 locus might play a role in a completely different mechanism than lipid metabolism as a cause for CAD (van Setten et al., 2013). The 9p21 locus is one of the most replicated markers for CAD and MI. Recently, it has been discovered that the haplotype block with multiple single nucleotide polymorphisms (SNPs) is spanning a region of approximately 50 kb in the deoxyribonucleic acid (DNA) sequence (Holdt and Teupser, 2012). The center of the haplotype block is located within a region free of protein-coding genes. Therefore, the focus for research was placed on the closest protein-coding regions Antisense non-coding RNA in the INK4-locus (*ANRIL,* also known as CDKN2BAS) and the INK4/Arf locus. *ANRIL* is thought to regulate the epigenetic modification that modulates the risk of cardiovascular diseases (Holdt and Teupser, 2012).

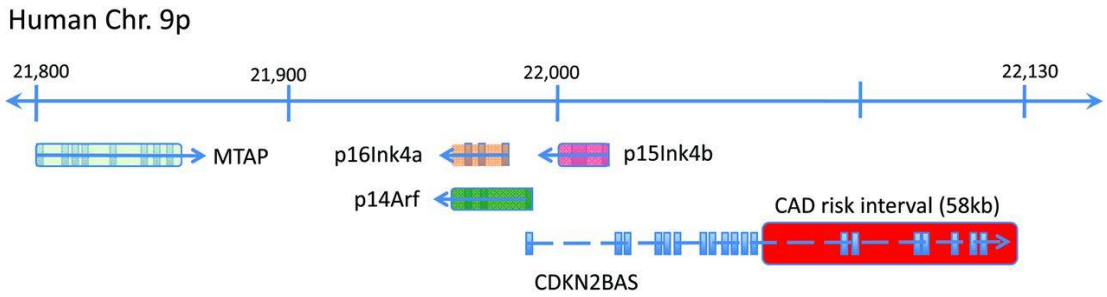

FIGURE 5: Location of CAD risk interval on human Chromosome 9 (Kim et al., 2012)
The CAD risk interval on 9p21 is located just downstream of various genes, like MTAP and CDKNs, and is located within the *ANRIL (CDKN2BAS)* region.

The core CAD risk region was identified to be located slightly distal to the INK4/Arf locus (Fig.5). This region encodes two cyclin-dependent kinase inhibitors (CDKNs): *CDKN2B* and *CDKN2A*. Both genes are cell cycle regulating proteins and are known to act as tumor suppressors (Holdt and Teupser, 2012). *CDKN2B* codes for $p15^{INK4B}$, whereas $p14^{Arf}$ and $p16^{INK4A}$ are partly encoded by *CDKN2A* and share the exons 2 and 3 (Holdt and Teupser, 2012). $P14^{Arf}$ activates p53 inducing cell cycle arrest and apoptosis. $P15^{INK4B}$ and $p16^{INK4A}$ have similar functions, as they bind to the catalytic subunit of cyclin-dependent kinases (CDK) 4 and 6. They form a stable complex with the CDKs, which hinders the binding of cyclins for catalytic activity (Handschick, 2014). This prevents the phosphorylation of retinoblastoma-family proteins, which leads to G1-Phase arrest and therefore, blocks cell proliferation (Holdt and Teupser, 2012).

Another gene located on 9p21 is methylthioadenosine phosphorylase (*MTAP*), which is located proximal, and also shares some exons with the INK4/Arf locus (Holdt and Teupser, 2012). *MTAP* catalyzes the phosphorylation of 5'-methyladenosine, which is associated with cell growth. As proliferation and apoptosis play a role in atherogenesis, the genes at the INK4/Arf locus might be suitable candidate gene as risk loci for atherosclerosis. Unfortunately, studies did not reflect the assumed association to atherosclerosis so far (Holdt and Teupser, 2012). On the other hand, *ANRIL* has shown strong associations to atherosclerosis. It is presumed that *ANRIL* might modulate the neighbouring genes in *cis*. In *ANRIL* knock-out (KO) mice cellular proliferation was described to be significantly reduced, which might contribute to atherosclerotic events (Holdt and Teupser, 2012). The expression of *ANRIL* and *CDKN2A/CDKN2B* has been associated with various atherosclerosis-related phenotypes. The deletion of this region in aortic SMCs *in vitro* led to the loss of their proliferative capacity, which is known to be important for the manifestation of atherosclerosis (Visel et al., 2010).
In terms of calcification, the 9p21 locus did not show a genome-wide association for aortic calcification, but for coronary artery calcification. Near *CDKN2A* and *CDKN2B*, 37 SNPs overall exceeded the genome-wide significance with a P-value of $P<5*10^{-8}$ (van Setten et al., 2013).

1.5 Vascular smooth muscle cells – *in vitro* models

Overall, VSMCs give structural support to vascular blood vessels and provide the contractile properties (Dash et al., 2015; M Drab, 1997; Sinha et al., 2014). VSMCs are necessary for various physiological functions such as contraction, regulation of blood pressure, regulation of blood vessel diameter and blood flow dispersion (Alexander and Owens, 2012; Beamish et al., 2010). Together with pericytes (PCs), VSMCs excrete ECM and its components, like collagen and elastin, that determine the mechanical properties of mature vessels (Alexander and Owens, 2012). Primary VSMCs do not differentiate conclusively. They display various phenotypes, and in addition the ability to switch between phenotypes. Various studies have raised the question whether this phenotypic plasticity might give a hint to the development of vascular disorders (Adam et al., 2000; Alexander and Owens, 2012; Sinha et al., 2014).

The majority of VSMCs in the tunica media contains a contractile phenotype required for regulation of vascular tone (Adam et al., 2000). Contractile VSMCs contain a fully functional contractile apparatus and they respond to small molecules, like acetylcholine and norepinephrine (Beamish et al., 2010). Cell compartments, like tightly bundled myofilaments, minimal rough endoplasmatic reticulum (ER), reduced golgi apparatus and few free ribosomes, as well as little connective tissues are specific for the contractile VSMC phenotype, as well as low proliferation rate (Beamish et al., 2010; Sinha et al., 2014). These cells express specific contractile proteins, ion channels and signaling molecules that are necessary for contractile functions (Alexander and Owens, 2012). Contractile VSMCs have a spindle shaped morphology and express typical contractile marker proteins like *SMαA*, smooth muscle myosin heavy chains SM-1 and SM-2, *TAGLN*, and smoothelin (*SMTN*) (Beamish et al., 2010; Rensen et al., 2007; Sinha et al., 2014). The synthetic VSMCs on the other hand, show a fibroblast-like morphology, express fewer contractile proteins and secrete a high amount of ECM. On cellular level, there are little to no contractile bundles in synthetic VSMCs, but extensive rough ER, a well-defined golgi apparatus and many free ribosomes. Due to their broad, spread morphology, cells even grow over one another creating a “hill and valley” morphology that is due to a high proliferation rate in synthetic VSMCs (Beamish et al., 2010; Rensen et al., 2007; Sinha et al., 2014). Proteins specifically expressed by VSMCs of the synthetic phenotype are caldesmon1 (*CALD1*), vimentin (*VIM*), myosin heavy chain 10 (*MYH10*), tropomyosin 4 (*TPM4*) and retinol binding protein 1 (*RBP1*) (Beamish et al., 2010). Unfortunately, various SMC marker genes are also transiently expressed in other cell types during embryonic development, tissue repair and disease states, making it necessary to include various genes and proteins in the analysis of VSMCs (Gomez and Owens, 2012).

The vascular development in early embryogenesis is regulated by only three cell types, namely ECs, SMCs and PCs. ECs make up the first vessel structures, which are then remodeled by the recruitment of SMCs and PCs (Sinha et al., 2014). In embryogenesis of vertebrates, VSMCs arise from various mesodermal lineages, like neural crest (or lateral mesoderm [LM] and paraxial mesoderm [PM]), secondary heart field (SHF) and the pro-epicardial organ (PEO) (Dash et al., 2015; Marchand et al., 2014; Sinha et al., 2014). Cells derived from the mesoderm give rise to VSMCs of e.g. the aortic root, ascending and descending aorta and coronary arteries (Ayoubi et al., 2017). As

VSMCs of the coronary arteries are of special interest for the analysis of CAC, generated VSMCs need to be of lateral mesoderm origin as they mainly build up the respective coronary arteries in the embryonic development (Ayoubi et al., 2017). The patterning of the mesoderm is influenced by multiple signaling gradients, growth factors and transcriptional factors, which are generally conserved across species (Sinha et al., 2014). Especially, basic fibroblast growth factors (bFGFs), Wingless-type MMTV integration site family member (Wnts), and the TGFβ-family members bone-morphogenic protein-4 (BMP4), activin and nodal regulate the mesoderm patterning during embryogenesis. BMP4-gradients lead to mesodermal subtypes, namely LM, defined by a high BMP4 concentration, and PM, defined by a lower BMP4 concentration (Sinha et al., 2014) (Fig. 6).

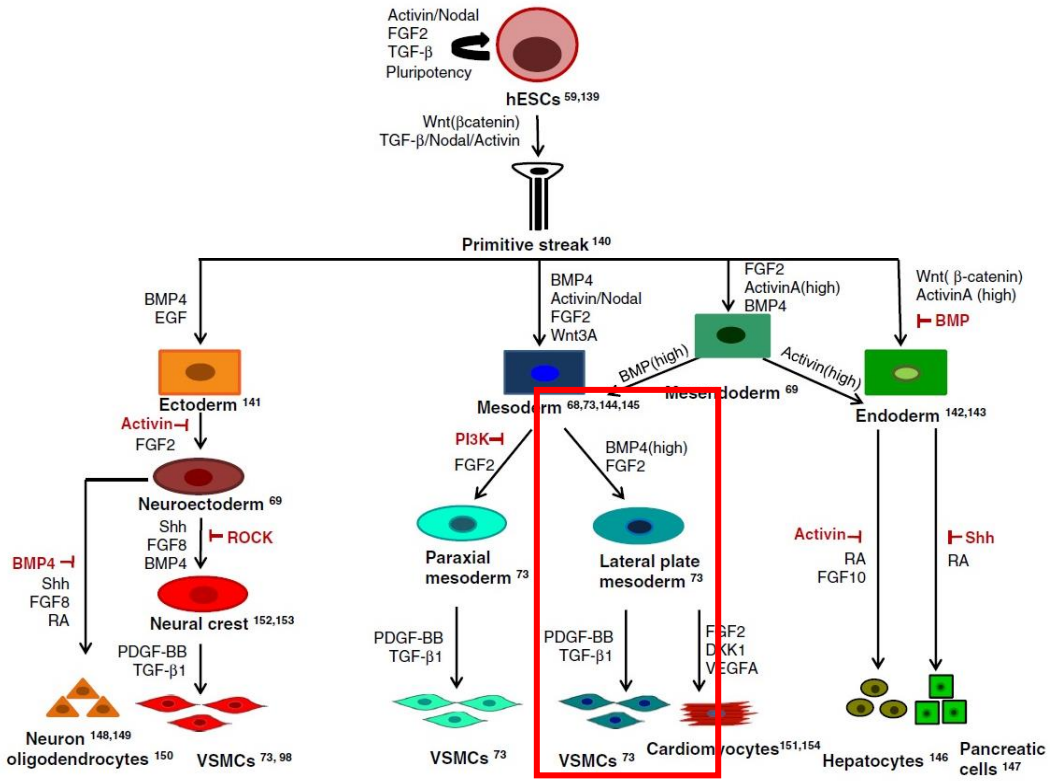

FIGURE 6: Differentiation pathways (Sinha et al., 2014)
ESCs are driven towards differentiation by induction of Wnt and TGFβ1 signaling pathways. Mesoderm is induced via BMP4, Activin/Nodal, FGF2 and WNT3A signaling. Lateral mesoderm is defined by high concentrations of BMP4, and FGF2, and emerging VSMCs are defined by PDGF-BB and TGFβ1 signaling (red box).

It is well known, that primary VSMCs quickly lose their phenotypic properties *in vitro* that rises various complications for their use in long term experiments *in vitro,* and requires verification of the results *in vivo* (Alexander and Owens, 2012). Further,

primary VSMCs lose their proliferative activity with increasing donor age, and puts donors at high risks for the isolation of cells, as a surgical intervention is necessary to access primary VSMCs (Dash et al., 2015).

Transforming growth factor beta 1 (TGFβ1) regulates the differentiation of VSMCs during embryogenesis. The loss of TGFβ1 in mice leads to prenatal death initiated by the incomplete differentiation of mesenchymal progenitors into VSMCs. Further, elevated TGFβ1 expression on RNA and protein level were detected in injured rat carotid arteries and human re-stenotic tissues indicating its role in VSMC distinction (Adam et al., 2000). The neural crest develops within the 4th week of embryogenesis in humans and around embryonic day E8.5 in mice. The progenitors are induced at the edge of the neural plate via high concentrations of BMP4, WNT, bFGF and Notch (Sinha et al., 2014) (Fig. 6). A diminished BMP4 signaling promotes neural development in embryogenesis of vertebrates (Sinha et al., 2014). The resulting cells in the neural crest give rise to VSMCs of the ascending aorta, the aortic arch and the pulmonary trunk (Dash et al., 2015). SMCs of the descending aorta originate from the PM (Sinha et al., 2014). Cells originating from the SHF are a progenitor cell population along the anterior-posterior axis of the pharyngeal mesoderm behind the cardiac crescent that build up the myocardium. Such cells give rise to VSMCs at the base of the aorta and the pulmonary trunk (Dash et al., 2015). The pro-epicardium is a transient structure in the looped heart stage of embryogenesis located at the venous pole and originates from the LM (Sinha et al., 2014). Finally, cells arising from the PEO undergo epithelial to mesenchymal transitions of immigrated pre-epicardial cells, that develop into progenitors of coronary SMCs, as illustrated in fate-map studies (Dash et al., 2015; Sinha et al., 2014). VSMC origin and local factors, like blood flow and shear stress, as well as vessel wall composition, are thought to influence the location and progression of vascular diseases (Sinha et al., 2014).

As mentioned above, VSMCs are able to undergo a phenotypic switch from a contractile to a synthetic phenotype. The synthetic phenotype is mediated by platelet derived growth factor (PDGF), bFGF, insulin-like growth factors (IGFs), epidermal growth factor (EGF), α-thrombin, factor Xa, angiotensin-II (ANG-II), endothelin-1, and unsaturated lypophosphatidic acid (Beamish et al., 2010). The contractile phenotype on the other hand, is promoted by the expression of heparin, TGFβ, and ANG-II and IGF1 as well (Beamish et al., 2010; Hayashi et al., 2004). Generally, the SMC

phenotypic switch is characterized by reduced expression of VSMC-selective differentiation markers, increased proliferation rate, as well as increased migration and the synthesis of ECM-components required for vascular repair (Alexander and Owens, 2012) (Fig. 7).

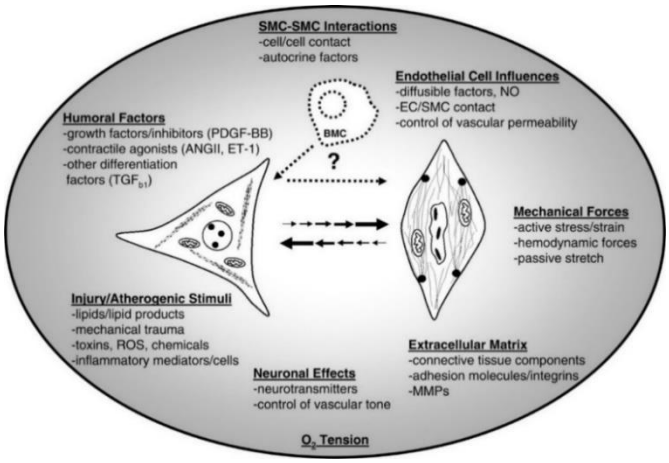

FIGURE 7: Characteristics of VSMC phenotype switch (Owens et al., 2004)
Various factors contribute to VSMC phenotypic switch, like cell interactions with ECs and SMCs, mechanical forces, ECM composition, oxygen (O_2), neuronal effects, injury and inflammation, as well as humoral factors, like growth factors, stimulators and differentiation factors.

Primary VSMCs usually contain a phenotype that is located in between both extreme ends and therefore, display both functions to a certain extend. The bigger problem however, is that primary VSMCs undergo a phenotypic switch *in vitro* (often referred to as “de-differentiation”), that leads to a loss of contractile characteristics and functions. This, in the end, makes it necessary to verify *in vitro* findings *in vivo* (Alexander and Owens, 2012). As mentioned before, primary VSMCs lose their proliferative potential with increasing donor age, leading to the problem of a reliable source of cells (Dash et al., 2015). Senescent cells release high amounts of MMP9, secrete less collagen, promote mononuclear cell chemotaxis and stimulate adjacent ECs to express pro-adhesive and pro-inflammatory phenotypes (Majesky, 2016). Due to a variety of problems with primary VSMC culture, it seems an alternative to use induced-pluripotent stem cell (iPSC)-derived VSMCs. Up to now, there are some differentiation protocols known that enable the generation of VSMCs out of pluripotent stem cells (PSCs) *in vitro*. It is known, that embryonic stem cells (ESCs) can be differentiated into VSMCs with the use of all-trans retinoic acid (RA) (Beamish et al., 2010).

1.6 Induced-pluripotent stem cells in disease research

Human ESCs were first isolated in 1998 by Thomson and co-workers at the University of Wisconsin-Madison, USA from pre-implantation embryos (Thomson et al., 1998). PSCs have a virtually unlimited replicative capacity and are capable to differentiate into 200 cell types of the body (Boyer et al., 2005). PSCs naturally occur in the inner cell mass (ICM) of the blastocyst (Wobus and Boheler, 2005). The differentiation potential decreases during differentiation with the increasing specificity of the cells. Accordingly, multipotent stem cells within the different germ layers are restricted to differentiate into germ layer derivatives. The differentiation potential of pluripotent cells is not restricted (Wobus and Boheler, 2005) (Fig. 8).

Only a small number of PSCs are determined to become progenitors of gametes. During embryogenesis, PSCs differentiate into multipotent cells, which subsequently become progenitors of certain tissues and finally develop into specialized cells of the respective tissues (Jung, 2014).

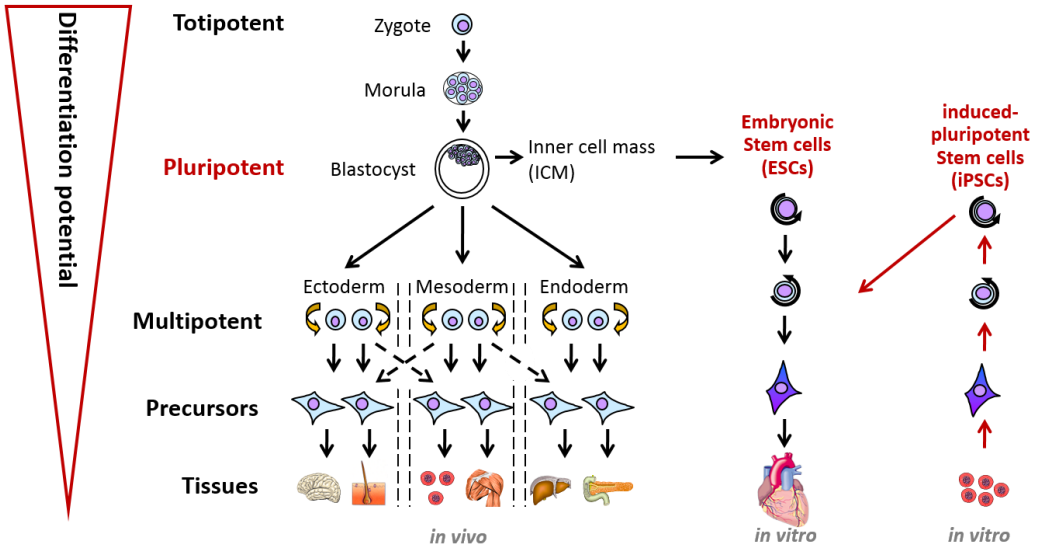

FIGURE 8: Differentiation potential and potencies of stem cells in embryonic development and reprogramming (modified from Wobus and Boheler, 2005)
ESCs are harvested from the ICM and can be differentiated *in vitro* following the embryological development via multipotent germ layer cells and precursors into specified cells of the tissues. Human iPSCs resemble ESC characteristics and can be differentiated into specific cells *in vitro* as well.

Still, ethical concerns arise about the isolation and cultivation, as well as the utilization of ESCs in research in Germany (Strong et al., 2009). Importantly iPSCs provide an alternative to ESCs, as the ethical concerns mentioned above are not valid for adult cells.

In order to generate iPSCs, differentiated cells are reprogrammed by the forced expression of pluripotency factors. Four of these factors were discovered by Yamanaka and Takahashi in 2006, and honored with a Nobel Prize in 2012. They were able to reprogram mouse fibroblasts with the overexpression of octamer-binding transcription factor 4 *(OCT4)*, sex-determining region Y-box 2 *(SOX2)*, kruppel-like factor 4 *(KLF4)* and v-Myc avian myelocytomatosis viral oncogene homolog (*MYC*, alias *c-MYC*) with the help of a retrovirus (Takahashi et al., 2007). The group of James Thomson replaced Klf4 and c-Myc by lin-28 homolog A (*C. elegans*) (*LIN28A*, alias *LIN28*) and Nanog homeobox (*NANOG*) (Yu et al., 2007). *OCT4* is expressed in the very early stages in mammalian development. It is essential for the pluripotency of cells from the ICM *in vivo* and their maintenance *in vitro* (Hanna et al., 2010). *NANOG* is activated in the 8-cell stage and is also expressed in the ICM (Hanna et al., 2010). *SOX2* regulates the levels of *OCT4* expression (Patel and Yang, 2010). *SOX2* in combination with *OCT4* target the micro RNA (miRNA) miR-302/367 cluster that inhibits the cell cycle regulator cyclin D1 (Rao and Malik, 2012). *KLF4* is involved in self renewal of ESCs, probably by the regulation of ESC-specific genes (Jaenisch and Young, 2008). *LIN28* represses the processing of the lethal-7 (*LET-7*) precursor into a mature miRNA. *C-MYC* seems to be involved in chromatin modelling (Patel and Yang, 2010), and it transactivates various genes required for reprogramming (Singhal et al., 2010). Especially, *OCT4*, *SOX2*, and *NANOG* regulate each other. Further, epigenetic modifications decide between pluripotency and differentiation and, are therefore important for the maintenance of a pluripotent state.

Patient- and disease-specific iPSCs are of great value for drug tests on a realistic population with varying genetic background, studying disease progression on a cellular level, and developing cell therapies (Chen et al., 2016; MacArthur et al., 2012) (Fig. 9).

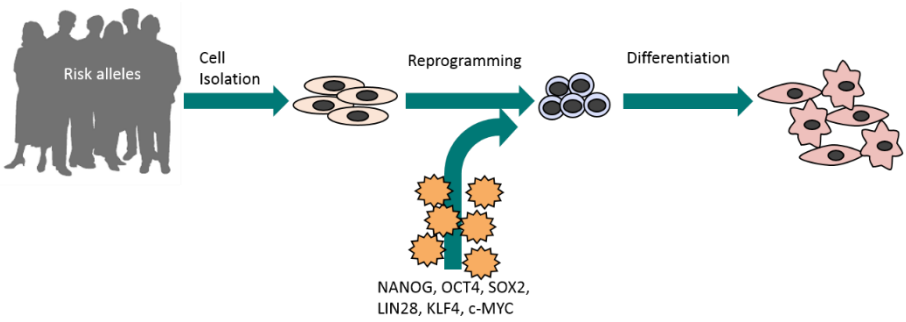

FIGURE 9: Generation of patient-derived iPSCs
Patients containing disease risk alleles provide somatic cells that are isolated and reprogrammed to iPSCs and can then be differentiated to disease-specific cell types for analysis of disease progression or drug screening.

Compared to primary cells, iPSCs are an almost unlimited source of target cells without putting patients at risk in surgical treatments for the isolation of cells (Chen et al., 2016). Further, primary cells are not sustainable *in vitro* for a long time and they often lose their phenotype during long-term culture *in vitro* (Chen et al., 2016). Furthermore, iPSCs are the only tool to verify the genetic findings of GWAS on a cellular level with the specific genetic background in order to describe a disease-related mechanism caused by SNPs or copy number variations (CNVs). The iPSC technology enables the observation of the genetic causes of CAD during the development of cardio-vascular cell types. Human iPSC models for vascular ECs- and VSMCs-affecting diseases are essential as there are species-dependent differences in structure and function between mice and humans for instance (Chen et al., 2016). Hence, an animal model alone is insufficient for studying these diseases (Chen et al., 2016). Lately, various models have been published in order to acquire VSMCs out of iPSCs. One possibility for the differentiation of iPSCs into VSMCs is to use the aggregation of embryoid bodies (EBs) ahead of differentiation. This method however, brings the issue of limited accessibility for growth factors to the EBs center and the cells' heterogeneity within one EB (Dash et al., 2015) (Fig. 8). Another method is the differentiation in a monolayer on ECM-coatings, which seems much more convenient in regard to nutrient and growth factor availability for the cells (Fig. 10).

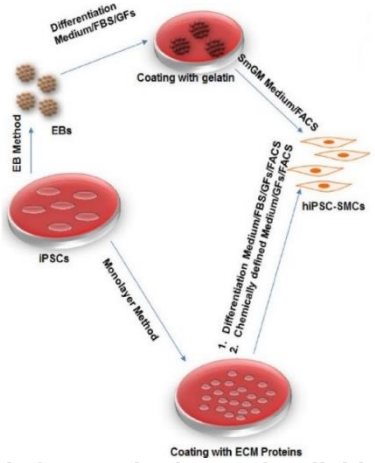

FIGURE 10: VSMC differentiation methods can be divided into 2D and 3D methods (Dash et al., 2015)
Either 2D differentiation using gelatin-coated plates or 3D methods via embryoid bodies can be used for VSMC differentiation from iPSCs.

The resulting cells display expression profiles similar to native SMCs. Nevertheless, significant variability in the expression patterns have been observed (Beamish et al., 2010). However, resulting VSMCs showed high proliferation potential, a morphology similar to primary SMCs and stable expression of SMC marker genes. Furthermore, iPSC-derived VSMCs showed contractile response to vasoactive agonists and organized themselves in fibrillar networks similar to networks in native vessels, confirming their structural and functional properties (Beamish et al., 2010).

1.7 Gene editing technologies

Gene or genome-editing is defined as the process of inducing targeted and specific modifications to the genome, its context (e.g. epigenetic marks) or its outputs (transcripts) (Hsu et al., 2014). The desire to study the effects of genetic mutations on the development of various diseases in a controlled *in vitro* environment or in *in vivo* systems has been great ever since. In the 1970s the recombinant DNA-technology developed, holding the opportunity to exchange exogenous repair DNA-templates against genomic DNA in an organism or in cells that contain sequence homology to the donor site (Hsu et al., 2014). This technology enabled the generation of knock-out (KO) and knock-in (KI) animal models via manipulation of germline cells (Hsu et al., 2014).

Recently established gene editing tools are zinc-finger nucleases (ZFNs) and transcription activator-like effector nucleases (TALENs), which use engineered endonucleases (Horii and Hatada, 2016). In both systems, a sequence-specific DNA-binding domain is merged with a non-specific DNA cleavage module (Gaj et al., 2013). TALENs' DNA-binding domains are composed of various 33 – 35 amino acid repeats that each recognizes a single base (Gaj et al., 2013; Wei et al., 2013). The specificity of TALENs is defined by two variable amino acids, so-called repeat-variable di-residues (RVDs) (Gaj et al., 2013; Wei et al., 2013). Nowadays, it is possible to design the DNA-binding domain according to the customers' desire in order to target virtually any sequence in the genome for both, ZFNs and TALENs (Gaj et al., 2013). TALEN binding sites require a single thymidine (T) most of the times whilst ZFNs need a three-base recognition site every 20 to 500 bp (Gaj et al., 2013; Strong and Musunuru, 2017; Wei et al., 2013). For both systems, custom-designed proteins are commercially available (Gaj et al., 2013; Wei et al., 2013). A disadvantage of ZFNs an TALENs is that both systems are rather complicated to design, time-consuming and expensive in the construction processes of DNA-binding proteins (Hsu et al., 2014; Wei et al., 2013). Further, ZFNs show a considerably low specificity due to crosstalk events that make extensive screening processes necessary (Hsu et al., 2014; Sander and Joung, 2014). The efficiency of TALEN-based genome editing shows immense variations between 0% - 50% in zebrafish or even 65% in flies (Wei et al., 2013).

Recently, the genome editing technology CRISPR (Clustered regularly interspaced short palindromic repeats) /Cas (CRISPR-associated) system was established. It was firstly discovered in 1987 by Nakata and colleagues in *E. coli* (Richter et al., 2012), as an intracellular "anti-virus" system (Rath et al., 2015; Sander and Joung, 2014).

TALENs and CRISPR/Cas, both are able to induce genomic modifications that can generate indels at targeted loci in the genome via non-homologous end joining (NHEJ), or they can even replace a piece of endogenous DNA sequence with homologous donor DNA via homologous repair (HR) (Wei et al., 2013).

The editing efficiency shows a strong locus-to-locus variability and, might not be influenced by DNA-methylation, but by local chromatin structure. Finally, the tissue being chosen for gene-editing influences the efficiency. Gene editing is accomplished much easier in e.g. liver than in cardiomyocytes (Strong and Musunuru, 2017). TALENs and CRISPR-mediated gene editing both have their right to exist and have

been demonstrated to work well *in vivo* and *in vitro*. The application needs to decide for the method of choice.

Additionally, *in vitro* cell models, especially stem cells, utilized in disease modeling entered the limelight of gene-editing. PSCs, as mentioned above, are capable of differentiating into various cell types *in vitro* and *in vivo*, making specific gene modifications valuable for studying the biology of diseases and performing drug tests or screens without the need of animals (Horii and Hatada, 2016; Strong and Musunuru, 2017).

1.8 Aims of the thesis

This work aimed at the investigation of the effect of the CAD risk locus 9p21 on vascular calcification in an iPSC-derived VSMCs *in vitro* model. Therefore, wildtype (WT) iPSCs of both, risk (R) and non-risk (NR) donors as well as TALEN-engineered 9p21 KO for both, were differentiated into VSMCs and subsequently calcified. During the process, iPSCs, VSMCs and calcifying VSMCs were monitored and characterized regarding their cell-specific properties. Further, the degree of calcification was determined and compared between WT and KO iPSC-derived calcifying VSMCs of the risk and non-risk background. To achieve these goals the following topics were defined for the present thesis:

I. **Establishment of a protocol for directed differentiation of iPSCs towards VSMCs for large scale application *in vitro***

II. **Establishment of a calcification protocol of iPSC-derived VSMCs *in vitro***

III. **Analysis of iPSC and VSMC properties and their comparison between the different 9p21 genotypes**

IV. **Comparison of calcification properties in iPSC-derived VSMCs of different 9p21 genotypes.**

2. Material/Methods

During the completion of this thesis following students have been supervised by the author of the thesis at the Institute for Cardiogenetics:

Undine Haferkamp, Master of Science, 2016

Alexandra Rangnau, Master of Science, 2018

Ann-Selin Onuk, Bachelor of Science, 2019

Shayan Zarin-Bal, Bachelor of Science, 2019.

Images and data acquired by those students during their work are used in this thesis and figures originated by them are indicated accordingly.

2.1 Induced-pluripotent stem cell lines

GM17602/4 iPSCs were provided by the Institute of Neurogenetics, University of Luebeck, in May 2015, as healthy WT iPSCs. In 2018, we noticed a problem concerning those cells. Analyses revealed that these cells named “HFF” were derived from a female patient (Coriell Institute for Medical Research (Camden, New Jersey); GM17602/GM17604), who is a carrier of a heterozygous missense COL1A2 mutation (Gly610Cys), showing a heart phenotype as well as osteogenesis imperfecta. Cells from a donor with osteogenesis imperfecta, having an impact on ECM secretion and stability, as well as ossification and mineralization (Forlino et al., 2011), are therefore not a suitable model for *in vitro* calcification of human iPSC-derived vascular cells. However, the disease does not affect the iPSC or VSMC status, as the results are comparable with the other iPSC lines used. Therefore, another cell line, 18i-3-6, was used as a control cell line for experiments that followed. Experiments performed with the GM17602/04 (further referred to as GM iPSCs) iPSCs are indicated accordingly, as many experiments of this thesis were initially performed using this cell line (years 2015-2018). A paper was published in 2018 at Stem Cell Research containing mainly results of the GM and 18i-3-6 (see next paragraph) cell lines. As results published with

the GM cell line could not be replicated using other cell lines, the paper had to be retracted in 2020.

18i-3-6 iPSCs were obtained from WiCell (UCSD018i-3-6, arrived on 21.07.2017). Human iPSCs were adapted to Geltrex coating and mTeSR™1 (Geltrex hESC qualified, ready-to-use, GFR, Thermo Fisher Scientific, #A1569601). Medium was exchanged every day. Cells were passaged once a week at a ratio of 1:6 to 1:10 as follows: StemPro™ Accutase™ cell dissociation Reagent (Thermo Fisher Scientific, # A1110501) was applied for 5 min at 37°C. Subsequently, cells were gently lifted from the plate and transferred into 15 ml Falcons. Further, cells were centrifuged at 0.2xg for 5 mins and resuspended in mTeSR1 containing 10 µM Y-27632 and replated onto Geltrex-coated 6-well plates (Nunc® 6-well plates, Thermo Scientific, #140675). From time to time manual passaging was required to keep the culture free of spontaneously differentiating cells. Human iPSCs were cryopreserved in liquid nitrogen in special cryomedium, as displayed in table 2.

9p21 TALEN-engineered iPSCs from a patient containing both risk alleles (R, C512) and a non-risk donor (NR, HE463_7) were generated at the Scripps research Institute, La Jolla, California, and kindly provided to us (by Dr. Valentina Lo Sardo, Prof. Dr. Kristin Baldwin and Dr. Ali Torkamani). KO cells used for this thesis contained a homozygous 58kb deletion in the 9p21 CAD risk region (Fig. 11).

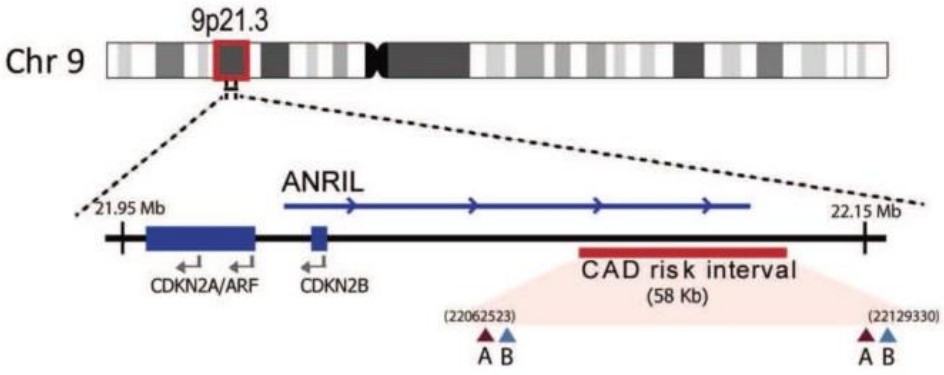

Figure 11: Demonstration of 9p21 KO region in iPSCs
A 58kb KO of the complete 9p21 CAD risk region was introduced into iPSC lines with the help of TALENs at the Scripps research institute, La Jolla (provided by Dr. Ali Torkamani).

Exact genotypes and donor information are displayed in table 1. Aliases used in this thesis are marked in bold letters. Cells were adapted to Geltrex coating and maintained

in mTeSR™1 medium with daily medium exchange. Maintenance corresponded to that of 18i-3-6 iPSCs.

Table 1: Cell line information

Cell line	9p21 risk status	9p21 Deletion	Donor information	Date of arrival
C512#17 **TAL1-2**	Risk/Risk	WT	C00512; Male; 57 years	21.09.2015
C512#17 **TAL1-5**	Risk/Risk	WT	C00512; Male; 57 years	21.09.2015
C512#17 **TAL2-3**	Risk/Risk	WT	C00512; Male; 57 years	21.09.2015
C512#17 **TAL1-9**	Risk/Risk	KO	C00512; Male; 57 years	21.09.2015
C512#17 **WB46**	Risk/Risk	KO	C00512; Male; 57 years	20.03.2019
HE463_7 **E14**	Nonrisk/Nonrisk	WT	HE463; Male; 86 years	31.01.2018
HE463_7 **E17**	Nonrisk/Nonrisk	WT	HE463; Male; 86 years	31.01.2018
HE463_7 **E50**	Nonrisk/Nonrisk	KO	HE463; Male; 86 years	31.01.2018
HE463_7 **E56**	Nonrisk/Nonrisk	KO	HE463; Male; 86 years	31.01.2018

2.2 iPSC-derived VSMCs

For differentiation of iPSCs towards VSMCs we examined two protocols that were formerly published for PSCs (Cheung et al., 2014; Xie et al., 2009), as discussed in the master thesis of Undine Haferkamp. In the process of comparing both protocols human aortic smooth muscle cells (HASMCs) served as tissue control. The differentiation protocol used for the generation of iPSC-derived VSMCs was adapted from the protocol originally published by Cheung and co-workers (Cheung et al., 2014) and optimized at our Institute. As the adaption of the protocol was part of this thesis, corresponding detailed information will be provided in the results section (for Media compositions see Table 2). Passaging or replating during differentiation was performed as described before for iPSCs. Differentiated VSMCS were passaged using Trypsin/EDTA in PBS applied for 5 min at 37°C. Cells were then lifted off the plate or flask and enzyme reaction was stopped by adding at least 1 volume of SMC medium.

Subsequently, cells were centrifuged at 0.4xg for 5 mins, resuspended in SMC medium and distributed onto freshly 0.1% gelatin-coated cell culture flasks (T75 or T175 cell+).

Table 2: Media compositions

Coating/Medium	Composition	Manufacturer
0.1% Gelatine	0.5 g gelatin (porcine)	Sigma, G1890
	500 mL phosphate buffered saline (PBS)	Lonza, BE17516Q
(Mouse embryonic fibroblast) MEF-Medium	450 mL Advanced DMEM/F12	Thermo Fisher Scientific, 12634-010
	50 mL fetal bovine serum (FBS) EU Professional	Pan Biotech, P30-8500
	5 mL GlutaMAX (200 Pi)	Thermo Fisher Scientific, 35050038
	3.5 µL 2-mercaptoethanol (50 mM)	Gibco, 31350-010
(Chemically defined Medium) CDM	250 mL Iscove's modified Dulbeccos Medium (IMDM)	Life Technologies, 12440-053
	250 mL Ham's F12 Nutrient Mix	Life Technologies, 11765-054
	5 mL Chemically defined lipid concentrate	Sigma Aldrich, G1890
	350 µL Insulin (10 mg/ml)	Roche, 11376497001
	250 µL Transferrin (30 mg/ml)	Roche, 10652202
	20 µL 1-Thioglycerol	Sigma Aldrich, M6145
	5 mL Penicillin/Streptomycin (10,000 U/ml)	Biochrome, A2213
CDM-BSA	500 mL CDM	
	2.5 g Bovine Serum Albumin (BSA)	Sigma Aldrich, A9418 - 10G
CDM-PVA	500 mL CDM	
	0.5 g polyvinyl alcohol (PVA)	Sigma Aldrich, P3186
SMC-Medium	450 mL Dulbeccos Modified Eagle's Medium (DMEM), high glucose, GlutaMAX, pyruvate	Life Technologies, 31966-047
	50 mL FBS Gold+	BioSell, FCS.GP.0500
	5 mL Penicillin/Streptomycin (10,000 U/ml)	Biochrome, A2213
iPSC Cryomedium	0.7 mL current good manufacturing practice (cGMP) mTeSR™1	Stem Cell Technologies, 85850
	0.2 mL FBS (HyClone)	GE Healthcare, SH30070.02
	0.1 mL Dimethyl sulfoxide (DMSO)	Sigma, D2650
	10 µM Y-27632	Stemcell Technologies, 72304
SMC Cryomedium	0.9 mL FBS Gold+	BioSell, FCS.GP.0500
	0.1 mL DMSO	Sigma, D2650
	10 µM Y-27632	Stemcell Technologies, 72304

2.3 Calcification of iPSC-derived VSMCs

In order to establish a calcification protocol for iPSC-derived VSMCs, various methods have been tested to find the most efficient protocol. An overview and respective reagents used in all methods applied in this thesis can be seen in table 3. As the development of the protocol was part of this thesis, further information will be provided in the results section.

Table 3: Calcification approaches applied to iPSC-derived VSMCs

Name	Medium	Calcifying Agents [conc]	Manufacturer	Duration
Pi	SMC-Medium	3.8 mM; 4mM $NaH_2PO_4 \cdot H_2O$	J.T.Baker, 4011-01	10 – 27d
β-GP + L-AP	SMC-Medium	10 mM β-glycerophosphate 0.28mM L-ascorbic acid-2-ahosphate	Sigma, G9422 Sigma, A8960	10 – 27d
Osteogenic Medium	StemXVivo Osteogenic Medium		R&D Systems, #CCM008/CCM007	30d
Osteogenic + TNFα	StemXVivo Osteogenic Medium	20 ng/mL TNFα	Peprotech, 300-01A-50	10d
Reactive Oxygen	SMC & StemXVivo Osteogenic Medium	0.4 mM H_2O_2 20 ng/mL TNFα 200 ng/mL BMP2	Merck, 1072090250 Peprotech, 300-01A-50 Peprotech, 120-02C	6 – 7d
Alves et al. 2014	SMC & StemXVivo Osteogenic Medium	1.8 mM $CaCl_2$ 20 mM HEPES 0.1 mM L-ascorbic acid-2-phosphate 10 mM β-glycerophosphate 0.1 µM dexamethasone	Sigma, C4901-100G Gibco, 15630080 Sigma, A8960 Sigma, G9422 Sigma, D-2915	7d
Tziakas et al. 2019	SMC -Medium	4 mM $CaCl_2$ 5 mM β-glycerophosphate 0.1 mM L-ascorbic acid-2-phosphate 1 µM insulin 0.1 µM dexamethasone	Sigma, C4901-100G Sigma, G9422 Sigma, A8960 Roche, 11376497001 Sigma, D-2915	7d

2.4 RNA Isolation and quantitative polymerase chain reaction (qPCR)

Messenger RNA (mRNA) isolation of cells was performed using the Qiagen RNEasy Mini Plus Kit (Qiagen, #74136) following manufacturers' instructions including DNaseI treatment. RNA concentration and purity were determined using a BioPhotometer (Eppendorf, Hamburg, Germany) and samples were stored at -80 °C until further use. Synthesis of complementary DNA (cDNA) from RNA templates via reverse transcription was performed as follows: 10µL of RNA sample adjusted to a concentration of 100 ng/µL in DNase/RNase-free water (Gibco, 10977035) was incubated for 5 min at 68 °C. 10 µL of the reaction mix for reverse transcription, containing 4µL 5x First Strand Buffer (Invitrogen, #28025021), 2µL 100 mM dithiothreitol (DTT) (Invitrogen, #28025021), and 1µL each of 4 mM 2'-deoxyribonucleosid-5'-triphosphates (dNTPs) (Promega, #U1330), Random Hexamer Primer-Mix (Roth, #HP28.1), RiboLock (40 U/µL) (Thermo Scientific, #EO0381), and M-MLV RT (200 U/µl) (Invitrogen, 28025021) was added to the RNA and incubated for 1 hour (h) at 37 °C, followed by enzyme inactivation at 95 °C for 5 min. cDNA was stored at -20 °C until further use.

Quantitative gene expression analysis, known as PCR, was performed on cDNA using a 7900HT Fast Real-Time PCR System (Applied Biosystems, #4329001) and the corresponding SDS 2.2.2 software for analysis. The reaction mix consisted of 3.75µL PowerUp™ SYBR® Green Master Mix (Life Technologies, #A25777), 1.125µL Primer mix (5 pmol/µL) and 1.125µL DNase/RNase-free water (Gibco, #10977035). The mix was added to a 384-well plate in triplicates (BioLabs, #12-40-0384-C). 1.5µL cDNA (10 ng/µL) was then added to the plate in plate accordingly. DNase/RNase-free water was used as negative control and the housekeeping gene β-Actin (or GAPDH in case of the Master thesis of Undine Haferkamp) served as internal standard (reference gene). PCR conditions were as follows: initial denaturation at 95 °C for 5 min, 40 cycles of denaturation at 95 °C for 15 sec, annealing and elongation at 60 °C for 1 min, followed by final dissociation at 95 °C for 10 min. Relative gene expression levels were calculated using the $2^{-\Delta\Delta CT}$ method. This method directly uses the threshold cycles (Cts), which are conform to the number of cycles required for the fluorescent signal to reach the threshold. Ct values were generated for each sample by the SDS 2.2.2 software, and evaluated according to the $2^{-\Delta\Delta CT}$ method (Maddocks and Jenkins,

2017). First the difference in threshold cycle between the target genes and the internal standard (β-Actin) was calculated, leading to the ΔCt value.

$$\Delta Ct = Ct(\text{target gene}) - Ct(\text{reference gene})$$

Subsequently, the difference between the target and reference sample, the ΔΔCT value, was calculated as follows:

$$\Delta\Delta Ct = \Delta Ct(\text{target sample}) - \Delta Ct(\text{reference sample})$$

The fold change due to the reference or the relative expression level is obtained as follows.

$$\text{Relative gene expression level} = 2^{\wedge -\Delta\Delta Ct}$$

Finally, the median of the expression levels of the three technical replicates per plate was estimated. At least three biological replicates were compared and plotted as dot plots using GraphPad 6.04. Expression fold changes between 0.5 and 2 are regarded as biologically irrelevant, as they can be attributed to biological variability.

2.5 Primer design

Primers for target genes were designed using the open source tool Primer3Plus and mRNA sequences from the National Center for Biotechnology Information (NCBI) database. To reduce the possibility of genomic DNA amplification in qPCR, primers were designed such that they span an exon-exon junction. Potential primer pairs were checked for sequence specificity in the human reference genome using the Primer BLAST tool from NCBI. Primer specificity was further validated through a test qPCR, including the monitoring of the standard curve and dissociation curve. Primers used are displayed in Table 4.

Table 4: Primer sequences used for qPCR

Gene	Target	Forward primer	Reverse primer
hALPL	Calcification	CCACGTCTTCACATTTGGTG	AGACTGCGCCTGGTAGTTGT
hCALD1	Smooth muscle	GAGTCCTCCAGTGTCTTGGC	GCCCTGGTTAGCTCTTCTGG
hCNN1	Smooth muscle	AGGCTCCGTGAAGAAGATCA	GTTGGCCTCAAAAATGTCGT
hCSF1	Calcification	GGAGACCTCGTGCCAATTA	TATCTCTGAAGCGCATGGTG
hCTSK	Calcification	TTCTGCTGCTACCTG	CCAGGTGGTTCATAG
hNANOG	Pluripotency	TGAACCTCAGCTACAAACAG	TGGTGGTAGGAAGAGTAAAG
hOCT4	Pluripotency	CCTCACTTCACTGCACTGTA	CAGGTTTTCTTTCCCTAGCT
hOPN/SSP	Calcification	CACTACCATGAGAATTGCAGTGA	CTGCTTTTCCTCAGAACTTCC
hRUNX2	Calcification	GACAGCCCCAACTTCCTGT	TACCCGCCATGACAGTAACC
hSOX2	Pluripotency	CCCAGCAGACTTCACATGT	CCTCCCATTTCCCTCGTTTT
hTAGLN	Smooth muscle	GTCCTTCCTATGGCATGAGC	CACCAGCTTGCTCAGAATCA
hβ-ACTIN	internal Standard	GGACTTCGAGCAAGAGATGG	AGCACTGTGTTGGCGTACAG

2.6 Protein Isolation

Adherent cells were detached by incubation with StemPro™ Accutase™ Cell Dissociation Reagent or 0.05% Trypsin/EDTA in PBS. The cell suspension was resuspended in 100 – 300 µL complete cell lysis buffer depending on the amount of cells harvested. Complete cell lysis buffer consists of 10 µL phenylmethane sulfonyl fluoride (PMSF) (Sigma, #P7626), 100µL 25x Protease Inhibitor (Roche, #1169749800), 100µL 10x cell lysis buffer (Cell Signaling, #9803) and 750µL DNase/RNase-free water (Gibco, #10977035), supplemented with 16.7µL DNase I. After adding cell lysis buffer, the suspension was incubated for 1 hour (h) at 4 °C on a shaker. The cell lysate was centrifuged at 13,000xg for 15 min at 4 °C. The supernatant containing the proteins was transferred to a new tube and stored at -80 °C until further use.

Total protein concentration was measured by the use of a colorimetric protein assay similar to Lowry assay (Biorad D_C-Assay). A protein standard series with ten defined protein concentrations ranging from 0.1 to 10µg/µL was prepared as well as the working reagent A', containing reagent S (Biorad, #500-0115) and reagent A (Biorad, #500-0113) at a ratio of 1:50. 5µL of respective standards (BioRad, #500-0007) or protein samples were added to an ELISA plate (Greiner bio-one, #756070) as duplicates. DNase/RNase-free water served as negative control. 25µL of reagent A' was added to each well followed by the addition of 200µL of reagent B (Biorad, #500-0116). After incubation in the dark for 15 min at room temperature protein concentration was measured via absorbance at 750nm using a Synergy HT Multi-Detection Microplate Reader (BioTek, Winooski, USA).

2.7 Western Blot (WB) analyses

Extracted proteins were separated according to their molecular weight by polyacrylamide gel electrophoresis using the Mini-PROTEAN® System from BioRad (Hercules, USA). The polyacrylamide gels were prepared in glass plates fixed in a casting module (BioRad, Hercules, USA) with a resolving gel of 10 to 12% depending on the molecular weight of the proteins (Compositions of reagents see Table 7). 5µL of 3x sodium dodecyl sulfate (SDS) Loading Buffer (BioLabs, #B7703S), supplemented with DTT (BioLabs, #B7703S) at a ratio of 10:1, and was added to 10µL of each sample that contains 10 µg of total protein. Samples were heated to 95 °C for 5 min and placed on ice until use. Precision Plus Protein Dual Color Standard (BioRad, #161-0374) served as a size standard. The proteins were separated for about 2 h at 100 V. For transfer to a polyvinylidene difluoride (PVDF) Immobilon-P Membrane (Millipore, #IPVH00010), proteins were blotted for 1 h at 120 V. The detection of specific proteins was performed by antibody staining. Unspecific binding sites on the membrane were blocked with 5% milk solution at 4 °C for 1 h. Subsequently, the membrane was incubated with a primary antibody (dilutions 1:300 – 1:10,000 in 5% milk) at 4 °C overnight (Tab 5).

Table 5: Primary Antibodies used for WB

Antibody	Host species	Clonality	Protein size	Dilution	Manufacturer	Catalog Number	Target
hALPL	Rabbit	Mono	57 kDa	1:10000	Abcam	ab108337	Calcification
hOCT4	Rabbit	Poly	39 kDa	1:100	Abcam	ab19857	iPSCs
hTAGLN	Rabbit	Poly	23 kDa	1:1000	Abcam	ab14106	SMCs
hβ-ACTIN	Mouse	Mono	43 kDa	1:1000	Santa Cruz	sc-47778	internal Standard
hα-Tubulin	Rabbit	Poly	50 kDa	1:1000	Abcam	Ab15246	Internal standard
hGAPDH	Rabbit	Poly	37 kDa	1:1000	Abcam	ab9485	Internal standard

This was followed by three washing steps at room temperature with Tris-buffered saline (TBS)/Tween (Tab 7) for 15 min. The membrane was incubated for 1 h with a horseradish peroxidase (HRP)-coupled secondary antibody (1:1000 – 1:5000 in 5% milk) (Tab 6.) and followed by three washing steps.

Table 6: HRP-coupled secondary antibodies used for WB

Antibody	Host species	Dilution	Manufacturer	Catalog Number
Anti-Mouse HRP linked IgG	horse	1:2000	Cell Signaling	7076S
Anti-Rabbit HRP linked IgG	goat	1:1000	Cell Signaling	7074S

For visualization of the antibody staining, ECL Prime Western Blotting Detection Reagent (GE Healthcare, #RPN2232) was directly added to the membrane and the chemiluminescence was detected by a Chemi Doc XRS BioRad imaging system (BioRad, Hercules, USA). Detected protein bands were quantified using the Image Lab Software (BioRad, Hercules, USA). β-Actin (or GAPDH in case of the Master thesis of Undine Haferkamp) served as internal standard for target protein quantification.

Table 7: Buffer compositions

Buffer	Composition	Manufacturer
10x TRIS-Borat-EDTA buffer (TBE)	121.1 g Tris Base 51.3 g boric acid 3.7 g Ethylenediaminetetraacidic acid (EDTA) bring to 1 Liter (L) with deionized water	Sigma, T6066 Sigma, B0394 Roth, 8043.1
1x TBE	10 mL 10x TBE bring to 100 mL with deionized water	
10x Electrophoresis buffer	30 g Tris base (125 mM) 144.4 g glycine (96 mM) 10 g SDS (17.5 mM) bring to 1L with deionized water	Sigma, T1503 Roth, 3790.2 Roth, 2326.1
1x Electrophoresis buffer	100 mL 10x Electrophoresis buffer bring to 1L with deionized water	
10x Transfer buffer	33 g Tris base (250 mM) 144 g glycine (1.92 M) bring to 1L with deionized water	Sigma, T1503 Roth, 3790.2
1x Transfer buffer	100 mL 10x transfer buffer 200 mL methanol (≥99%) 700 mL deionized water	 Roth, 8388.6
1x TBS pH 7.3	80 g Sodium chloride (NaCl) 12.1 g Tris base 900 mL deionized water	Roth, HN00.2 Sigma, T1503
1X TBS/Tween	100 mL 10x TBS 500 µL Tween® 20 detergent 900 µL deionized water	 Merck, 9005-64-5
Stacking Gel buffer	48 mL 0.5 Tris Hydrochloric acid (HCl, pH 6.8) 2 mL 10% SDS	
Resolving gel buffer	48 mL 1.5 M Tris HCl, pH 8.8 2 mL 10% SDS	
10% (Ammonium persulfate) APS	1 g Ammonium peroxydisulfate 10 mL deionized water	Roth, 9592.3

2.8 Immunofluorescence (IF) staining

Detection and visualization of the distribution of target proteins within cultured iPSCs or iPSC-derived VSMCs was performed by immunofluorescence staining. For IF analysis cells were grown on Nunc™ Lab-Tek™ II Chamber Slides™ (Thermo Scientific, #154534) at a seeding density of $0.5x10^4$ to $2x10^4$ cells per cm^2. Cells were washed with PBS and then fixed 30 minutes (mins) with chilled (-20 °C) methanol:acetone (1:1). A Dako Pen (Dako, #S2002) was used to outline the wells, to avoid antibody solutions to run from one well to the other. For antibody staining, cells were permeabilized in PBS containing 0.1% Triton-X100 (Sigma Aldrich, #T-8787) and 1% BSA, and blocked with PBS containing 3.5% BSA. 100µL primary antibody diluted in PBS (1:300 – 1:500) or PBS alone in case of the negative control, was applied to each well and incubated overnight at 4 °C (Tab. 8).

Table 8: Primary antibodies used for IF

Antibody	Host species	Clonality	Dilution	Manufacturer	Cat.No	Target
hCNN1	Mouse	Mono	1:500	Sigma	C2687	VSMC
hKi67 (marker of proliferation Ki67)	Mouse	Mono	1:300	BD Pharmingen	556003	Proliferation
hNANOG	Rabbit	Mono	1:300	Cell Signaling	4903	Pluripotency
hTAGLN	Rabbit	Poly	1:500	Abcam	ab14106	VSMC

Slides were washed three times for 5 min in PBS and incubated with a secondary antibody (1:300 – 1:500) diluted in PBS for 1 h at room temperature (Tab. 8). Used secondary antibodies were conjugated to a fluorescent dye (Alexa Fluor®) for target protein detection.

Table 9: Secondary antibodies used for IF

Antibody	Fluorochrome	Host species	Dilution	Manufacturer	Catalog Number
Anti-rabbit IgG	Alexa 488	Donkey	1:300	Invitrogen	A21206
Anti-mouse IgG	Alexa 488	Goat	1:500	Invitrogen	A11029
Anti-mouse IgG	Alexa 568	Donkey	1:500	Invitrogen	A10037

Subsequently, cells were washed three times for 5 min in PBS. To counterstain the nucleus of the cells, the blue-fluorescent stain 4',6-diamidino-2-phenylindole (DAPI) was used, which binds to double stranded DNA. Slides were incubated in the dark for 15 min with 0.1 µg/mL DAPI solution and washed with deionized water. The slides were covered using Dako Fluorescence mounting medium (Dako, #S3023) and cover slips (Menzel, #9161060). The detection of IF staining was performed with a BZ-9000 BioRevoTM fluorescence microscope (Keyence, Neu-Isenburg, Germany).

2.9 Proliferation-Assay

For proliferation analyses, cells were stained in IF for the proliferation marker Ki67. Nuclei were counterstained with DAPI. DAPI+ and Ki67+ cells were counted, and Ki67+ cells normed on DAPI count. Results are presented as % of Ki67+ cells of at least three independent biological replicates.

2.10 Migration-Assay

For Migration analysis, a scratch assay was established at our Institute. Cells were seeded in a 12-well plate format and cultivated until confluent. With the use of a 100 µL tip, a scratch through the cell layer was placed vertically in each well and one phase contrast image was taken at previously specified positions in each well using an Olympus IX70 inverted microscope and CellSens Software. After 24h new images at the same positions were taken. Using CellSens Software the Confluency Checker tool was used to calculate the confluency at 0h and 24h. All time points included in the experiment were processed and confluency was analyzed. The difference between the confluency of 0h and 24h was set equal to migration rate in percent. Three independent biological replicates were analyzed.

2.11 Calcein and Alizarin Red S staining

Calcium phosphate depositions within cultured iPSC-VSMCs were detected by Calcein ($C_{30}H_{26}N_2O_{13}$), a fluorescent chromophore that specifically binds to Ca^{2+} (Du et al., 2001). Cultured cells were washed with PBS once and fixed in chilled (4°C) 4% paraformaldehyde (PFA) for 30 mins. Cells were then incubated with Calcein staining solution (Sigma, #C0875) for 30 min in the dark, washed 3 times with 50 mM TBS (pH 9) for 3 min each and DNA was counterstained with DAPI for 10 min in the dark. Cells were covered with 400µL 50 mM TBS (pH 9) and Calcein fluorescence was detected immediately after staining by using a BZ-9000 BioRevoTM fluorescence microscope (Keyence, Neu-Isenburg, Germany).
Alizarin Red S (ARS) staining was performed using the Osteogenesis quantitation kit (Merck Millipore, # ECM815), following the manufacturers' instructions. Stained cells were imaged using the BZ-9000 BioRevo^{TM} fluorescence microscope (Keyence, Neu-Isenburg, Germany).

2.12 Calcein Quantification

For quantification of calcium deposits, Calcein stainings were used for analyses. Using a python script (Appendix), kindly provided by Tobias Reinberger, Institute for Cardiogenetics, DAPI Intensity and pixel count, as well as Calcein Intensity and pixel count were estimated. Calcein was then normed to DAPI (Intensity Calcein/DAPI pixel count). Untreated VSMCs were used as reference.

2.13 Calcium Assay

In order to determine the CaP concentration, the cells were washed twice with PBS and incubated with 0.6 normal (N) HCl overnight at 4°C. On the next day, CaP content in the supernatant was determined following the protocol of the Randox Calcium quantification assay (Randox, #CA590). At a certain time point we observed technical

problems applying this method of calcium quantification. We therefore only proceeded using the Calcein Quantification.

2.14 Statistical Analyses

Data are presented as dot plots showing all points, unless otherwise stated including the median represented by horizontal bars. Unpaired t-tests using a Welch's correction were performed using GraphPad Prism 6.04.

$P < 0.05$ was considered statistically significant. For all tests: *$P < 0.05$, **$P < 0.01$, ***$P < 0.001$, ****$P < 0.0001$, and p-values are indicated for not significant (n.s.), unless stated otherwise.

Statistic outliers were identified using GraphPad outlier test and excluded from the analyses.

3. Results

3.1 Generation of iPSC-derived VSMCs *in vitro*

In order to allow iPSC-based *in vitro* examinations of cell lines edited for atherosclerosis-associated risk locus 9p21, a joint protocol for the differentiation of iPSCs towards lateral-mesoderm originated VSMCs and their subsequent calcification was necessary. First of all, we started the adaptation of the differentiation protocol with the GM and 18i-3-6 iPSCs into VSMCs, as described in the following section.

3.1.1 Differentiation of iPSCs towards VSMCs *in vitro* – Protocol establishment at our Institute

Initially, it is important to mention that at the Institute of Cardiogenetics there was no protocol established for the generation of iPSC-derived VSMCs. Therefore, we had to find the protocol that was working the best. We chose two published differentiation protocols to compare. The first one was published by Xie and colleagues in 2009 (in the following section termed Protocol X), the second one by Cheung et al. 2014 (in the following section termed Protocol C). The comparison of both protocols was performed by Undine Haferkamp during her Master thesis, using the GM iPSCs in the context of this thesis.

Protocol X (Xie et al., 2009) describes an undirected differentiation. Shortly, iPSCs are adapted to PSC culture medium (450mL Advanced DMEM/F12 + 75mL FBS + 50 mM 2-mercaptoethanol + 200 mM GlutaMAX + 10 mM non-essential amino acids (NEAA)) supplemented with 12 ng/mL FGF2 and 10 ng/mL activin A. For induction of differentiation cells were passaged with StemPro™ Accutase™ as described before, and replated on gelatin-precoated plates at a density of $4x10^4$ cells/cm^2 in differentiation medium. Differentiation medium consisted of Advanced DMEM + 10% FBS + 50 mM 2-mercaptoethanol + 200 mM GlutaMAX + 10 mM NEAA supplemented with 10 nM retinoic acid (RA). Medium was replaced every day until d10. After d10, differentiation was determined, and cells were switched to SMC medium

made up of DMEM + GlutaMAX (high glucose) + 10% FBS + 10 mM NEAA and cultured until further use. An overview of the protocol is shown in figure 12.

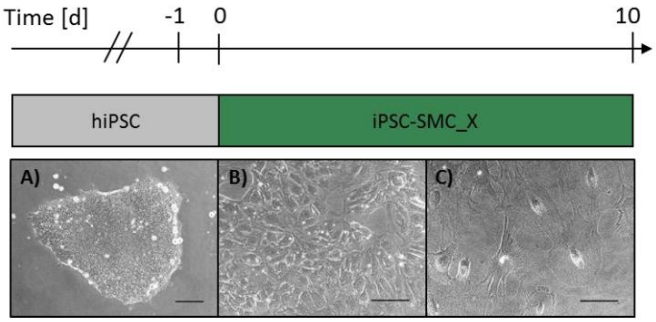

FIGURE 12: Overview of Protocol X (adapted from Xie et al. 2009)
Prior to differentiation, iPSCs were expanded until 70% - 80% confluency. One day before induction of the differentiation (d-1), cells were cultured in PSC-medium supplemented with 12 ng/mL FGF2 and 10 ng/mL activin A. On d0 cells were replated and cultured in differentiation medium supplemented with 10 nM RA until d10. Each differentiation step is represented by brightfield images. The figure was generated by Undine Haferkamp.

Protocol C on the other hand, described a more detailed and complex, lineage-specific differentiation protocol. The protocol regarding the generation of lateral mesoderm-originated VSMCs out of human pluripotent stem cells published by Cheung et al., 2014 proved less efficient to produce high numbers of VSMCs in our hands. Therefore, slight changes were introduced into the original protocol (Fig. 13) as described in the following section.

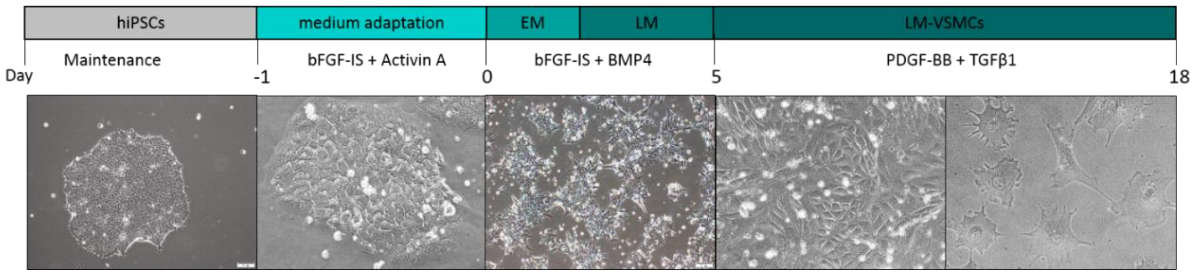

FIGURE 13: Differentiation Protocol of iPSCs towards lateral-mesoderm derived VSMCs (adapted from (Cheung et al., 2014)).
Prior to differentiation, iPSCs were expanded until 80% - 90% confluency. One day before induction of the differentiation (d-1), cells were cultured in CDM-BSA supplemented with 12ng/mL bFGF-IS and 0.1 ng/mL activin A. On d0 cells were replated at a ratio of 1:2-1:3 and cultured in CDM-PVA supplemented with 20 ng/mL bFGF-IS and 0.1 ng/mL BMP4 until day 1.5, where they reach early mesoderm (EM) identity. Until d5, where they reach lateral-mesoderm (LM) identity, 50 ng/mL BMP4 and 20ng/mL bFGF-IS were added. On d5 cells were replated at 20,000 cells/cm^2 and cultivated in CDM-PVA with 10 ng/mL PDGF-BB and 2 ng/mL TGFβ1 supplementation until d18. Each differentiation step is represented by brightfield images. The figure was generated by Undine Haferkamp.

The original protocol describes a medium adaptation to CDM-BSA for a couple of days, followed by replating the cells to gelatin-coated plates at a 1:10 ratio (Cheung et al., 2014). However, in our hands iPSCs showed increased cell death. Therefore, the duration until iPSCs reached 70% confluency again, was too long. In the end, 1d of adaptation to CDM-BSA medium, supplemented with 12 ng/mL FGF2-IS and 0.1 ng/mL activin A, proved sufficient in our case. On d0, Cheung and colleagues split cells very sparse. We noticed, that a lower splitting ratio of 1:2 to 1:3 that set the cells at around 75-80% confluency, notably improved the differentiation efficiency of our iPSCs. The cells were then kept in CDM-PVA for the whole differentiation process as described in the original protocol (Cheung et al., 2014). From d0 until d1.5, differentiation towards early mesoderm (EM) property is initiated by the addition of 20 ng/mL FGF2-IS, 10 µM LY294002, and 10 ng/mL BMP4, as reported (Cheung et al., 2014). Between d1.5 and d5, early mesoderm progenitors develop into LM progenitors by adding 20 ng/mL FGF2-IS and 0.5 ng/mL BMP4 (Cheung et al., 2014).

Starting from d5 until d18 Cheung and colleagues recommended to perform only changes of 50% of the medium every other day, supplemented with 10 ng/mL PDGF-BB and 2 ng/mL TGFβ1 (Cheung et al., 2014). We instead noted a complete medium exchange every second day in order to wash out all dead cells notably improved cell viability (data not shown). After 18d, generated iPSC-derived VSMCs were characterized, cryopreserved in liquid nitrogen or further cultured for calcification and other assays in SMC maintenance medium. During differentiation we did not experience the necessity to replate cells of the GM iPSCs. With other cell lines, like 18i-3-6 or C512 we did observe the necessity to replate cells at a ratio of 1:2 to 1:3 between d8 and d14 of differentiation. For that cells were detached using StemPro™ Accutase™, centrifuged at 0.4xg for 5 mins and resuspended as single cell solution in CDM-PVA containing PDGF-BB and TGFβ1. Plates were prepared as described before for the differentiation.

VSMCs resulting from both differentiation protocols were tested for the expression of pluripotency-associated markers as well as SMC markers. Human aortic smooth muscle cells (HASMCs) served as control.

On RNA level, the expression of pluripotency-associated markers *NANOG, OCT4,* and *SOX2* were downregulated in human aortic HASMCs and in VSMCs of Protocol X as well as Protocol C (Fig. 14).

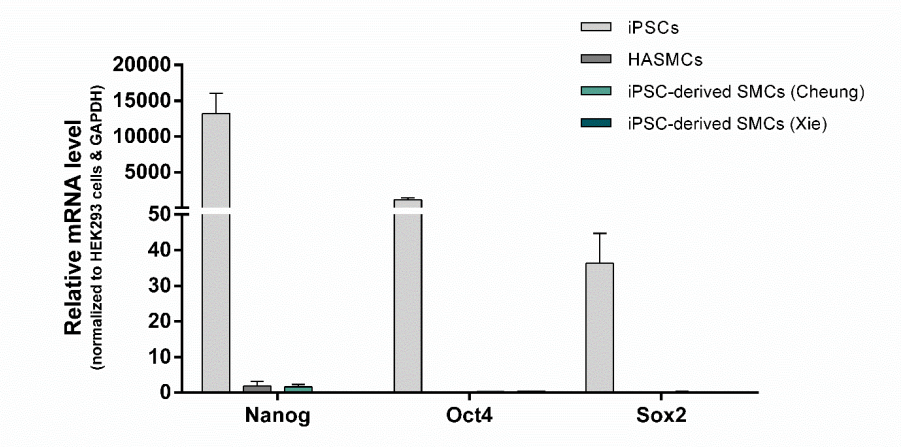

FIGURE 14: RNA expression of pluripotency markers in cells derived from Protocol X and C
Pluripotency-associated markers are downregulated in HASMCs (dark grey), and SMCs derived from Protocols X and C (green) compared to iPSCs (light grey). Data are presented as bar diagrams +standard deviation (SD). The figure was generated by Undine Haferkamp.

Further, we analyzed the RNA expression of SMC-specific markers *CNN1, TAGLN,* and *CALD1*. All markers were upregulated in iPSC-derived VSMCs (Fig. 15).

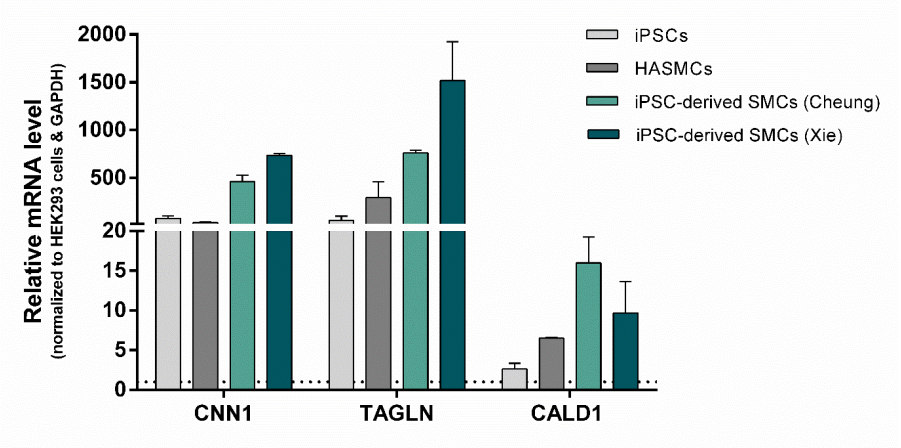

FIGURE 15: RNA expression of SMC markers in cells derived from Protocol X and C
SMC-specific markers are upregulated in iPSC-derived SMCs from Protocols X and C (green) compared to iPSCs (light grey). HASMCs show a moderate upregulation (dark grey). Data are presented as bar diagrams +SD. The figure was generated by Undine Haferkamp.

Further, we analyzed the protein expression of OCT4 and TAGLN (SM22α). As expected OCT4 expression was downregulated in HASMCs and iPSC-derived VSMCs (Fig. 16 A/B), while TAGLN (SM22α) was upregulated (Fig.16A/C).

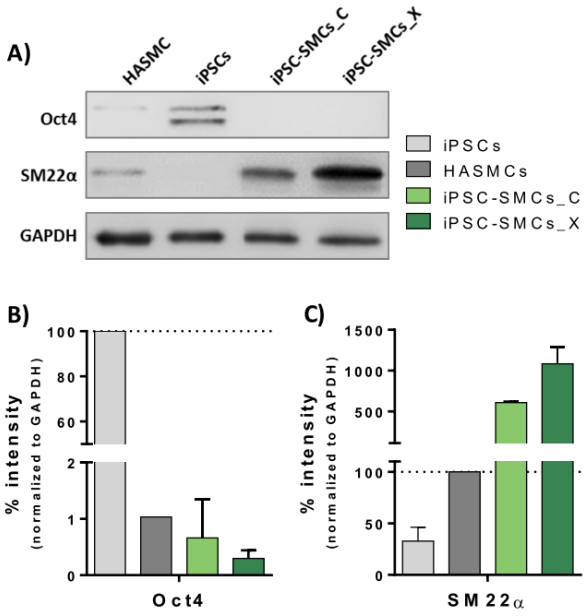

FIGURE 16: Protein expression of SMC markers in cells derived from Protocol X and C
A) Representative WB images. Glyceraldehyde 3-phosphate dehydrogenase (GAPDH) was used as internal standard.
B) OCT4 protein expression was downregulated in HASMCs (dark grey), as well as iPSC-derived SMCs (green) of both protocols, compared to iPSCs (light grey).
C) SM22α is upregulated in iPSC-derived SMCs (green) of both protocols compared to HASMCs (dark grey). Human iPSCs show a downregulation of protein expression of SM22α.
Data are presented as bar diagrams +SD. The figure was generated by Undine Haferkamp.

Both protocols lead to the generation of iPSC-derived VSMCs, as shown above. Critical parameters, as the downregulation of pluripotency-marker expression as well as upregulation of SMC-maker expression on RNA and protein level were confirmed for both protocols.

However, Protocol X (Xie et al., 2009) is based on serum and represents an undirected approach, while Protocol C (Cheung et al., 2014) is serum-free and allows the directed differentiation of lineage-specific VSMCs. We decided to use Protocol C (Cheung et al., 2014) with the modifications introduced to the original protocol, as described in the beginning of this section to obtain lineage-specific VSMCs in a directed manner for further experiments.

3.1.2 Adaptation of the Cheung protocol on 18i-3-6 cells and characterization of their iPSCs and iPSC-derived VSMCs

Human iPSCs of the 18i-3-6 cell line were differentiated into VSMCs using the adapted protocol from Cheung and coworkers, already described in section 3.1.1. Human iPSCs and iPSC-derived VSMCs were characterized on morphological as well as molecular level. Morphologically, iPSCs and VSMCs are easily distinguishable. Characteristic for iPSCs is their colony forming growth with rather round shaped cells. Those cells sit tightly together, often referred to as cobblestone-like and display notably big nuclei in combination with very little cytoplasm (Fig. 17A). VSMCs on the other hand are much bigger. Depending on the growth space available and their phenotype, they display a star- or stellate shape. Compared to iPSCs they display much more cytoplasm and grow as single cells (Fig. 17B).

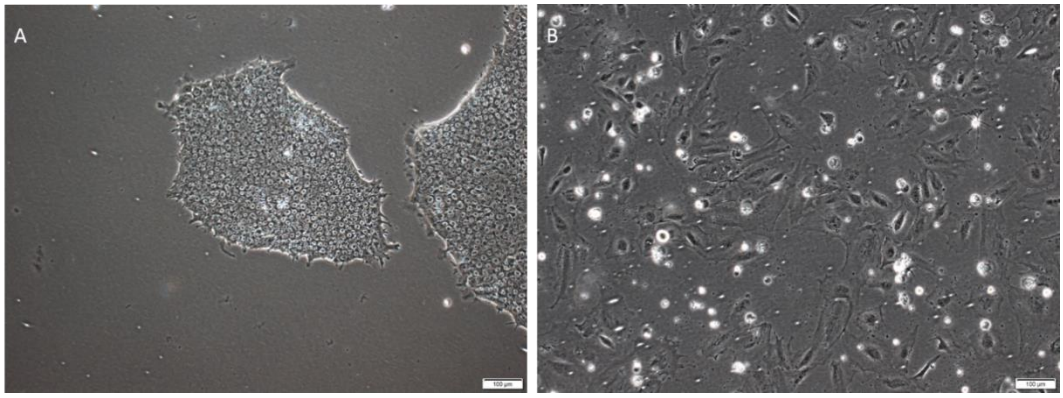

FIGURE 17: Bright field images of 18i-3-6 iPSCs and iPSC-derived VSMCs
A) Typical for iPSC colonies is the cobblestone-like appearance of the cells. Induced PSCs usually contain a big nucleus compared to minimum cytoplasm. Most of the times iPSC colonies grow round shaped.
B) IPSC-derived VSMCs are much bigger than the iPSCs. Their typical shape is either star- or stellate shaped depending on growth space available and the phenotype they display. Scale bars represent 100 micrometer (µm).

As described in sections 1.5, 1.6, and 3.1.1 both iPSCs and VSMCs express marker genes typical for their identity. On RNA level we could show that the pluripotency markers *NANOG*, *OCT4,* and *SOX2* were significantly downregulated in iPSC-derived VSMCs compared to 18i-3-6 iPSCs (Fig. 18A). The SMC-markers *CALD1*, *CNN1,* and *TAGLN* on the other hand were significantly upregulated in iPSC-derived VSMCs compared to iPSCs (Fig. 18B).

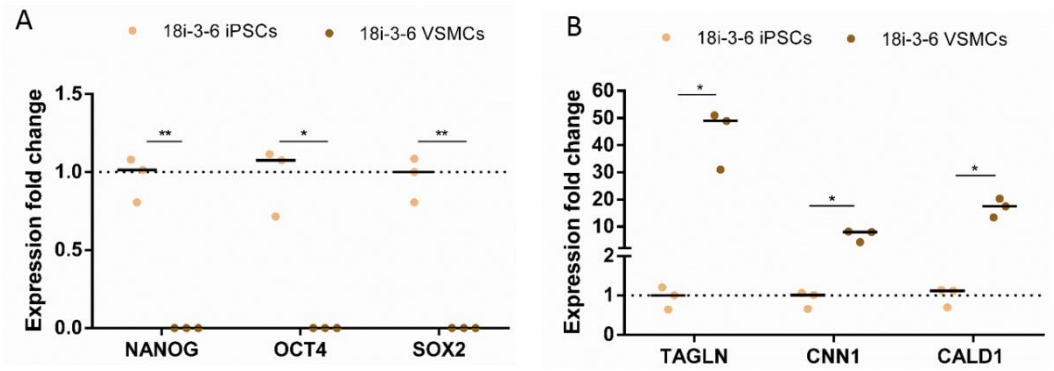

FIGURE 18: RNA expression analysis of 18i-3-6 iPSCs and iPSC-VSMCs
A) RNA expression analyses show downregulation of the pluripotency markers *NANOG, OCT4,* and *SOX2* in iPSC-derived VSMCs compared to iPSCs.
B) The SMC-marker genes *CALD1, CNN1,* and *TAGLN* were upregulated in iPSC-derived VSMCs compared to iPSCs. Each dot represents median of three technical replicates.

In order to confirm the findings from RNA level on protein level, WB analyses for OCT4 and TAGLN were performed, and corresponding protein expression was quantified. Similarly, to the RNA expression we were able to show on protein level that OCT4 as pluripotency marker was significantly downregulated in iPSC-derived VSMCs, while TAGLN as SMC marker was significantly upregulated in iPSC-derived VSMCs after *in vitro* differentiation (Fig. 19).

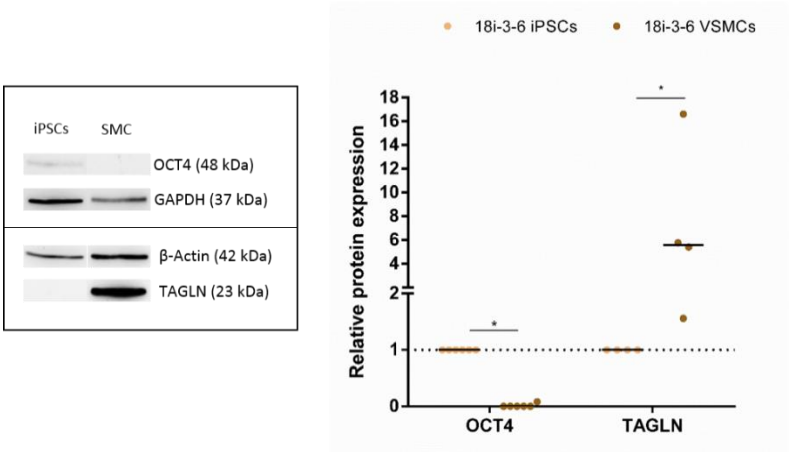

FIGURE 19: Protein expression of OCT4 and TAGLN in 18i-3-6 iPSCs and iPSC-derived VSMCs
Protein analyses show the downregulation of OCT4 expression in iPSC-derived VSMCs and the upregulation of TAGLN in 18i-3-6 iPSC-derived VSMCs compared to iPSCs. Representative Blots are displayed on the left. Each dot represents one biological replicate.

After checking for the specific expression of characteristic markers, we wanted to assure that the proteins are located in the right compartments. Therefore, we performed IF stainings for NANOG as pluripotency-associated marker. NANOG as a

transcription factor is highly expressed in the nucleus of pluripotent cells that was confirmed for 18i-3-6 iPSCs (Fig. 20).

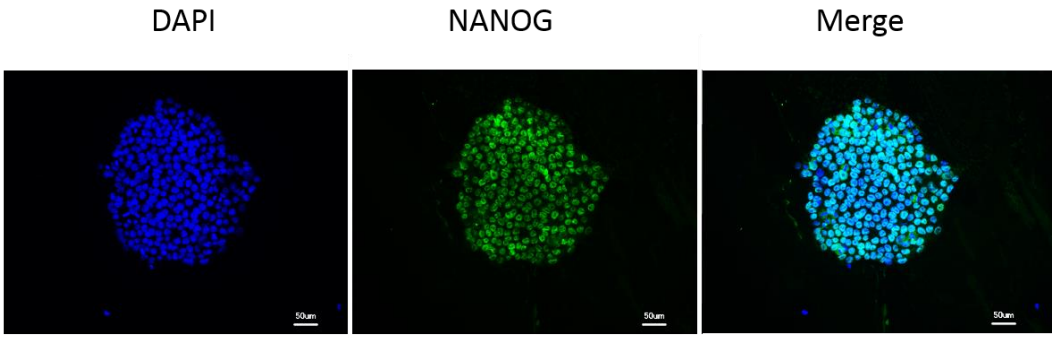

FIGURE 20: Characterization of 18i-3-6 iPSCs in IF
The 18i-3-6 iPSC line was stained against NANOG (green) and nuclei were counterstained with DAPI (blue). NANOG is highly expressed in the nuclei of iPSCs, as seen in the overlay (merge). Scale bars represent 50 µm.

To assure correct localization of SMC markers, iPSC-derived VSMCs of 18i-3-6 iPSCs were stained against TAGLN and CNN1. TAGLN and CNN1 are highly expressed in the cytoplasm and cytoskeleton, especially localizing in the contractile fibers (Fig. 21).

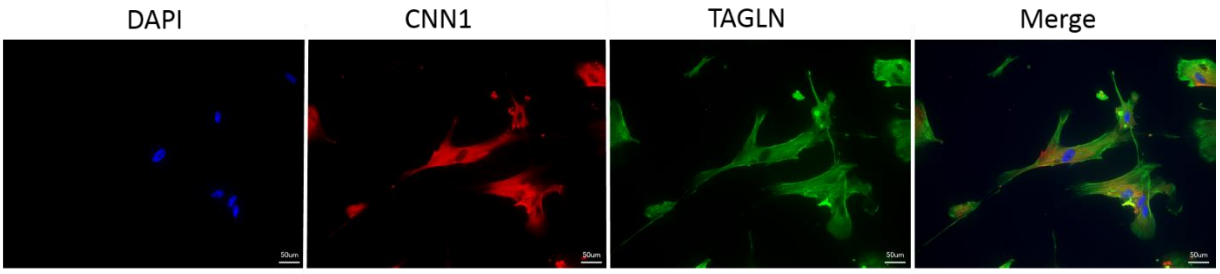

FIGURE 21: Characterization of 18i-3-6 iPSC-derived VSMCs in IF
18i-3-6 iPSC-VSMCs show the expression of VSMC marker proteins TAGLN (green) and CNN1 (red) in the cytoplasmic compartment of the cells. Nuclei are stained with DAPI (blue). The overlay (Merge) shows the colocalization of CNN1 and TAGLN in all cells. Scale bars represent 50 µm.

As we intended to estimate the differentiation efficiency, we analyzed the IF stainings of iPSC-derived VSMCs for the colocalizing expression of CNN1 and TAGLN. All DAPI positive cells were counted and set to 100%. Following, the CNN1 and TAGLN positive cells were counted and the percentage of positive cells compared to DAPI positive cells was estimated, resulting in an overall differentiation efficiency of more than 95% (Fig. 22).

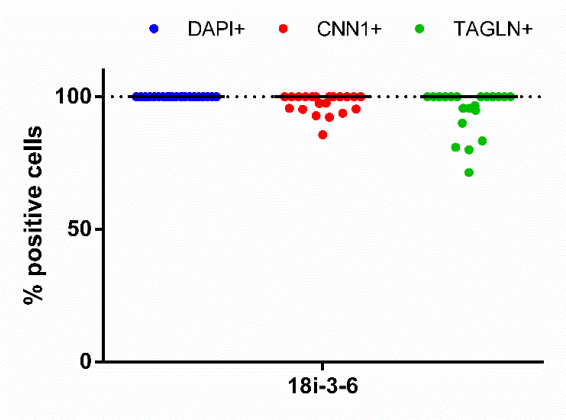

FIGURE 22: Estimated differentiation efficiency in 18i-3-6 iPSC-VSMCs
Immunofluorescence images of 18i-3-6 VSMCs stained against CNN1 and TAGLN were analyzed regarding their percentage of TAGLN+ and CNN1+ cells. TAGLN and CNN1 co-expression is above 95% for most of the 18i-3-6 VSMCs. Dots represent % positive cells per image analyzed; n=5 biological replicates

Altogether, we managed to differentiate the 18i-3-6 iPSCs with an even higher efficiency than originally reported by Cheung and colleagues (Cheung et al., 2014). The characterization of the 18i-3-6 iPSCs and VSMCs showed, that pluripotency markers like OCT4, NANOG, and SOX2 were significantly downregulated during the process of differentiation on RNA as well as protein level. The SMC markers CALD1, CNN1, and TAGLN on the other hand were significantly upregulated during the course of differentiation, reaching their highest expression level in iPSC-derived VSMCs.

3.1.3 Functional characterization of iPSC-derived VSMCs

Finally, iPSC-derived VSMCs needed to be characterized for their functional values like migration and proliferation, which are relevant atherosclerotic parameters.
For VSMC migration a scratch assay was established in our lab and performed with iPSC-derived VSMCs from at least three independent differentiation approaches (three biological replicates). Human iPSC-derived VSMCs of the 18i-3-6 cell line do migrate notably within 24h (Fig. 23).

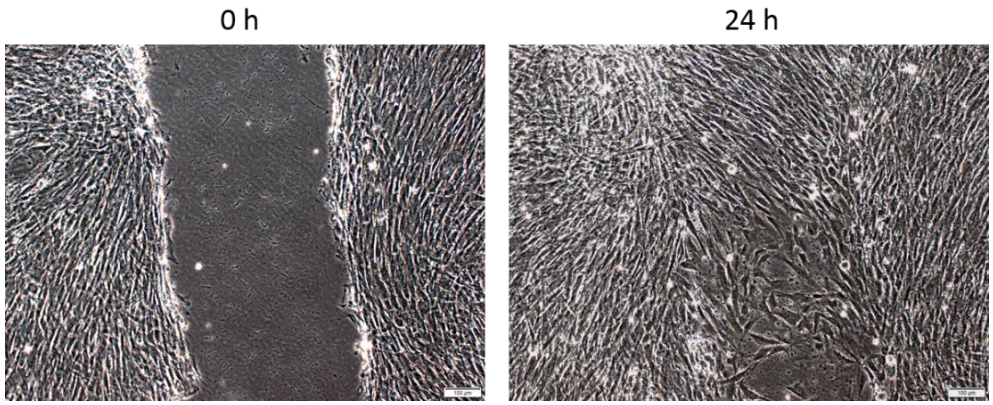

FIGURE 23: Migration of 18i-3-6 iPSC-VSMCs
Brightfield images of 18i-3-6 VSMCs show strong migration within 24h using a scratch assay. Scale bars represent 100 µm. n=3 biological replicates.

Further, migration was quantified using the tool Confluency checker of the CellSens Software. The analysis of the brightfield images taken at 0h and 24h showed a highly significant increase in confluency that was set equivalent to migration. The difference between 0h and 24h was defined as migration rate [%], which has a median of 42.25% for 18i-3-6 cells with notable variation (Fig. 24).

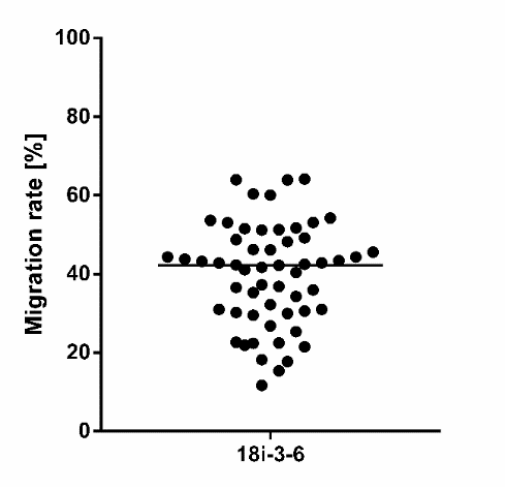

FIGURE 24: Migration rate of 18i-3-6 iPSC-VSMCs
Quantification of migration of 18i-3-6 VSMCs shows a migration rate of 42.25% within 24h using a scratch assay. Each dot represents the migration rate per well analyzed.

For proliferation 18i-3-6 iPSC-derived VSMCs were seeded on cover slides and stained for Ki67. Ki67 positive cells were counted and related to DAPI count. We observed a proliferation rate of around 21% in 18i-3-6 iPSC-derived VSMCs (Fig. 25).

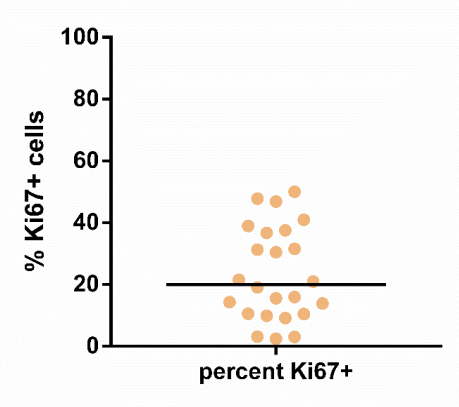

FIGURE 25: Proliferation of 18i-3-6 iPSC-VSMCs
18i-3-6 iPSC-derived VSMCs show an estimated proliferation rate of around 20%. Each dot represents the percentage of Ki67+ cells per image analyzed.

18i-3-6 iPSC-derived VSMCs show a proliferation rate of around 21% and a migration rate of around 42%.

3.2 Establishing a calcification protocol of iPSC-derived VSMCs *in vitro*

As to date there are several publications showing the calcification of VSMCs, mesenchymal stem cells or other cell types of different origin *in vitro* (Alam et al., 2009; Bansal, 1990; Byon et al., 2008; Demer et al., 1994; Proudfoot et al., 2000; Tziakas et al., 2019; Yang et al., 2004). However, so far there are no protocols describing the calcification of human iPSC-derived VSMCs *in vitro*. Therefore, it was necessary to examine various approaches to find the method with the highest efficiency. Those approaches will be described in the following section.

3.2.1 Inorganic Phosphate and β-GP/L-AP Treatment

The following experiment was performed in GM iPSCs by Undine Haferkamp during her Master thesis in the context of this work.

After the characterization of iPSC-derived VSMCs, they were used for subsequent calcification *in vitro* using two stimuli: 3.8 mM Pi and the combination of 10 mM beta-glycerophosphate (β-GP) and 0.28 mM L-ascorbic acid phosphate (L-AP). For the generation of calcifying vascular cells, VSMCs were plated on 0.1% gelatin-coated Nunc® 12-well plates for calcification at a density of 40,000 cells/well in SMC medium until they reached 95% confluency. For the initiation of calcification in iPSC-derived VSMCs two approaches were tested as well as the influence on the calcification during differentiation was analyzed. We developed a protocol to test, whether it made a difference in the calcification outcome if cells were initiated with the start of differentiation from iPSCs into VSMCs (d0) and after differentiation (d17) (Fig.26A). Therefore, either 3.8 mM Pi or the combination of 10 mM β-GP and 0.28 mM L-AP was added to the medium for a duration of 10 or 27d respectively (Fig.26). Afterwards, the calcium concentration was measured, showing an increase in calcium concentration for cells treated with Pi. Treatment with β-GP/L-AP did not result in significantly elevated calcium levels (Fig. 26B/C). For treatment with Pi, no difference could be seen when cells were supplemented with calcifying agents on d0 vs d17 of differentiation towards VSMCs (Fig. 26B/C).

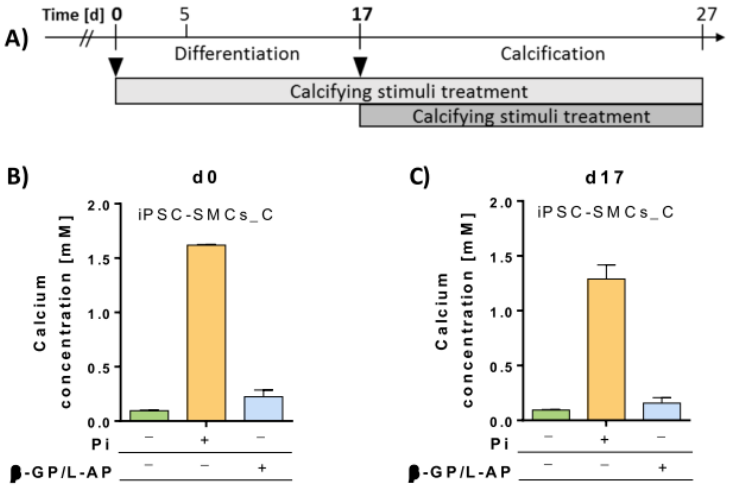

FIGURE 26: Calcification of iPSC-derived VSMCs during and after differentiation using Pi and β-GP/L-AP

A) Schematic view of differentiation in combination with calcification treatment.
B) Calcium assay of calcification starting from d0 of differentiation resulted in increase of calcium concentration for Pi treatment, but not for β-GP/L-AP treatment.
C) Calcium assay of calcification starting from d17 of differentiation resulted in increase of calcium concentration for Pi treatment, but not for β-GP/L-AP treatment.

Data are presented as bar diagrams +SD. Figure was generated by Undine Haferkamp.

Further, samples were stained with Calcein in order to confirm the results from the calcium assay. After induction of calcification on d0 of differentiation, β-GP/L-AP treatment did not result in a positive Calcein staining (Fig. 27 middle). Pi treated cells show very little Calcein signal (Fig.27 bottom). Untreated cells were used as control, and did not show a positive staining (Fig. 27 top).

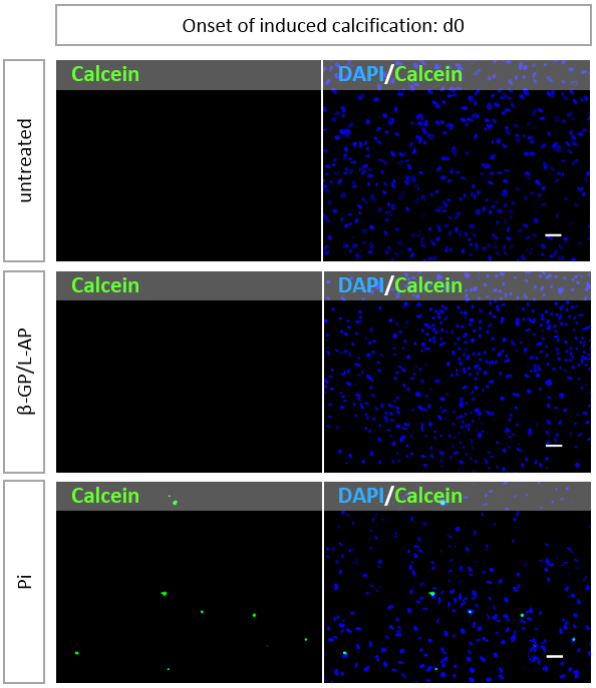

FIGURE 27: Calcein staining of calcification induced on d0 of VSMC differentiation
Untreated controls (top) as well as β-GP/L-AP treated cells (middle) did not show positive Calcein staining (green, left). Pi treated cells show very little positive staining (bottom). Cells were counterstained with DAPI (blue, right). Scale Bars represent 100 µm. Images were taken and Figure was generated by Undine Haferkamp.

The same staining was performed for cells where calcification was induced on d17 of differentiation. Again, untreated controls show no Calcein staining (Fig. 28 top). The combination of β-GP/L-AP show very few Calcein signals (Fig. 28 middle), and Pi-treated cells show slightly more positive Calcein staining (Fig. 28 bottom).

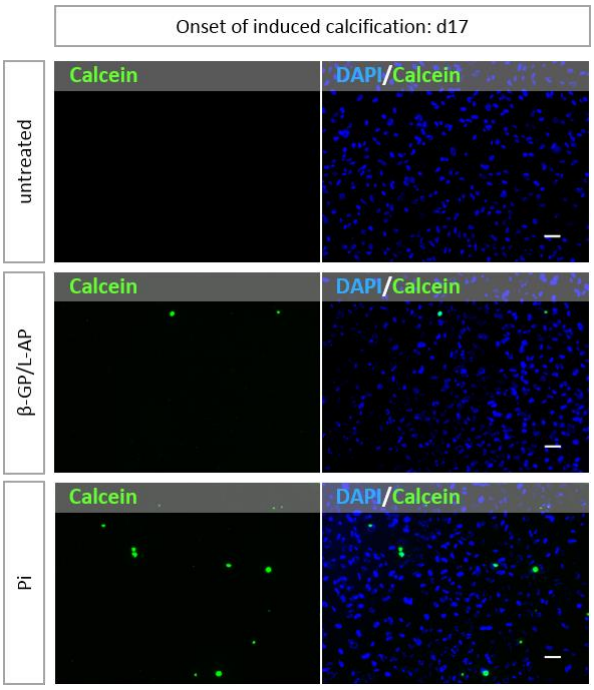

FIGURE 28: Calcein staining of calcification induced on d17 of VSMC differentiation
Untreated controls (top) did not show positive Calcein staining (green, left). The combination of β-GP/L-AP (middle) and Pi treatment (bottom) showed little positive staining. Cells were counterstained with DAPI (blue, right). Scale Bars represent 100 µm. Images were taken and figure was generated by Undine Haferkamp.

Finally, the expression of the calcification-associated marker *OPN* was examined in cells where calcification was induced on d17 (Fig. 29). Neither Pi treatment, nor β-GP/L-AP treatment showed an upregulation in *OPN* expression on RNA level compared to untreated controls (Fig. 29).

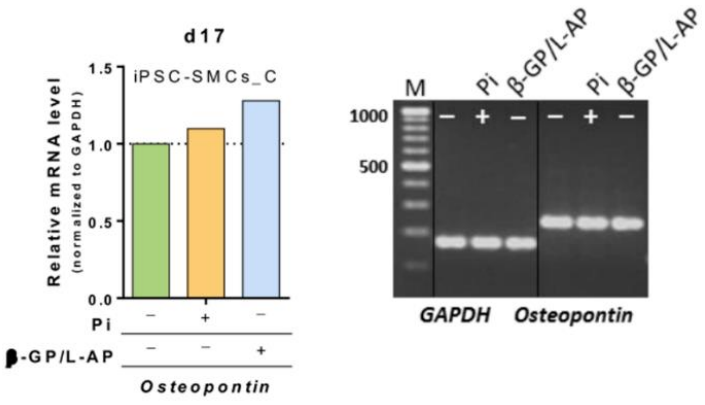

FIGURE 29: Expression analysis of *OPN* in calcified VSMCs from d17
Cells that were calcified from d17 of differentiation for a duration of 10d did not show an upregulation of *OPN* expression on RNA level. A representative gel image is displayed on the right side. Data are presented as bar diagram. The figure was generated by Undine Haferkamp.

In summary, the onset of calcification before (d0) or after (d17) differentiation of iPSC-derived VSMCs does not make a difference in calcium content, Calcein staining or osteogenic marker expression. Pi was able to increase the calcium content in both experiments, but did not show positive Calcein staining, and was not able to induce an upregulation of *OPN* expression on RNA level. The combination of β-GP and L-AP did not show an increase in calcium concentration, Calcein staining or *OPN* expression in this setting.

3.2.2 StemXVivo™ Osteogenic Medium

The following experiments were carried out in GM iPSCs and results were published in Stemcell Research in August 2018 (Trillhaase et al., 2018) . Unfortunately, due to scientific misconduct of a collaborator and therefore, not reproducible results, the publication was retracted in 2020 (retracted 2020).

For calcification, iPSC-derived VSMCs were replated at a density of 52,000 cells/cm^2 in Nunc® 24-well cell culture plates and cultured in StemXVivo® human osteogenic medium (R&D Systems, #CCM008/CCM007; referred to as osteogenic medium) for 30d. Medium was exchanged twice a week to reduce shear stress. After 30d the calcification was investigated, analyzing the amount of CaP deposits using Calcein (Fig. 26A) and ARS staining (Fig. 26A). Cells treated with osteogenic medium show high amounts of CaP deposits, represented by bright Calcein staining, whereas control cells show no Calcein staining signal (Fig. 30A). ARS staining shows bright red colour in calcified, osteogenic medium-treated cells, while VSMCs kept in SMC-medium appear in fade red to yellow (Fig. 30A). Additionally, the degree of calcification was quantified using a Randox Calcium quantification kit. Differences between treated and untreated cells observed in the Calcein and ARS staining were confirmed by this quantification, showing increased CaP levels in treated cells up to 5.5 times higher than in control cells (Fig. 30B).

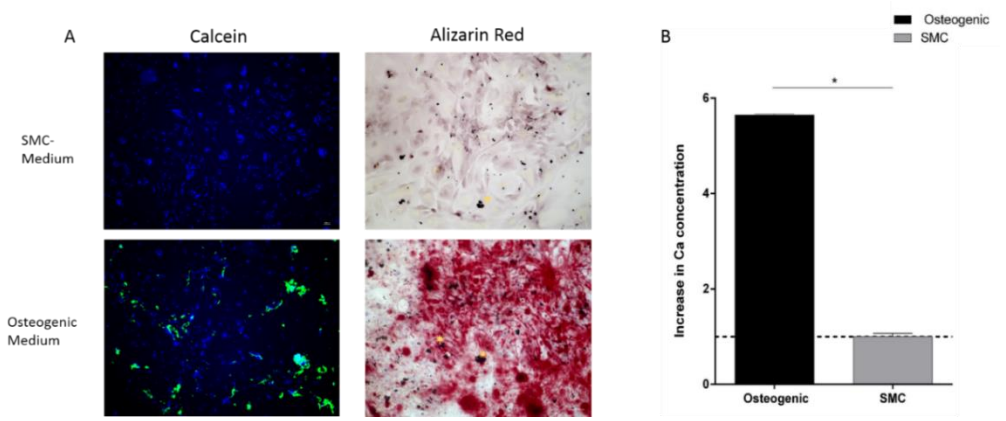

FIGURE 30: Calcein and ARS staining (A) and calcium quantification (B) after treatment with osteogenic medium
A) Calcification was shown via Calcein staining (left) and ARS staining (right). (✷ indicate precipitates from Alizarin staining solution).
B) Calcification was quantified with the help of a colorimetric Calcium assay. Control cells were maintained in SMC-medium (SMC), treated cells were kept in osteogenic medium (Osteogenic) for 30d. Calcification levels were normalized to untreated controls (n=4). Data are presented as mean +SD. ((Trillhaase et al., 2018); retracted 2020)

In order to confirm the molecular regulation of the cellular calcification, qPCR for RNA and WB analyses for protein expression of the calcification markers ALPL and CTSK was performed (Fig. 31). Both, qPCR and WB show the upregulation of calcification markers in treated cells (Osteogenic) compared to untreated controls (SMC).

ALPL expression is upregulated on RNA level up to six-fold, while *CTSK* expression shows expression fold change up to 10-fold higher in calcifying, osteogenic medium-treated cells compared to the untreated control (Fig. 31A). Additionally, upregulated expression of the calcification markers ALPL and CTSK was also confirmed in WB analyses (Fig. 31B).

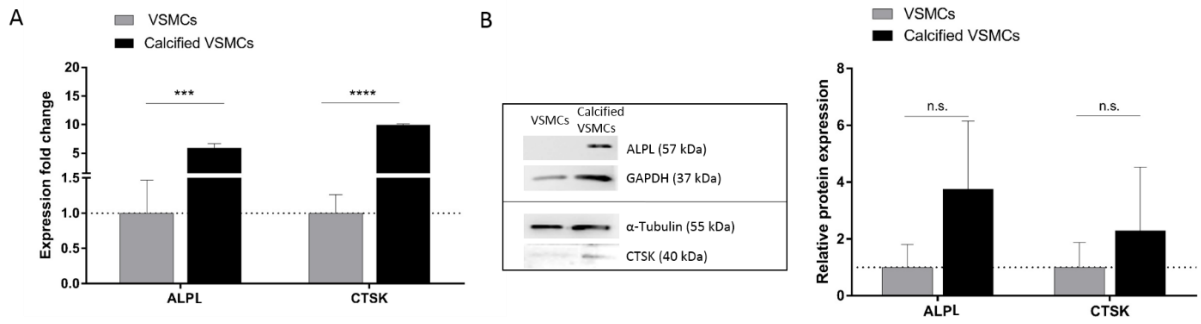

FIGURE 31: Expression analysis of calcification markers ALPL and CTSK
A) Calcifying VSMCs show significantly increased expression of calcification markers *ALPL* and *CTSK* on mRNA level.
B) Calcifying cells show increased protein expression of calcification markers ALPL and CTSK in WB analysis. Representative WB images are shown on the left, quantification of WB is shown on the right. Data are presented as bar diagrams representing mean +SD. (Adapted from Trillhaase et al., 2018; retracted 2020)

After the protocol worked successfully in the GM cell line we wanted to apply it to other cell lines. This was also part of the Master thesis of Alexandra Rangnau and the Bachelor thesis of Ann-Selin Onuk.

We used 9p21 R WT and KO cells and treated them as described above. We then performed ARS stainings in order to see the CaP deposits. Unfortunately, the ARS staining remained negative for a majority of experiments (4/5) and cell lines as seen in Fig. 32. Further, often cells detached due to the longevity of treatment and high proliferation rate.

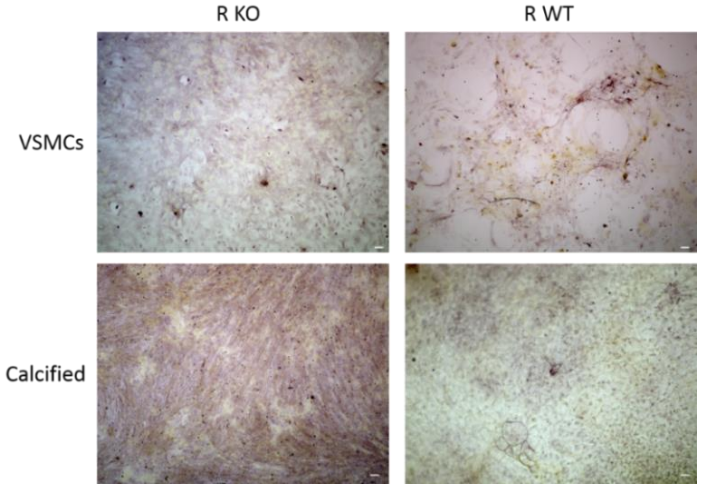

FIGURE 32: ARS staining in 9p21 R KO and R WT cells after treatment with osteogenic medium Osteogenic medium treated cells of the R KO and WT cells show no positive ARS staining (bottom) after 30d. Representative images are displayed. Scale Bars represent 100 µm.

Consequently, as no red ARS staining was detectable, no further experiments solely using osteogenic medium were performed.

3.2.3 StemXVivo™ Osteogenic Medium supplemented with TNFα

Subsequently, we tested whether the supplementation of osteogenic medium with 20 ng/mL TNFα would improve the calcification efficiency in iPSC-derived VSMCs. Therefore, cells were incubated with the osteogenic medium and supplemented with 20 ng/mL TNFα for 10d. Medium was exchanged twice a week. This protocol was also used by Ann-Selin Onuk in her Bachelor thesis.

Human iPSC-derived calcifying VSMCs of the 18i-3-6 iPSC line were analyzed regarding their amount of CaP deposits using ARS staining. As seen below ARS (Fig. 33) shows varying results in biological replicates (experiments). Only two out of five calcification approaches resulted in a positive ARS staining.

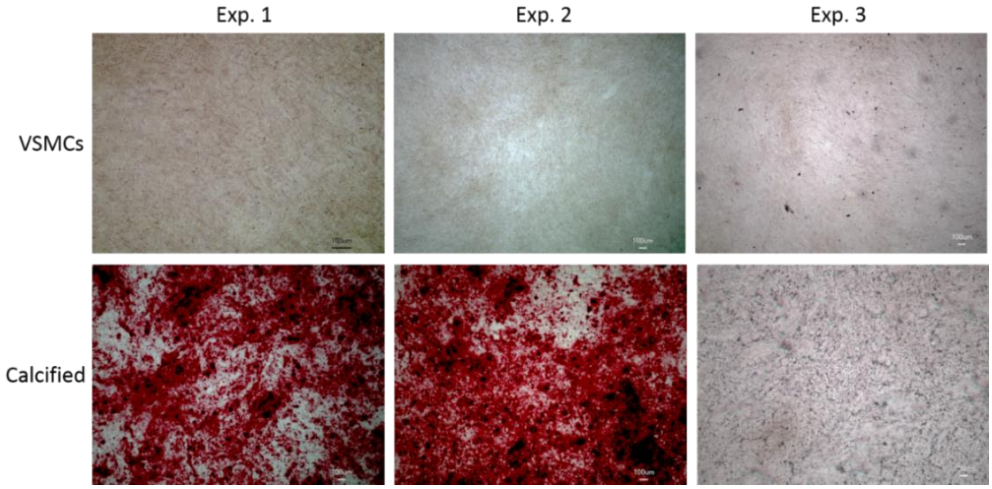

FIGURE 33: ARS staining in 18i-3-6 iPSC-derived VSMCs
VSMCs kept in maintenance medium (top) do not show calcium deposits, while calcifying VSMCs (bottom) show red stains in at least 2 out of 3 biological replicates (Exp.1-3).
Scale bars represent 100 µm.

Following, we wanted to identify possible cell-line specific effects that would be responsible for the low efficiency of the calcification protocol and therefore, applied it to R and NR iPSC-derived VSMCs. 9p21 R iPSC-derived VSMCs showed two positive ARS stainings out of six approaches overall, whereby both positive stainings originated from R KO cell lines (Fig. 34).

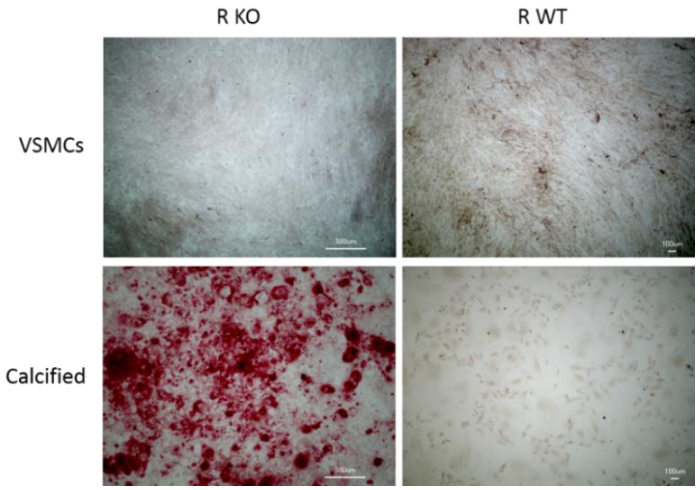

FIGURE 34: ARS staining in 9p21 R iPSC-derived VSMCs
VSMCs kept in maintenance medium (top) do not show calcium deposits, while calcifying VSMCs (bottom) show red stains in R KO iPSCs in 2 out of 3 approaches. The R WT did not show positive calcification in all 3 experiments. Scale bars represent 100µm.

9p21 NR iPSC-derived VSMCs showed an even lower efficiency. In NR KO only one out of three approaches was successful (Fig. 35). NR WT cells did not calcify in this setting (Data not shown).

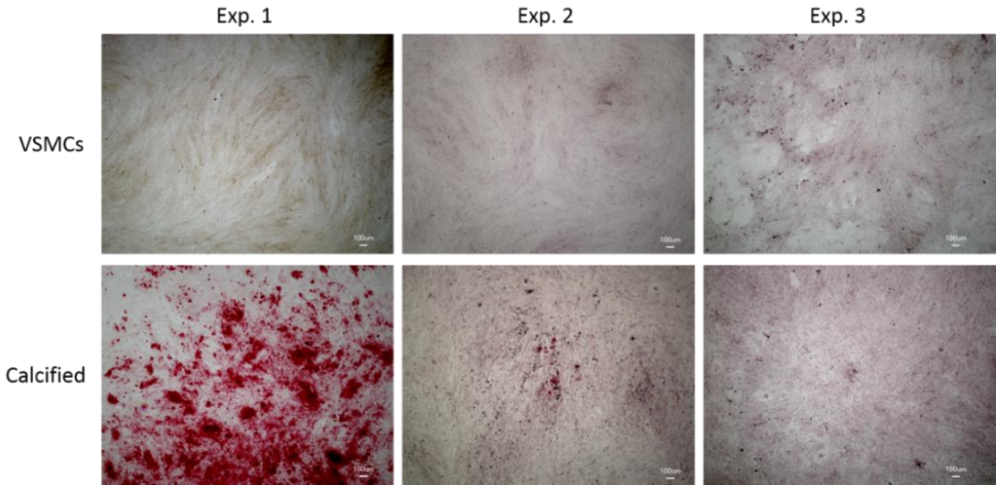

FIGURE 35: ARS staining in 9p21 NR KO iPSC-derived VSMCs
VSMCs kept in maintenance medium (top) do not show calcium deposits. Treated VSMC showed a positive ARS staining in only 1 out of 3 approaches (Exp. 1-3). Scale bars represent 100 µm.

Overall, only four out of 18 approaches using osteogenic medium in combination with TNFα resulted in a positive ARS staining. Therefore, this method did not result stably in positive staining in iPSC-derived VSMCs and was not used for further analyses. Furthermore, the low efficiency is not due to the cell line identity.

3.2.4 Combination of H_2O_2 with TNFα and BMP2

In the following experiment we aimed to investigate whether H_2O_2 was able to induce calcification in iPSC-derived VSMCs. We further looked at the effect in different culturing media, SMC medium and osteogenic medium, as well as the effect of 20 ng/mL TNFα and/or 200 ng/mL BMP2. For technical reasons we used a R WT clone to perform this assay.

Two 48 well plates were coated with 0.1% gelatin and 20,000 c/well were seeded and cultured until confluency. On d0 of calcification one plate was treated with SMC-maintenance medium including the different combinations of calcifying agents (Fig. 36). The other plate was cultured in osteogenic medium with the calcifying reagents respectively. Medium was exchanged twice a week, and samples were collected on d6.

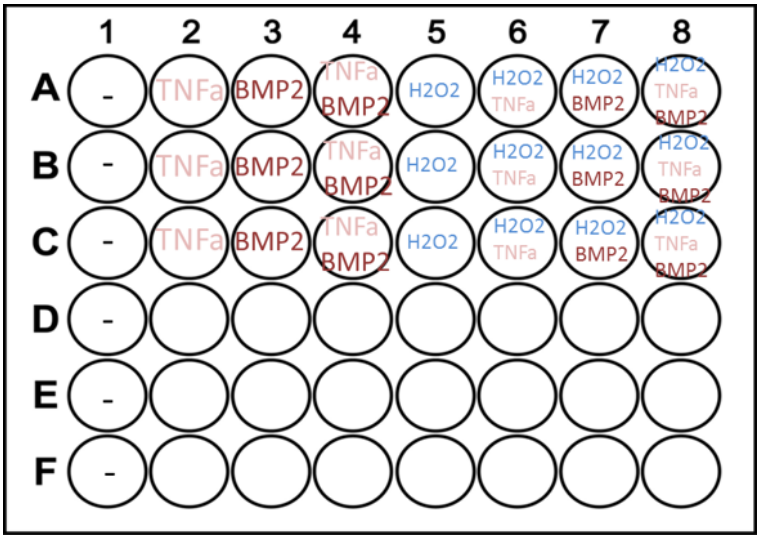

FIGURE 36: Plate layout of the calcification Test using H_2O_2
Two 48 well plates were prepared, one with SMC maintenance medium, the other containing osteogenic medium. The first row stayed untreated, the second contained 20 ng/mL TNFα, the third 200 ng/mL BMP2, the 4th TNFα and BMP2. Row 5 contained 0.4 mM H_2O_2, row 6 H_2O_2 together with TNFα, row 7 H_2O_2 together with BMP2 and the last row a combination of all three agents.

Firstly, samples were stained with ARS and Calcein to see whether CaP precipitation took place. As expected, SMC without supplementation did not show any positive stainings (Fig. 37, left). SMC maintenance medium where TNFα and/or BMP2 was added we did not see any positive stainings either (Fig. 37).

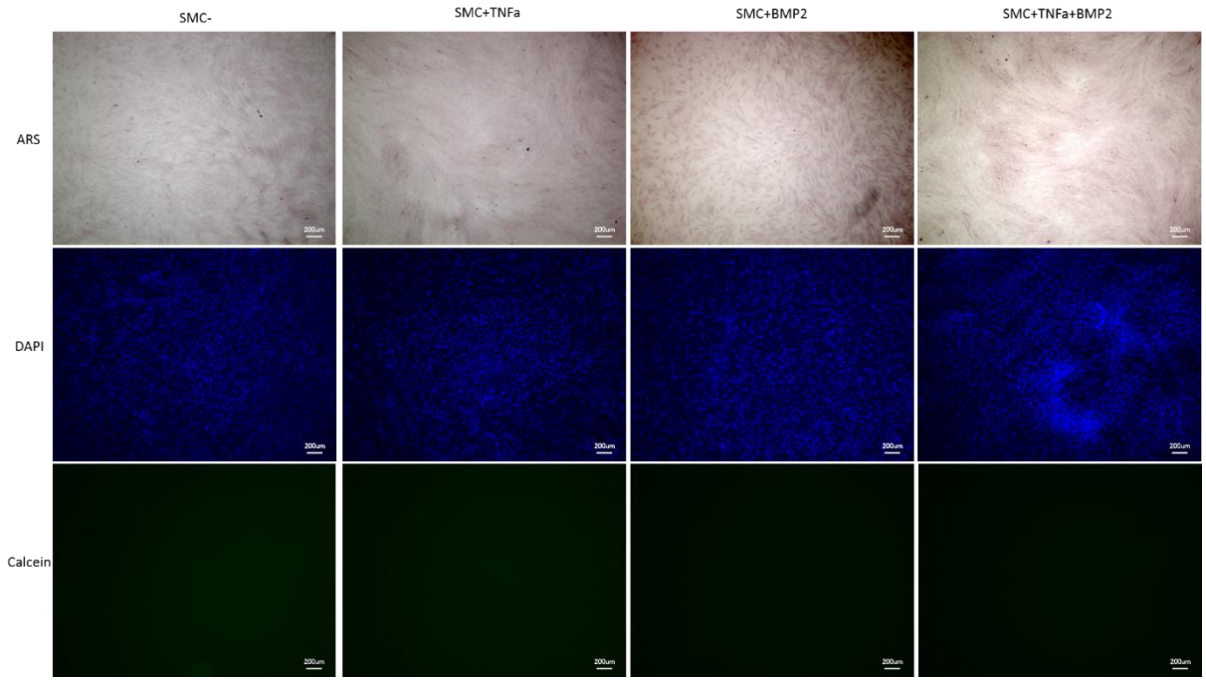

FIGURE 37: ARS and Calcein staining of cells treated with SMC medium supplemented with TNFα and/or BMP2
Cells kept in SMC medium do not show positive stainings. Neither do cells supplemented with TNFα and/or BMP2. Representative images are displayed. Scale bars represent 200 µm.

The addition of H_2O_2 to SMC maintenance medium with or without TNFα and/or BMP2 did not result in positive ARS or Calcein stainings (Fig. 38).

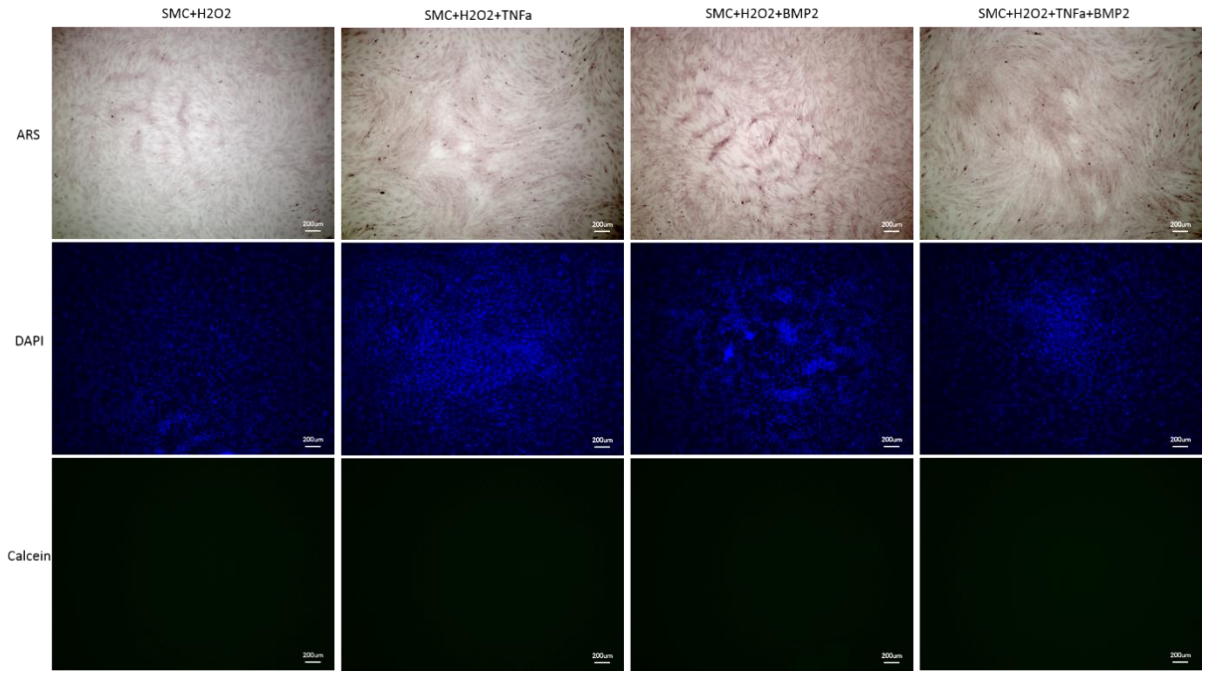

FIGURE 38: ARS and Calcein staining of cells treated with SMC medium with H_2O_2 and TNFα and/or BMP2
Cells kept in SMC medium with H_2O_2 alone do not show positive stainings. Cells supplemented with TNFα and/or BMP2 do not show positive stainings either. Representative images are displayed. Scale bars represent 200 µm.

The same applies to VSMCs kept in osteogenic medium. They do not show calcification as detectable by ARS and Calcein staining (Fig. 39, left). Neither do cells in osteogenic medium when treated with TNFα and/or BMP2 (Fig. 39).

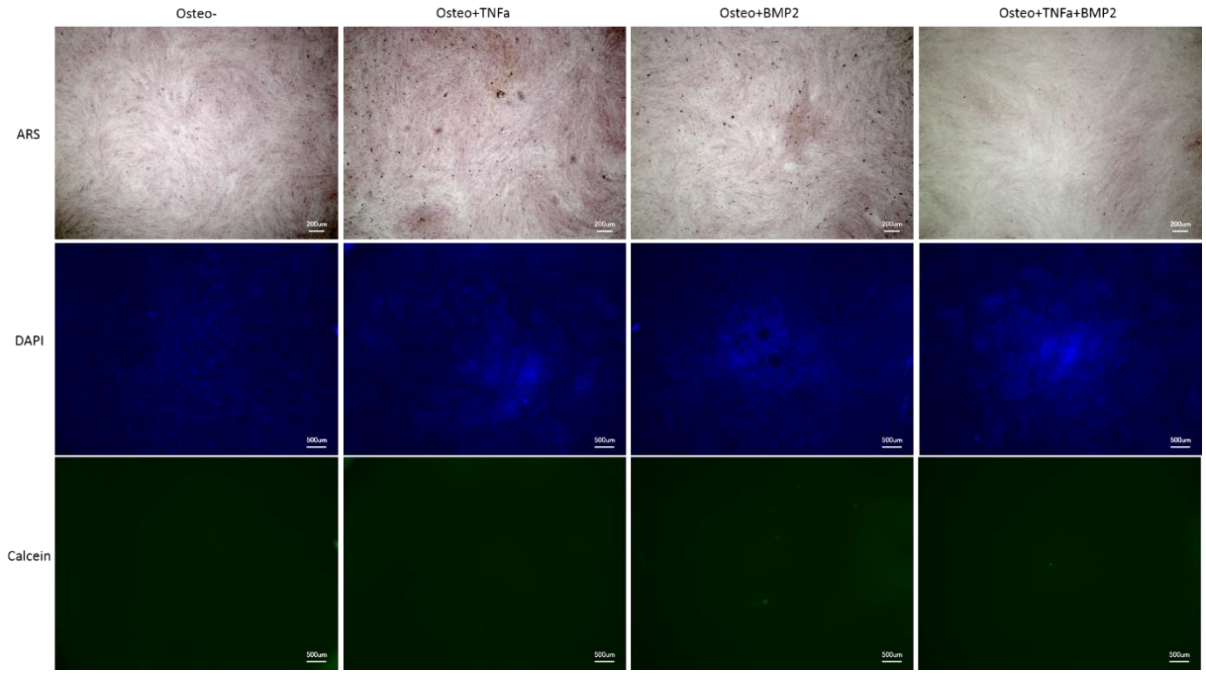

FIGURE 39: ARS and Calcein staining of cells cultured in osteogenic medium with TNFα and/or BMP2
Cells kept in osteogenic medium do not show positive stainings. Neither do cells supplemented with TNFα and/or BMP2. Representative images are displayed. Scale bars represent 200 µm.

Finally, the supplementation of osteogenic medium with H_2O_2 did not result in positive stainings (Fig. 40, left). The addition of TNF and/or BMP2 did not enhance CaP deposition (Fig. 40). Further, adding H_2O_2 decreased the cell number, as visible in the images.

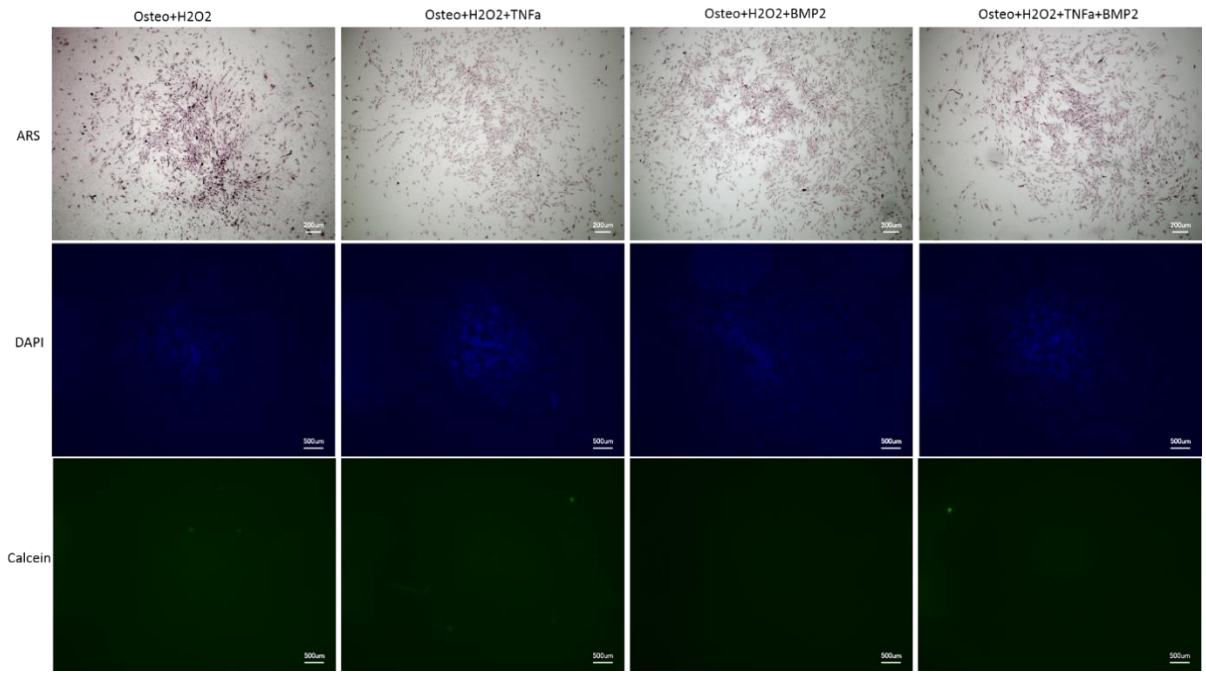

FIGURE 40: ARS and Calcein staining of cells treated with osteogenic medium with H_2O_2 and TNFα and/or BMP2
Cells kept in osteogenic medium with H_2O_2 alone do not show positive stainings. Neither do cells supplemented with TNFα and/or BMP2. Further, cell number is reduced in all approaches. Representative images are displayed. Scale bars represent 200 µm.

Afterwards, we measured the Ca concentration in all samples to identify differences in Ca concentrations. None of the approaches, neither in SMC maintenance medium (SMC) nor in osteogenic medium (Osteo) resulted in a reasonably high Ca concentration after 6d of treatment (Fig. 41). We could not prolong the time for sampling to more than 6d, as cells started detaching and got apoptotic.

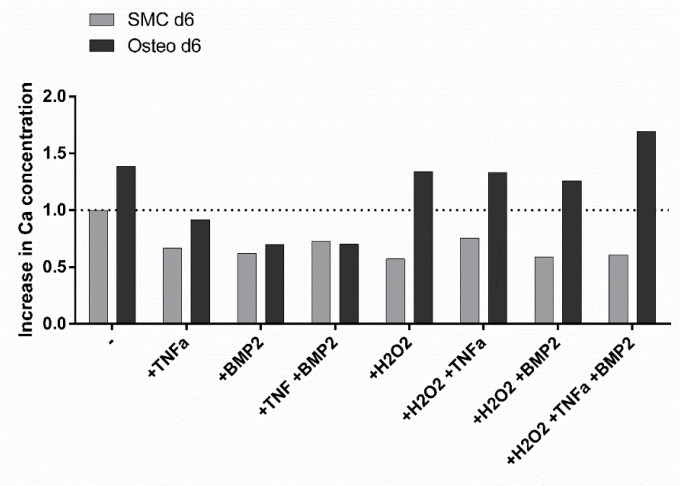

FIGURE 41: Ca Assay of calcification test with H2O2, TNFαand BMP2
None of the methods described above resulted in a significant increase in Ca concentration after 6d of treatment. n=1 replicate

As the methods investigated, failed to result in detectable ARS and Calcein staining in iPSC-derived VSMCs, we considered them inappropriate to perform any further analyses.

3.2.5 Calcification according to Alves et al., 2014

In 2014, Alves and colleagues published a calcification protocol for human mesenchymal stem cells and human VSMCs (Alves et al., 2014). We used this protocol in order to establish a calcification protocol for human iPSC-derived VSMCs in a R WT clone.

VSMCs were cultured in SMC maintenance medium. For induction of calcification cells were cultured in SMC medium or osteogenic medium including 1.8 mM Calcium chloride ($CaCl_2$) and 20 mM HEPES. Freshly, the medium was supplemented with 0.1 mM L-AP, 10 mM β-GP and 100 nM dexamethasone. Medium was exchanged twice a week. Calcification was stopped after 9d, ARS and Calcein staining were performed. The protocol published by Alves et al. in 2014 did not result in positive ARS and Calcein stainings (Fig. 42).

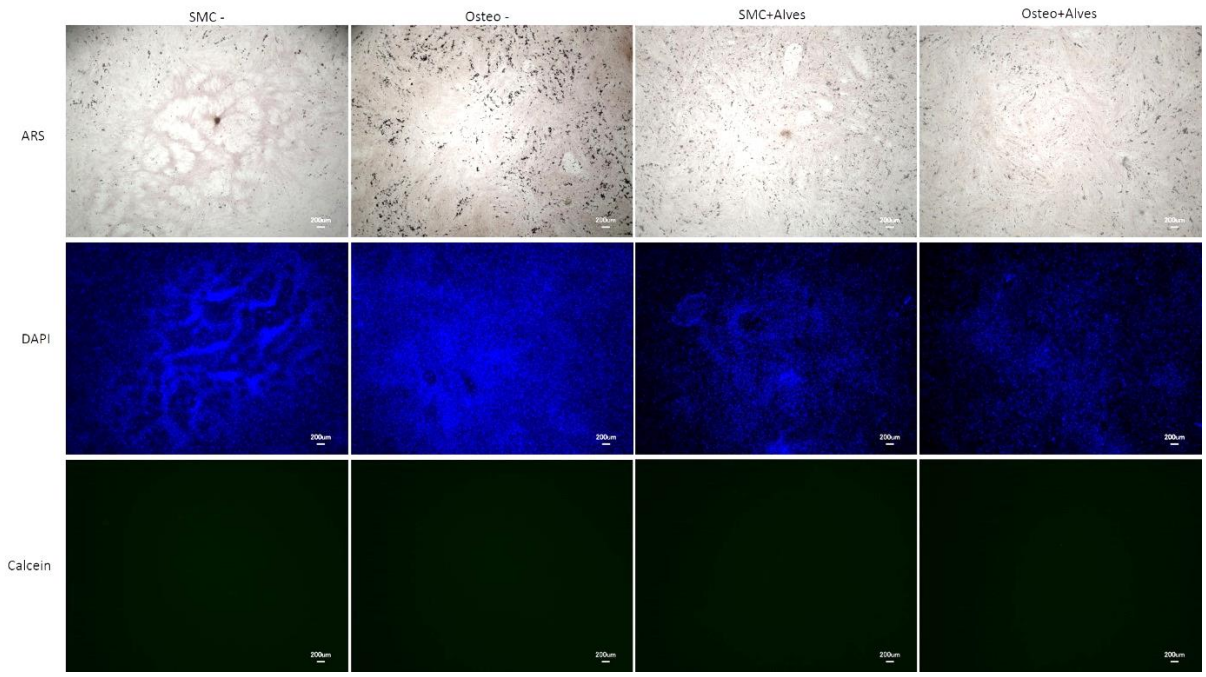

FIGURE 42: ARS and Calcein staining of cells induced with the cocktail published by Alves et al., 2014 in a R WT clone
Cells kept in SMC and osteogenic medium do not show positive ARS or Calcein stainings. Neither do cells treated with the Alves cocktail in SMC or osteogenic medium. Representative images are displayed. Scale bars represent 200 µm.

As the ARS and Calcein staining remained negative for both media, this method was not used for further experiments.

3.2.6 Tziakas cocktail for calcification

In 2019 Tziakas et al. published a calcification protocol for human smooth muscle cells slightly different from the one published by Alves et al., mentioned above (Tziakas et al., 2019). Briefly, cells were cultured in SMC medium supplemented with 4 mM $CaCl_2$, 5 mM β-GP, 50 µg/ml L-AP, 1 µM insulin and 0.1 µM dexamethasone for 7d. We tested this calcification cocktail in two independent iPSC-VSMC lines in two biological replicates each.
The first cell line we tested, 18i-3-6, showed positive stainings for ARS and Calcein after 7d of incubation (Fig. 43).

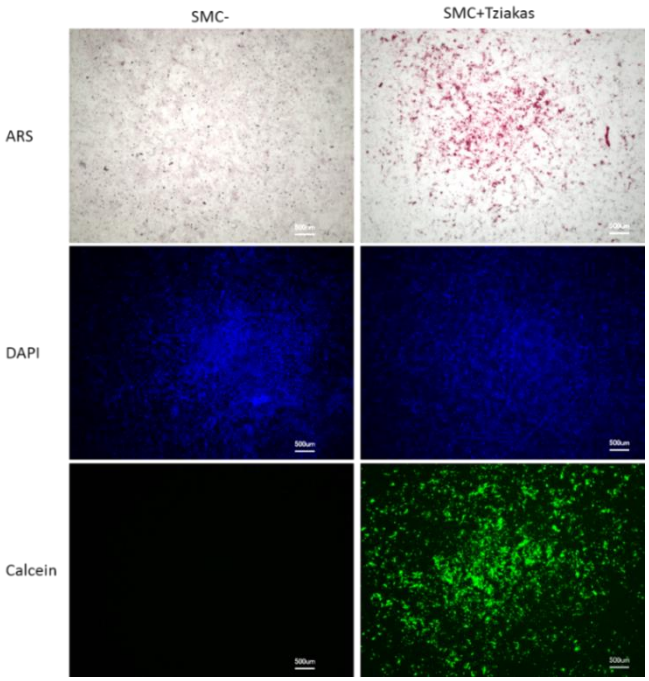

FIGURE 43: ARS and Calcein staining of 18i-3-6 VSMCs induced with the cocktail published by Tziakas et al., 2019
Cells kept in SMC maintenance medium do not show positive ARS or Calcein stainings. Human iPSC-derived VSMCs treated with the Tziakas cocktail in SMC Medium show positive stainings in ARS and Calcein. Representative images are displayed. Scale bars represent 500 µm.

For the independent, healthy control cell line 18i-3-6, the calcification cocktail published by Tziakas and colleagues resulted in positive ARS and Calcein staining. In order to assure, that the protocol would also work in other cell lines we additionally applied it to a 9p21 R WT cell line under the same conditions.

This cell line as well showed positive ARS and Calcein staining after treatment with the Tziakas cocktail for 7d (Fig. 44).

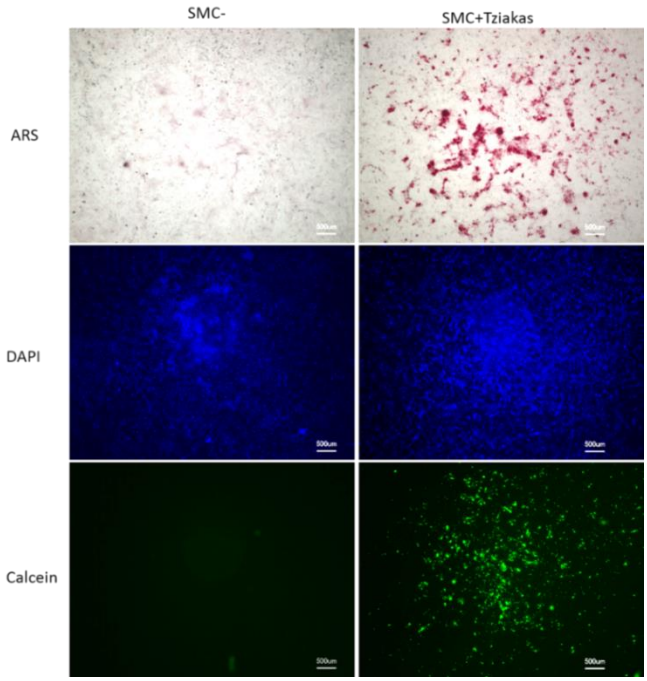

FIGURE 44: ARS and Calcein staining of 9p21 R WT cells induced with the cocktail published by Tziakas et al., 2019
Cells kept in SMC maintenance medium do not show positive ARS or Calcein stainings. Human iPSC-derived VSMCs treated with the Tziakas cocktail in SMC Medium show positive stainings in ARS and Calcein. Representative images are displayed. Scale bars represent 500 µm.

As this calcification cocktail resulted in positive ARS and Calcein staining in two independent cell lines we used it for further experiments. The following results were all obtained using the calcification cocktail published by Tziakas and colleagues. Cell numbers seeded for calcification approaches ranged between 30,000 cells/well for R cells up to 100,000 cells/well for NR cells. A 24 well format was chosen and induction of calcification was terminated after 7d. Cells were then used for further analyses, ARS and Calcein staining, Calcein quantification, qPCR and WB analyses (for details see Methods section). The Randox Ca Assay was not applied for the following experiments due to technical reasons. During the course of the experiment we noticed that 18i-3-6 cells more often showed negative ARS and Calcein stainings (Fig. 45). Only two out of eight calcifications resulted in positive ARS and Calcein staining.

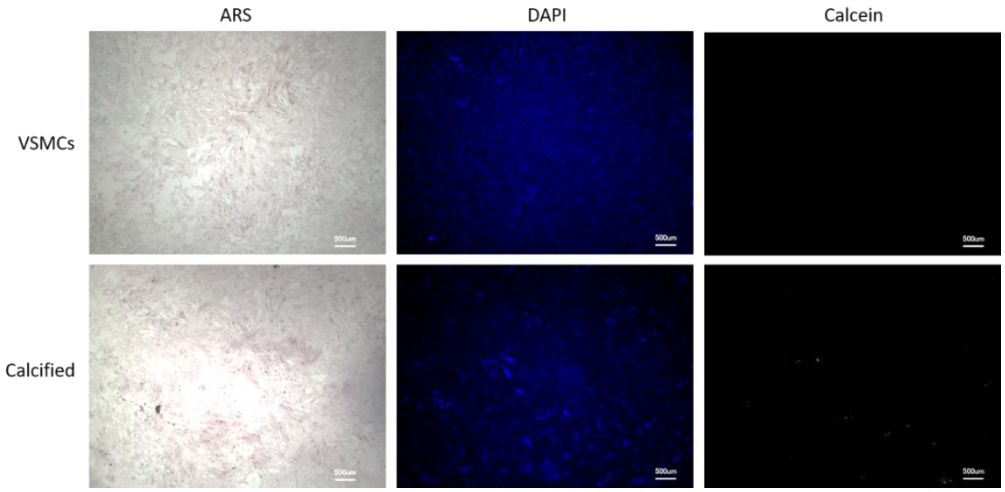

FIGURE 45: Representative ARS and Calcein staining of 18i-3-6 VSMCs treated with calcifying agents from Tziakas for n=3 replicates
Cells kept in SMC maintenance medium do not show positive ARS or Calcein stainings. Human iPSC-derived VSMCs treated with the Tziakas cocktail in SMC Medium do not show positive ARS and Calcein stainings either. Representative images are displayed. Scale bars represent 500 µm.

In order to quantify the CaP deposits, the Calcein stainings were analyzed, comparing the green Calcein staining to DAPI between the untreated and the treated, calcifying cells (Fig. 46). For 18i-3-6 we noticed very few Calcein staining in calcifying VSMCs compared to untreated VSMCs (Fig. 46).

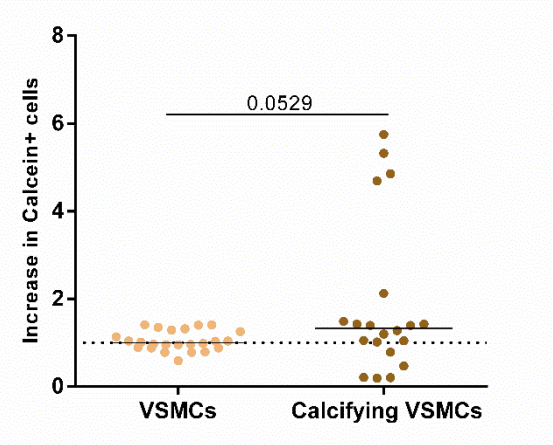

FIGURE 46: Calcium quantification using the Calcein staining in 18i-3-6 cells
18i-3-6 cells did not display a significant increase in CaP depositions in calcifying cells compared to untreated VSMCs. Dots represent value per image analyzed.

For the determination of gene expression, we applied a RT^2 Profiler PCR Array (Qiagen) for osteogenesis to samples from the initial protocol testing, showed the

upregulation of important calcification markers in 18i-3-6 cells, like *CSF1*, *RUNX2*, *CTSK*, and *DLX5* (Fig. 47), while *ALPL* was downregulated (not shown).

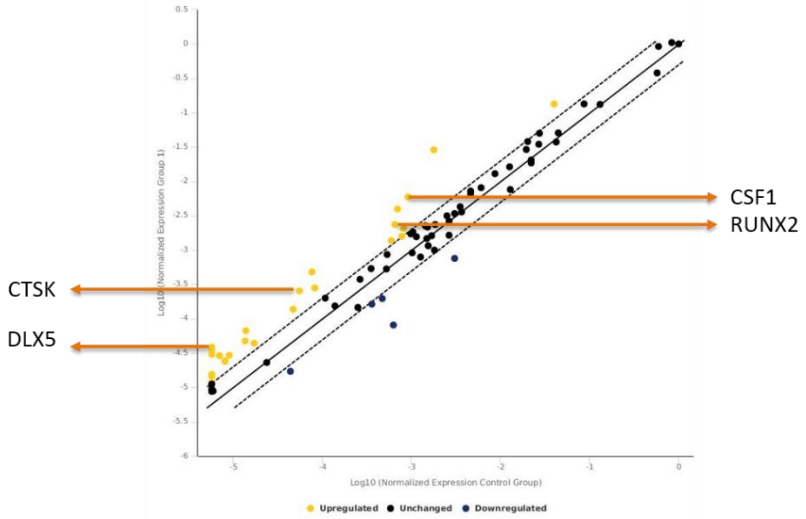

FIGURE 47: Gene expression profile of iPSC-derived calcifying 18i-3-6 cells
RT profiler Array for osteogenesis shows the upregulation of various genes (yellow), including calcification markers *CSF1*, *RUNX2*, *CTSK*, and *DLX5*. Treated vs untreated iPSC-derived VSMCs, β-Actin served as housekeeping gene.

The results served as a basis for further qPCR and WB analyses. We additionally checked for *ALPL* and *OPN* expression on RNA level.

Merging all replicates, 18i-3-6 cells showed upregulated expression in the calcification-associated markers *CTSK* and *CSF1*, *ALPL* however was not significantly changed in its expression (Fig. 48A). *RUNX2* as late stage calcification marker was upregulated in its expression, while *OPN/SSP* did not show a significant difference in the expression on RNA level in calcifying VSMCs compared to untreated VSMCs (Fig. 48B).

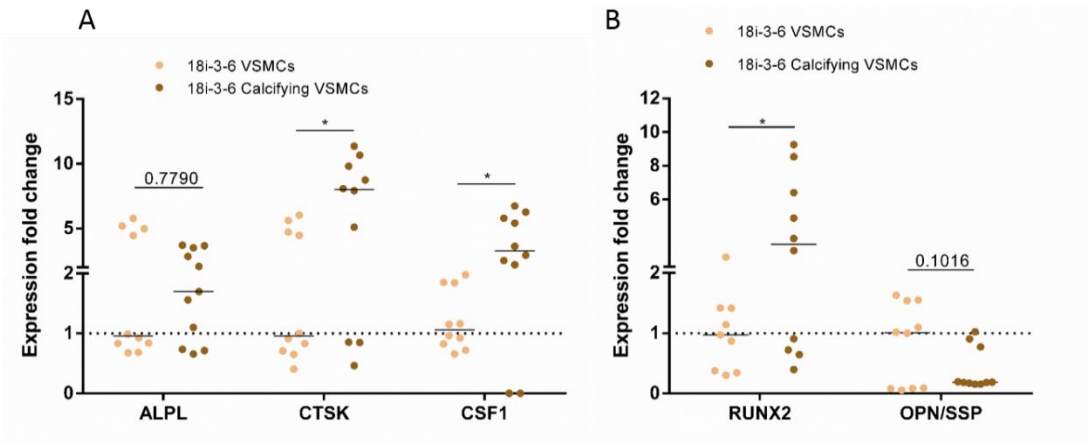

FIGURE 48: Expression of calcification-associated markers in 18i-3-6 iPSC-derived cells
A) *CTSK* and *CSF1*, as early and intermediate calcification markers were significantly upregulated, *ALPL* was not significantly changed.
B) *RUNX2* as late stage calcification marker was significantly upregulated, while *OPN/SSP* was not significantly changed. Dots represent median per technical replicate.

Concluding, three out of five calcification associated markers were significantly upregulated in their expression on RNA level in 18i-3-6 iPSC-derived calcifying cells.

3.3 Differentiation of 9p21 NR WT and R WT iPSC towards VSMCs and their calcification

After the differentiation protocol of healthy WT iPSCs into VSMCs was adapted and proved efficient, the effect 9p21 may have on the differentiation needed to be estimated. A NR cell line (HE463_7), was treated with TALENs creating a 58 kb KO in the 9p21 CAD risk region, resulting in two WT (E14 and E17), and two KO (E50 and E56) clones. The R cell line (C512) was treated in the same way, resulting in three WT (TAL1-2, TAL1-5, and TAL2-3), and two KO (TAL1-9 and WB46) clones. For further information on the cell lines please see Material & Methods section. In order to identify the effect, the CAD risk region has on calcification, NR and R WT cell lines were compared.

3.3.1 Characterization of 9p21 NR WT and R WT iPSCs

Morphologically, the NR WT and R WT iPSCs could be described as round shaped colonies with defined colony boundaries in phase contrast (PhC) images. Further, the cells were comparably small with a large nucleus and rather low amounts of cytoplasm. Human iPSCs of the NR WT and R WT cell lines were further stained for NANOG in IF staining demonstrating the proteins localization in the nuclei. No differences could be seen between the NR WT and R WT cells regarding their morphology or the expression of NANOG in IF staining (Fig. 49).

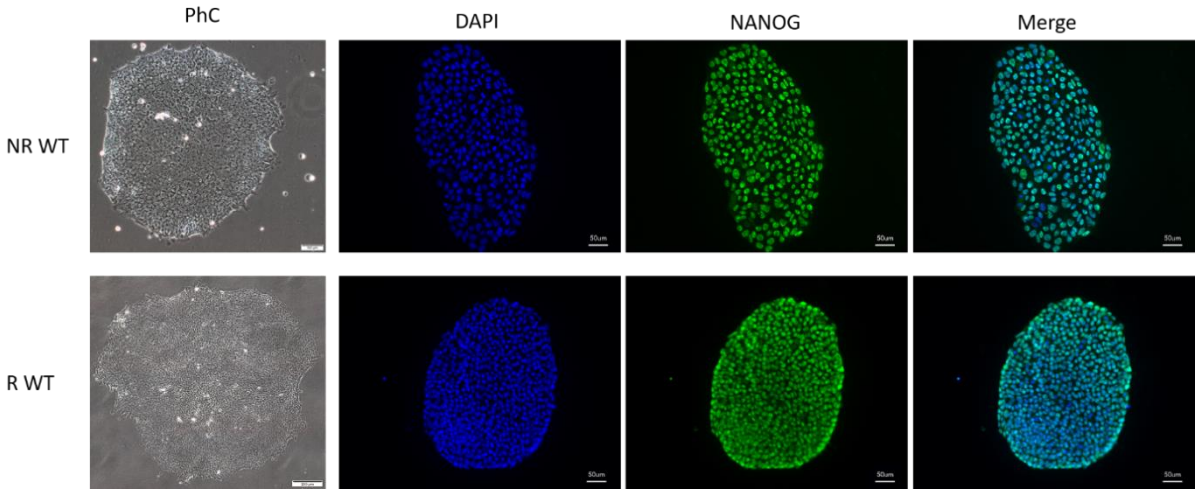

FIGURE 49: IF staining of 9p21 NR WT and R WT iPSC colonies
NR WT (top) and R WT (bottom) iPSCs display comparable, typical iPSC morphology in bright field. Further, both express NANOG (green) in the nuclei of the iPSCs; Nuclei are counterstained with DAPI (blue). Scale bars represent 200 µm for PhC and 50 µm for IF staining images.

On morphological and cellular level, we did not see differences between the R WT and NR WT iPSCs.

3.3.2 Differentiation of 9p21 NR WT and R WT iPSCs towards VSMCs

Following the differentiation protocol described above, R WT and NR WT iPSC-lines were differentiated into VSMCs. Resulting VSMCs were characterized regarding their expression status of pluripotency-associated markers as well as SMC-specific markers on RNA and protein level. First, IF staining were performed that showed the expression

of CNN1 and TAGLN on protein level and their correct localizations in the contractile fibers and the cytoplasm of the cells (Fig. 50).

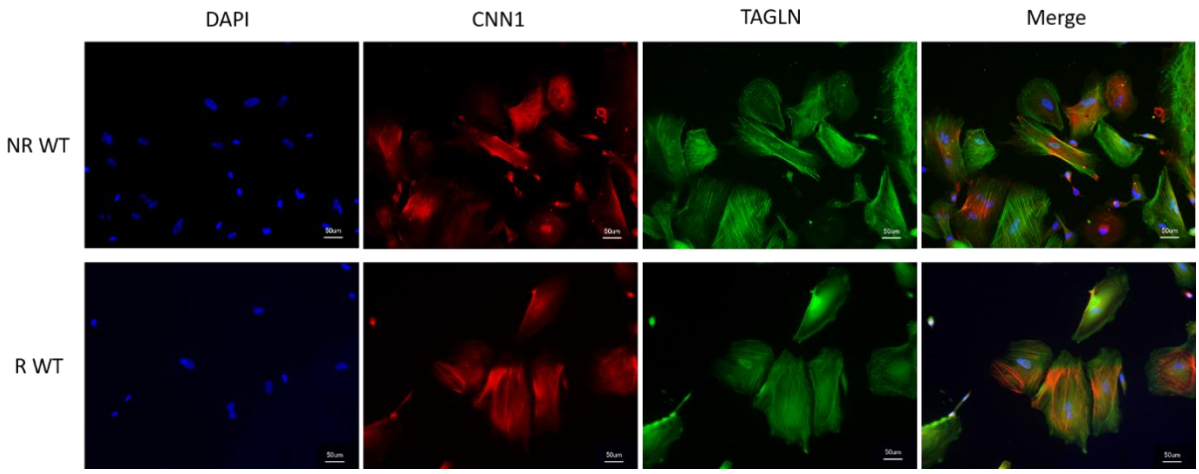

FIGURE 50: IF staining of 9p21 NR WT and R WT iPSC-derived VSMCs
NR WT (top) and R WT (bottom) VSMCs express TAGLN (green) and CNN1 (red) in the contractile apparatus and the cytoplasm of the VSMCs; Nuclei are counterstained with DAPI (blue). Scale bars represent 50 µm.

For the R WT and NR WT cells we further estimated the differentiation efficiency via the IF staining of CNN1 and TAGLN in iPSC-derived VSMCs. The majority of the R WT as well as the NR WT iPSC-derived VSMCs displayed an overall CNN1 and TAGLN overlap and, therefore a differentiation efficiency, of more than 95% (Fig. 51). The differentiation efficiency between NR WT and R WT cells was not significantly different.

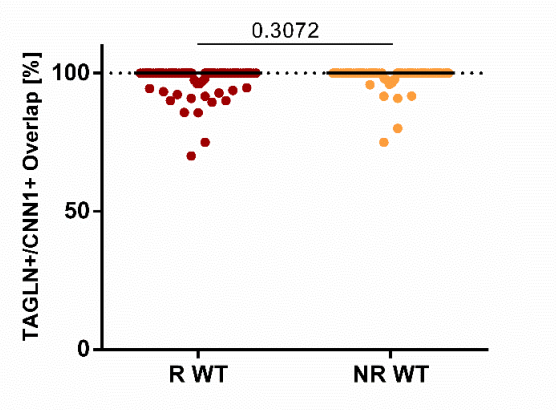

FIGURE 51: Differentiation efficiency of R WT vs NR WT cells
NR (orange) WT and R WT (red) VSMCs express TAGLN and CNN1 with an overlap of above 95%. Differentiation efficiencies of NR WT and R WT did not differ significantly between WT cells of both genotypes. Dots represent % positive cells per image analyzed.

Following, we performed molecular analyses of the R WT and NR WT iPSCs and iPSC-derived VSMCs in order to confirm the correct molecular regulation during the differentiation process. Firstly, we performed RNA expression analyses of all clones showing the downregulation of pluripotency-associated markers in all R WT clones (Fig. 52) as well as NR WT clones (Fig.53).

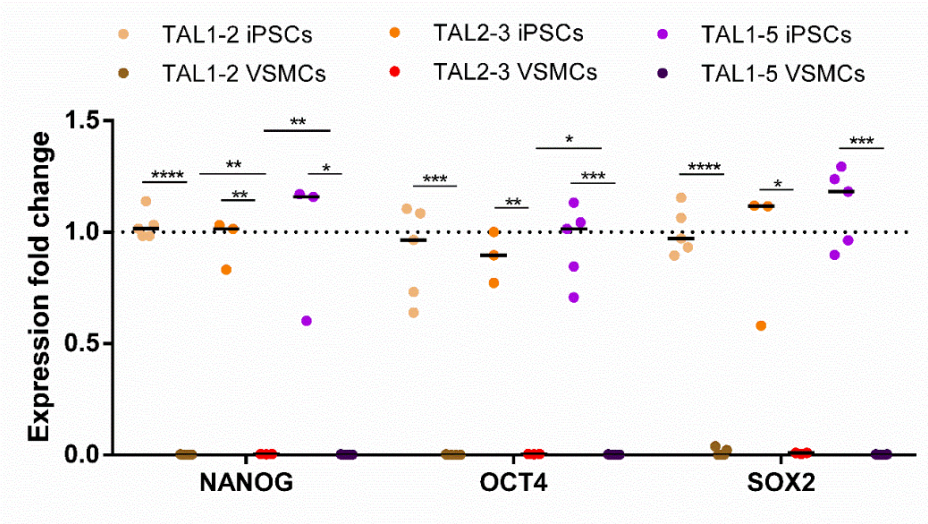

FIGURE 52: RNA expression analysis of R WT clones for pluripotency-markers
RNA expression analyses show significant downregulation of the pluripotency markers *NANOG, OCT4,* and *SOX2* in iPSC-derived VSMCs compared to iPSCs of all three R WT clones. N.s. t-test not indicated in the Figure. Each dot represents median of technical replicates.

All R WT clones showed a significant downregulation of pluripotency-associated marker expression in iPSC-derived VSMCs compared to iPSCs (Fig. 52). Although, statistically significant differences between the clones could be detected, the three R WT clones were merged for the analysis of RNA expression.

The same applied to the NR WT clones. RNA expression of pluripotency-associated markers was significantly downregulated in iPSC-derived VSMCs compared to iPSCs (Fig. 53). Even though significant differences between the clones were detected e.g. in *OCT4* and *SOX2* expression, data of both clones were merged for genotype-dependent analysis (Fig. 54).

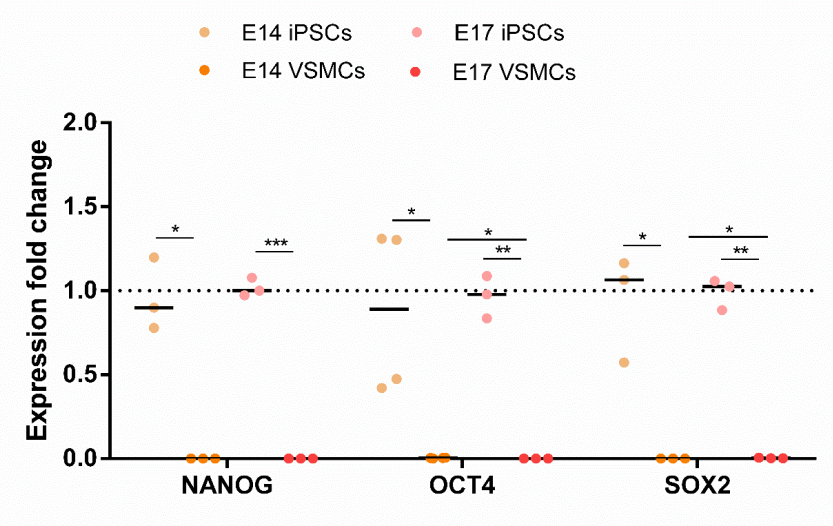

FIGURE 53: RNA expression analysis of NR WT clones for pluripotency-markers
RNA expression analyses showed significant downregulation of the pluripotency markers *NANOG, OCT4,* and *SOX2* in iPSC-derived VSMCs compared to iPSCs of both NR WT clones. N.s. t-test not indicated in the Figure. Each dot represents median of technical replicates.

Therefore, in order to detect differences due to the genotype, we merged the cells of the same genotype for RNA expression analyses. Except for *NANOG*, there were no significant differences in the RNA expression of pluripotency-associated markers between R WT and NR WT iPSCs or iPSC-derived VSMCs (Fig. 54).

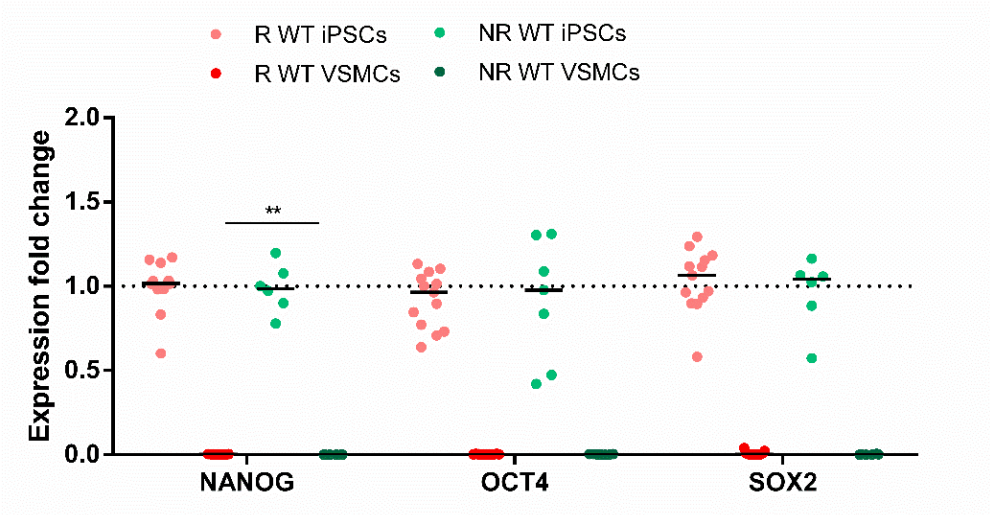

FIGURE 54: RNA expression analysis of NR WT vs R WT cells for pluripotency-markers
RNA expression of the pluripotency markers *NANOG, OCT4,* and *SOX2* in iPSC-derived VSMCs compared to iPSCs showed no significant differences. Only *NANOG* showed a difference in RNA expression in iPSC-derived VSMCs between R WT and NR WT. N.s. t-test not indicated in the Figure. Each dot represents median of technical replicates.

The detected statistically significant differences in the RNA expression of *NANOG* in iPSC-derived VSMCs of R WT and NR WT cells however was considered biologically irrelevant, as the differences in expression fold changes are minor.

Further, we investigated the RNA expression of SMC-specific markers in iPSCs and iPSC-derived VSMCs in R WT and NR WT cells. Again, we performed RNA expression analyses for all clones of the R WT (Fig. 55) and NR WT cells (Fig. 56) to ensure correct molecular regulation in the single clones during the differentiation process.
The three R WT clones showed a significant upregulation between 4- and 15-fold of the SMC-associated markers *TAGLN*, *CNN1*, and *CALD1* in iPSC-derived VSMCs compared to iPSCs (Fig. 55).

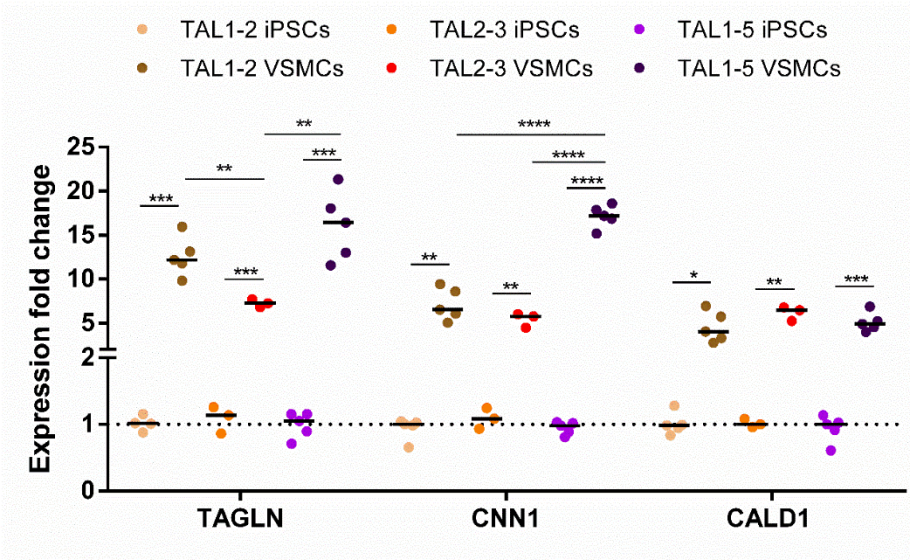

FIGURE 55: RNA expression analysis of R WT clones for SMC-markers
RNA expression analyses showed significant upregulation of the SMC-specific markers *TAGLN*, *CNN1*, and *CALD1* in iPSC-derived VSMCs compared to iPSCs of all three R WT clones. Significant differences between the clones was detected for *TAGLN* and *CNN1* expression. N.s. t-test not indicated in the Figure. Each dot represents median of technical replicates.

Again, statistical differences between the three clones were detected for *TAGLN* and *CNN1* expression.

The same results could be observed for the NR WT clones E14 and E17 (Fig. 56). Both clones showed a significant upregulation between 5- and 15-fold of SMC-specific marker expression in iPSC-derived VSMCs compared to iPSCs, except for *CALD1* that did not show a significant difference in the clone E14 (brown).

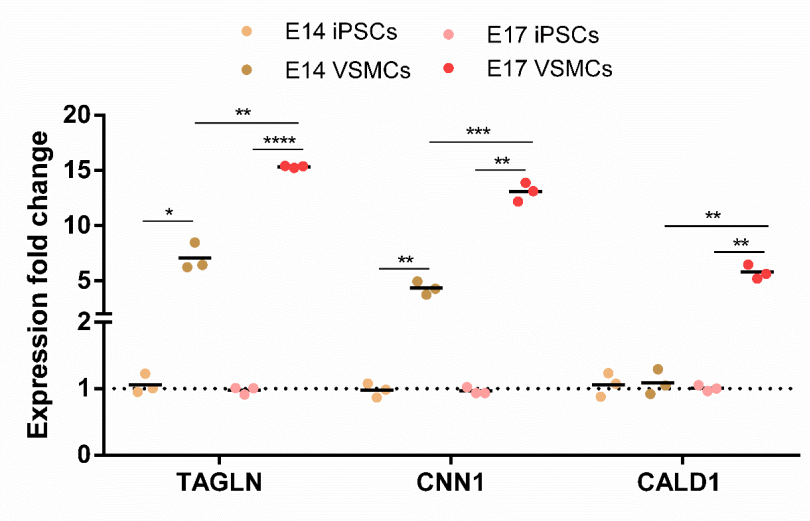

FIGURE 56: RNA expression analysis of NR WT clones for SMC-markers
RNA expression analyses showed significant downregulation of the SMC-markers *TAGLN, CNN1,* and *CALD1* in iPSC-derived VSMCs compared to iPSCs of both NR WT clones. Only *CALD1* did not show a significant upregulation in the clone E14 (brown). N.s. t-test not indicated in the Figure. Each dot represents median of technical replicates.

Even though significant differences between the clones were detected, we merged the data of the clones with the same genotype in order to examine possible differences between the genotypes. We were not able to detect significant differences in the expression of SMC-specific markers between the NR WT (green) and the R WT (red) (Fig. 57).

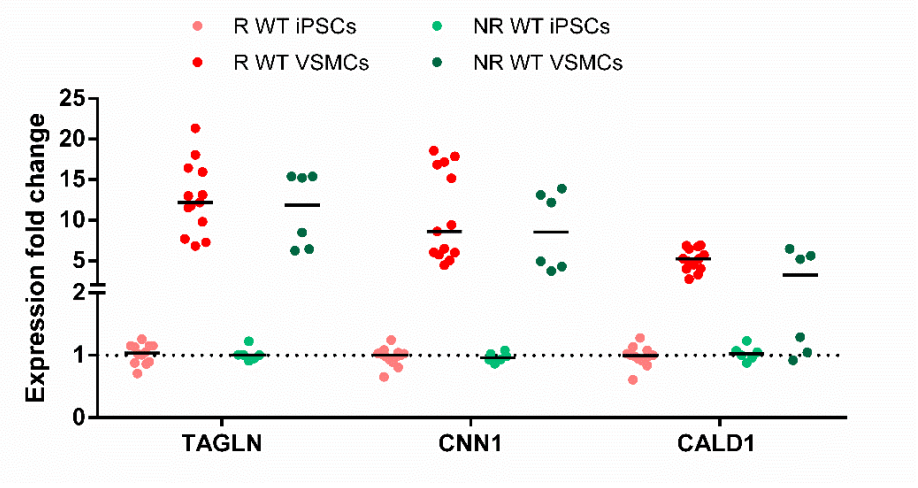

FIGURE 57: RNA expression analysis of NR WT vs R WT cells of SMC-markers
RNA expression of the pluripotency markers *TAGLN, CNN1,* and *CALD1* in iPSC-derived VSMCs compared to iPSCs showed no significant differences between R WT and NR WT cells.
N.s. t-test not indicated in the Figure. Each dot represents median of technical replicates.

Finally, we performed WB analyses to confirm the findings from RNA level on protein level. R WT cells showed a clear downregulation in protein expression of OCT4 to almost zero in iPSC-derived VSMCs (Fig. 58A/B). TAGLN expression was not significantly changed, but a slight tendency towards increased protein expression was detectable in iPSC-derived VSMCs (Fig. 58A/C).

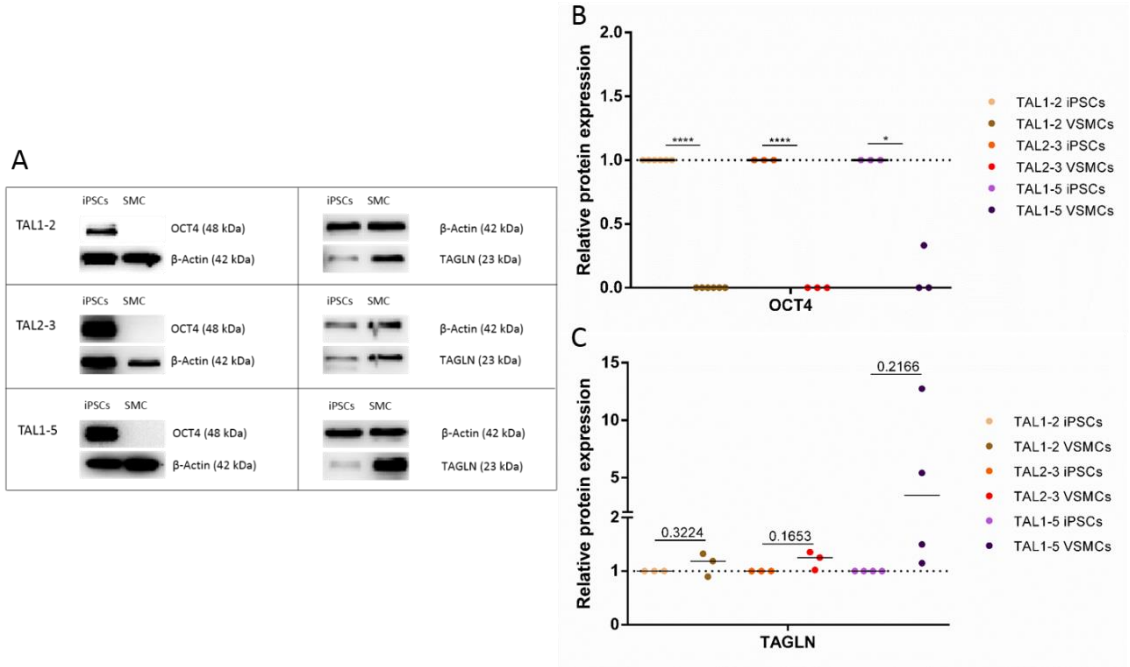

FIGURE 58: Protein expression of R WT iPSCs and iPSC-derived VSMCs.
A) Representative images of blots are displayed for each clone.
B) OCT4 protein expression was significantly downregulated in iPSC-derived VSMCs of all three clones.
C) TAGLN protein expression was not significantly changed, but a tendency towards increased expression was detectable in all three clones. Each dot represents value for each blot analyzed.

On protein level NR WT cells showed a significant downregulation in the expression of OCT4 to almost zero in iPSC-derived VSMCs (Fig. 59A/B). There were no significant differences visible between the NR WT clones. For TAGLN the clone E17 (red) showed a significant increase in the protein expression to around 15-fold in VSMCs compared to iPSCs (Fig. 59A/B). Cells of the clone E14 (orange) did not show a significant difference, but a very strong tendency towards upregulation to around 10-fold in protein expression of TAGLN was visible (Fig. 59A/B). Again, no significant differences in the TAGLN expression in iPSC-derived VSMCs between both clones was detected (Fig. 59B).

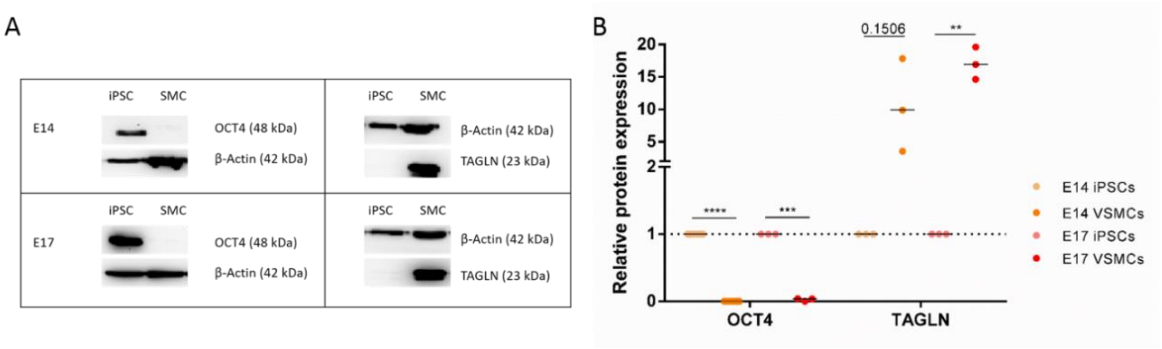

FIGURE 59: Protein expression of NR WT iPSCs and iPSC-derived VSMCs.
A) Representative images of blots are displayed for each clone.
B) OCT4 protein expression was significantly downregulated in iPSC-derived VSMCs. TAGLN expression was significantly upregulated in the clone E17 (orange); Clone E14 (red) showed a strong tendency towards upregulation in TAGLN expression in iPSC-derived VSMCs too. Each dot represents value for each blot analyzed.

On molecular level we did not see any significant differences between R WT and NR WT cells in the expression of iPSC- or SMC-marker genes and proteins. Protein expression of TAGLN in iPSC-derived VSMCs was often not significantly increased, however a tendency towards upregulation in protein expression of the respective protein was visible.

For the analysis of the VSMC behavior, we performed migration assays for iPSC-derived VSMCs of independent differentiation approaches in forms of a scratch assay. At first, we compared the migration assays of the R WT clones, to detect possible differences in migration rate in between the single clones (Fig. 60). The migration rate between the clones TAL1-2 and TAL2-3 was not significantly different (34.12% vs 35.14%). However, the clones TAL1-5 and TAL2-3 displayed significant differences in the migration rate (35.14% vs 26.02%).

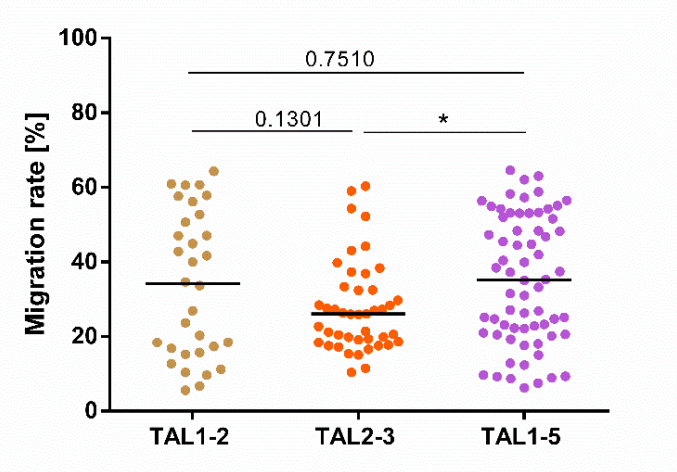

FIGURE 60: Migration rate of the R WT clones
The migration assay of the R WT clones TAL1-2 and TAL1-5 did not show significant differences in migration rate (34.12% vs 35.14%). However, between TAL1-5 and TAL2-3 we detected a significant difference in migration rate (35.14% vs 26.02%). Each dot represents migration rate per well analyzed.

Following, we analyzed the migration rate of the NR clones E14 and E17. Here we observed a significant difference in the migration rate of both NR WT clones (15.9% vs 24.68% respectively) (Fig. 61).

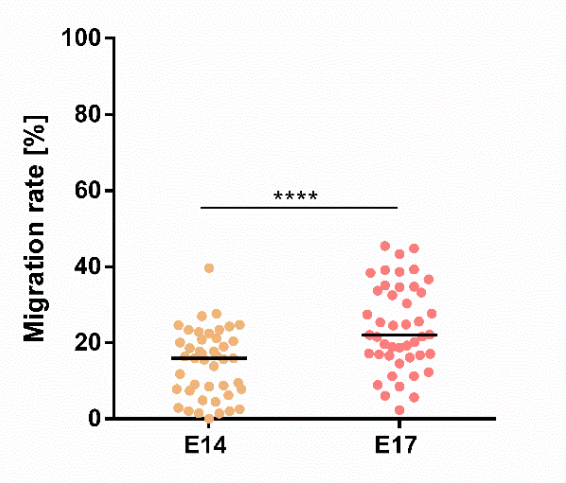

FIGURE 61: Migration rate of the NR WT clones
The migration assay of the NR WT clones E14 and E17 displayed a significant difference (15.9% vs 24.68%). Each dot represents migration rate per well analyzed.

In order to compare R WT and NR WT migration rates, we merged the data per genotype (Fig. 62). The migration rate in R WT iPSC-derived VSMCs was significantly higher (Median 27.39%) than in NR WT iPSC-derived VSMCs (Median 18.77%).

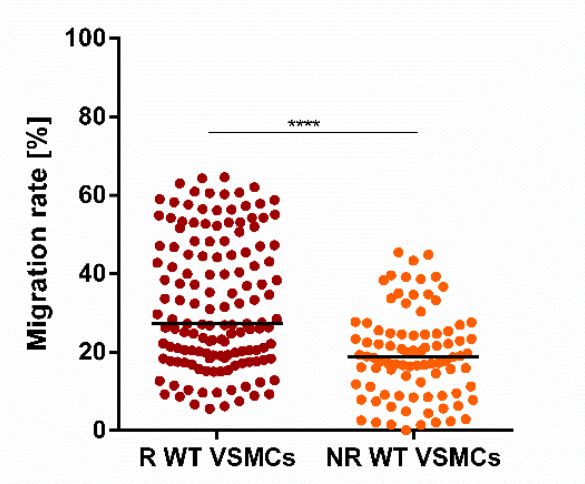

FIGURE 62: Comparison of Migration rates between R WT and NR WT VSMCs
The migration rate of R WT was significantly higher than the migration rate in NR WT VSMCs (Median 27.39% vs 18.77% respectively). Each dot represents migration rate per well analyzed.

Another characterization of VSMC behavior was determined by proliferation rate via Ki67 staining. Ki67 positive cells were counted and the percentage of Ki67+ cells was related to the overall cell number, determined by DAPI staining. Firstly, R WT clones were compared regarding their proliferation rate. The clone TAL1-2 showed a significantly lower proliferation rate (Median 0%) than the other two R WT clones (Median: TAL1-5 14.29%; TAL2-3 16.95%) (Fig. 63).

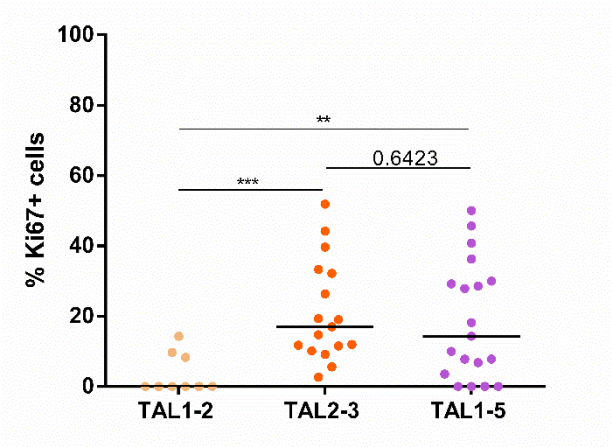

FIGURE 63: Proliferation rate in R WT iPSC-derived VSMCs
The proliferation rate in TAL1-2 cells was significantly lower (0%) than in the other two clones (16.95% vs 14.29% respectively). Each dot represents % positive cells per well analyzed.

NR WT clones of iPSC-derived VSMCs show significantly different proliferation rates as well (Fig. 64). The clone E17 (dark green) showed almost no proliferation (Median: 0%), while E14 (light green) showed a proliferation rate of around 11%.

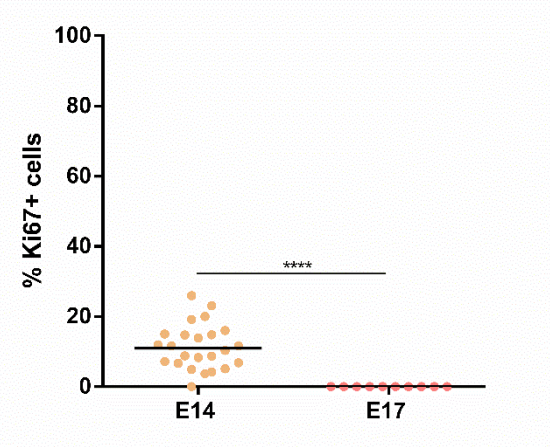

FIGURE 64: Proliferation rate in NR WT iPSC-derived VSMCs
The proliferation rate in E17 (dark green) cells (Median: 0%) was significantly lower than in E14 (light green) cells (Median: 10.99%). Each dot represents % positive cells per well analyzed.

For comparison of the two genotypes, data were merged. The R WT (dark red) iPSC-derived VSMCs showed a significantly higher proliferation rate than the NR WT (orange) cells (Fig. 65). The R WT cells exhibited a median of proliferative cells of around14.3%. NR WT cells on the other hand showed a significantly increased rate of about 5.5% proliferative cells.

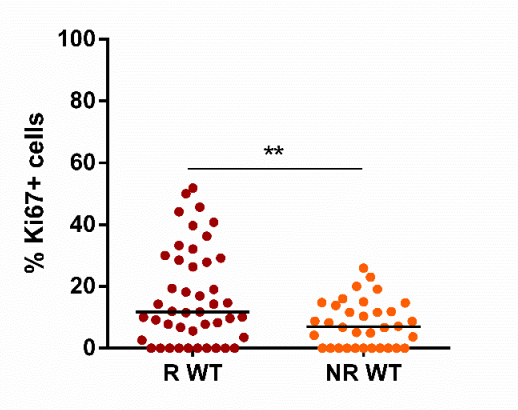

FIGURE 65: Comparison of proliferation rate in R WT vs NR WT iPSC-derived VSMCs
The proliferation rate in R WT cells (Median: 14.3%) was significantly higher than in NR WT cells (Median: 5.5%). Each dot represents % positive cells per well analyzed.

Regarding the characterization of iPSC-derived VSMCs we noticed varying results, even with significant differences between the clones of the same genotype. Altogether, R WT cells showed a significantly higher proliferation rate and a significantly higher migration capacity than NR WT cells.

3.3.3 Calcification of 9p21 NR WT and R WT iPSCs-derived VSMCs

9p21 R WT and NR WT cells were calcified, using the protocol published by Tziakas et al. 2019, as described before. In order to determine, whether they were positively calcified or not, ARS and Calcein stainings were performed.

For R WT cells, one calcification per clone was performed and analyzed. R WT cells showed intermediate ARS staining in each calcification approach for cells treated with the Tziakas cocktail while untreated VSMCs (SMC-) did not show red ARS staining (Fig. 66).

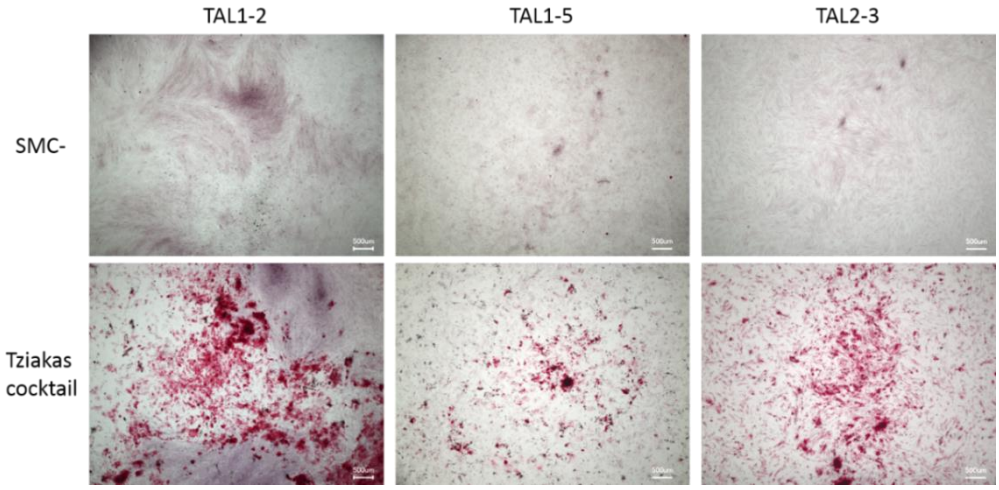

FIGURE 66: ARS staining of R WT cells
Untreated cells (SMC-) did not show any CaP deposition, while treated cells (Tziakas cocktail) displayed intermediate CaP deposition represented by red staining. Representative images per biological replicate are shown above. Scale Bars represent 500 µm.

For NR WT cells one or two biological replicates per clone were performed and analyzed. NR WT cells did not show any positive ARS staining in Tziakas treated VSMCs. Untreated VSMCs (SMC-) remained without staining (Fig. 67).

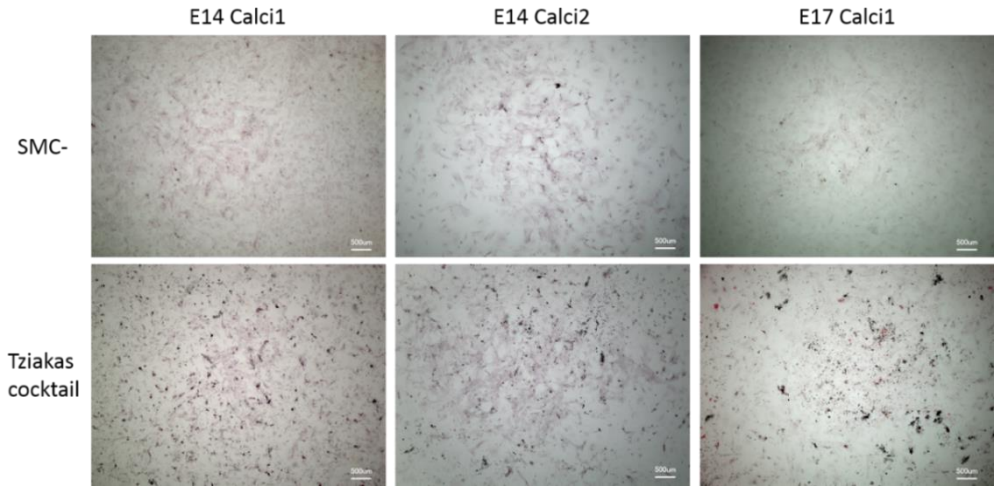

FIGURE 67: ARS staining of NR WT cells
Untreated cells (SMC-) as well as treated cells (Tziakas cocktail) did not show any red ARS staining. Representative images per biological replicate are displayed above. Scale Bars represent 500 µm.

Similar results were obtained by using Calcein staining. R WT cells showed intermediate to strong CaP depositions represented by green fluorescent staining in Tziakas cocktail-treated cells, while untreated VSMCs (SMC-) only show blue DAPI staining (Fig. 68).

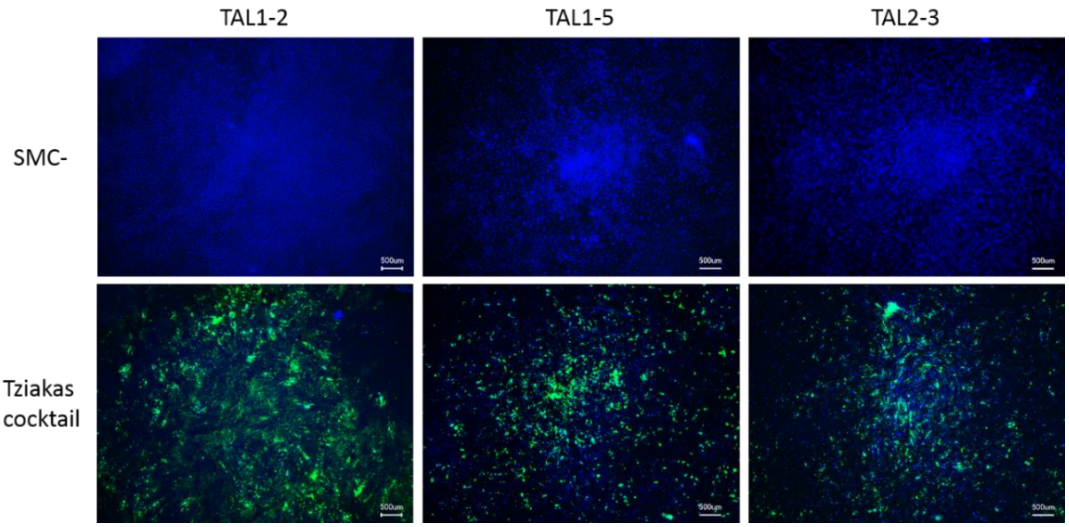

FIGURE 68: Calcein staining of R WT cells
Untreated cells (SMC-) did not show any CaP deposition, while treated cells (Tziakas cocktail) displayed intermediate to strong CaP deposition represented by green fluorescent staining. Representative images per biological replicate are shown above. Scale Bars represent 500 µm.

Calcein staining of NR WT cells remained negative (no green fluorescent staining) in untreated (SMC-) as well as treated (Tziakas cocktail) cells (Fig. 69).

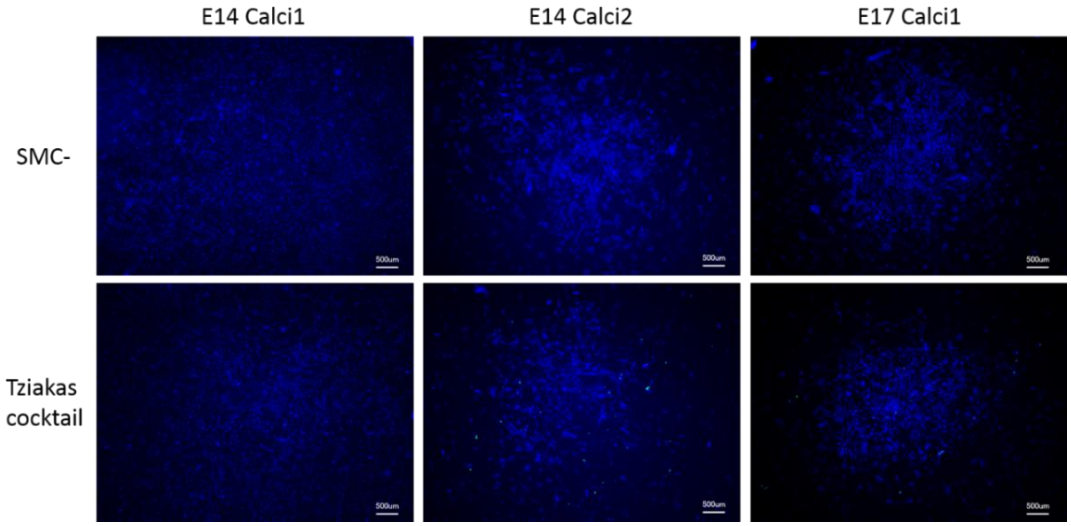

FIGURE 69: Calcein staining of NR WT cells
Untreated cells (SMC-) as well as treated cells (Tziakas cocktail) did not show any CaP deposition. Representative images per biological replicate are displayed above. Scale Bars represent 500 µm.

Concluding, R WT cells showed intermediate ARS and Calcein staining, while NR WT cells did not show positive staining in Tziakas treated VSMCs. Untreated VSMCs (SMC-) remained negative in all cases.

Further, we quantified the CaP depositions using the Calcein images and a Python script. Briefly, green staining from Calcein was compared with blue staining from DAPI. R WT calcifying VSMCs showed a significant increase in Calcein staining between 10- and 40- fold for the clones TAL2-3 and TAL1-5 compared to untreated VSMCs, whilst the clone TAL1-2 does not show a significant increase in Calcein staining (Fig. 70).

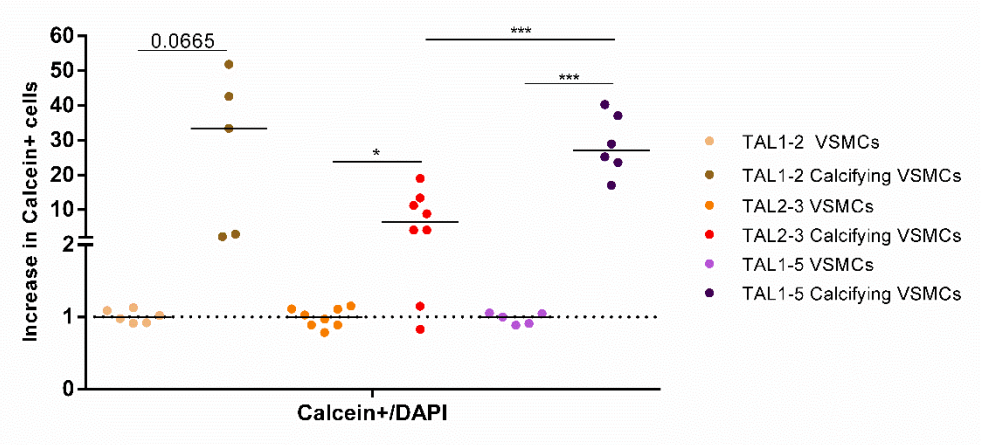

FIGURE 70: Calcein quantification in R WT cells
Treated cells (calcifying VSMCs) showed a significant increase in Calcein staining when compared to untreated cells (VSMCs) for the clones TAL2-3 (red) and TAL1-5 (lilac). For the clone TAL1-2 (brown) no significant increase was detected. Dots represent value per image analyzed.

NR WT cells only showed little to no increase in Calcein staining in calcifying VSMCs compared to untreated VSMCs. In the E14 clone we detected a statistically significant increase in CaP deposition up to 1.5-fold (Fig. 71). For the clone E17 no significant increase in the Calcein staining was detected (Fig. 71).

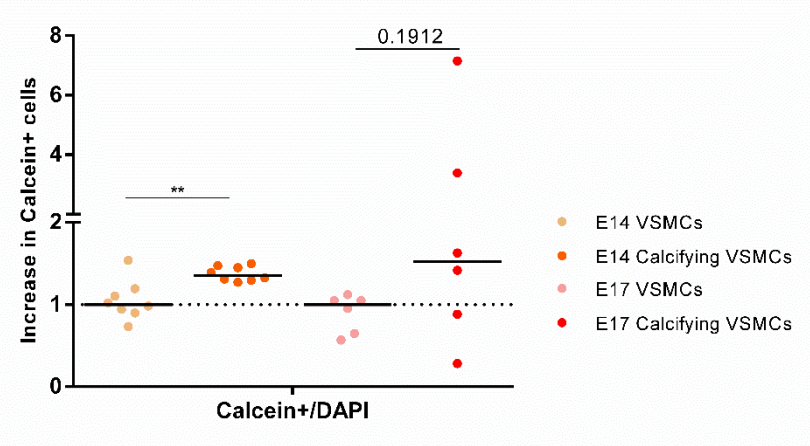

FIGURE 71: Calcein quantification in NR WT cells
Treated cells (calcifying VSMCs) showed little increase in Calcein staining when compared to untreated cells (VSMCs). A statistical significant increase to almost 1.5-fold between VSMCs and calcifying VSMCs in the clone E14 (orange) was detected, while for E17 (red) the increase was not significant. Dots represent value per image analyzed.

In order to compare the CaP deposition in R WT and NR WT cells we merged the data from the single clones. The R WT cells showed a significantly higher level in CaP deposition in calcifying cells than NR WT cells. Calcein was increased to around 20-fold in R WT cells, while NR WT cells showed an increase of about 1.5-fold (Fig. 72).

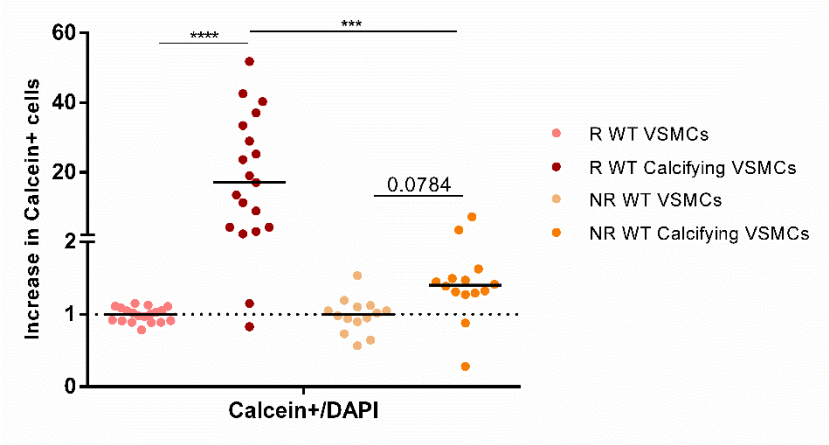

FIGURE 72: Comparison of Calcein quantifications of R WT and NR WT cells
R WT (red) calcifying cells displayed significantly higher levels (~20-fold increase) of CaP deposits than NR WT (orange) (~1.5-fold increase) calcifying cells. Untreated VSMCs of both genotypes did not show differences in CaP deposition. Dots represent value per image analyzed.

After assessing the calcification on cellular level we examined the calcification on molecular level, by analyzing the RNA expression of calcification-associated markers *ALPL*, *CTSK*, *CSF1*, *RUNX2,* and *OPN/SSP*.

We started by analyzing the expression of *ALPL* in R WT clones TAL1-2, TAL2-3 and TAL1-5. TAL1-2 (orange) showed a statistically significant increase of 2-fold expression fold change in *ALPL* expression in calcifying VSMCs compared to untreated VSMCs (Fig. 73). The clone TAL2-3 (blue) displayed a significant decrease in *ALPL* expression to almost zero in calcifying VSMCs compared to untreated VSMCs (Fig. 73). TAL1-5 cells (green) did not show significant changes in RNA expression of *ALPL* in calcifying VSMCs compared to VSMCs (Fig. 73).

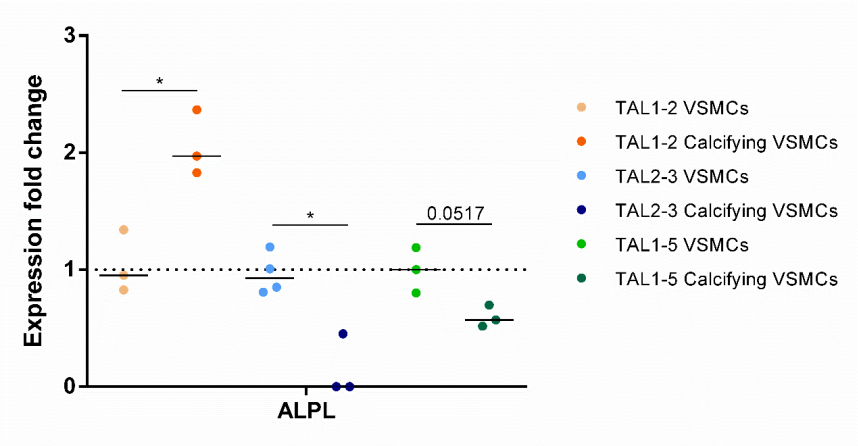

FIGURE 73: RNA expression of *ALPL* in R WT cells
ALPL expression was statistically significant increased in cells of the TAL1-2 clone (orange) to almost 2-fold. Cells of the TAL2-3 (blue) clone showed a significant decrease in *ALPL* expression to almost zero, whilst TAL1-5 cells (green) did not show significant differences in *ALPL* expression. Dots represent median per technical replicate analyzed.

Following, the expression of *CTSK* in R WT clones TAL1-2, TAL2-3 and TAL1-5 was analyzed. TAL1-2 (orange) showed a significant increase in *CTSK* expression of around 5.5-fold in calcifying VSMCs compared to untreated VSMCs (Fig. 74). The clones TAL2-3 (blue) and TAL1-5 cells (green) on the other hand displayed a significant decrease in *CTSK* expression in calcifying VSMCs compared to untreated VSMCs (Fig. 74).

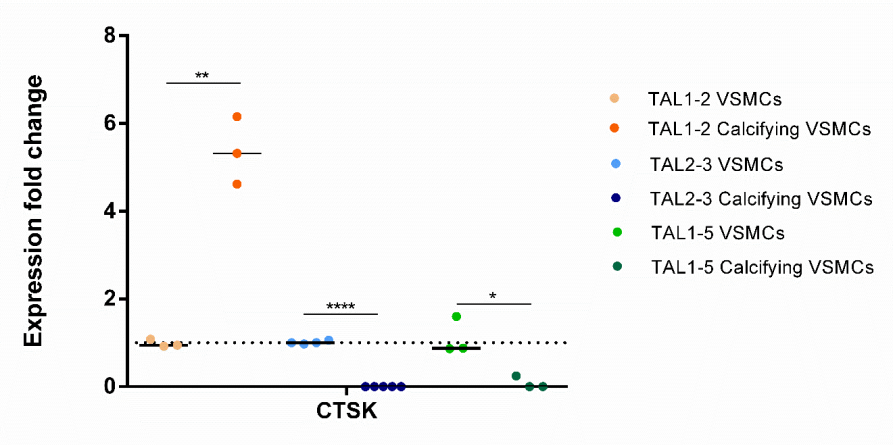

FIGURE 74: RNA expression of *CTSK* in R WT cells
CTSK expression was significantly increased in cells of the TAL1-2 clone (orange) to around 5.5-fold. Cells of the TAL2-3 (blue) clone and the TAL1-5 cells (green) clone showed a significant decrease to almost zero in *CTSK* expression. Dots represent median per technical replicate analyzed.

Further, the expression of *CSF1* in R WT clones TAL1-2, TAL2-3 and TAL1-5 was analyzed. TAL1-2 (orange) showed a statistically significant increase of 2.5-fold in *CSF1* expression in calcifying VSMCs compared to untreated VSMCs (Fig. 75). The clone TAL2-3 (blue) displayed a significant decrease to almost zero in *CSF1* expression in calcifying VSMCs compared to untreated VSMCs (Fig. 75). TAL1-5 cells (green) did not show significant changes in *CSF1* expression (Fig. 75).

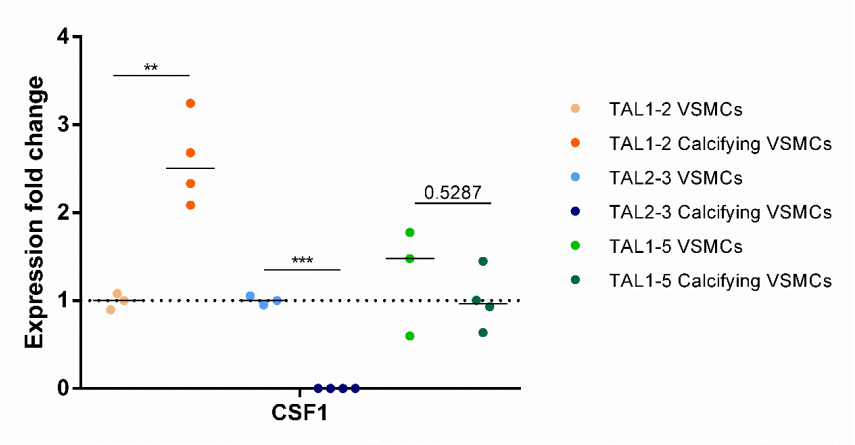

FIGURE 75: RNA expression of *CSF1* in R WT cells
CSF1 expression was statistically significant increased to around 2.5-fold in cells of the TAL1-2 clone (orange). Cells of the TAL2-3 (blue) clone showed a significant decrease in *CSF1* expression, whilst TAL1-5 cells (green) did not show significant differences in *CSF1* expression. Dots represent median per technical replicate analyzed.

RUNX2 as late-stage calcification marker was analyzed in R WT cells. The clones TAL1-2 (orange) and TAL1-5 (green) showed statistically significant increases

between 1.5 and 2-fold in *RUNX2* expression (Fig. 76). TAL2-3 cells (blue) did not show significant differences in the expression of *RUNX2* (Fig. 76).

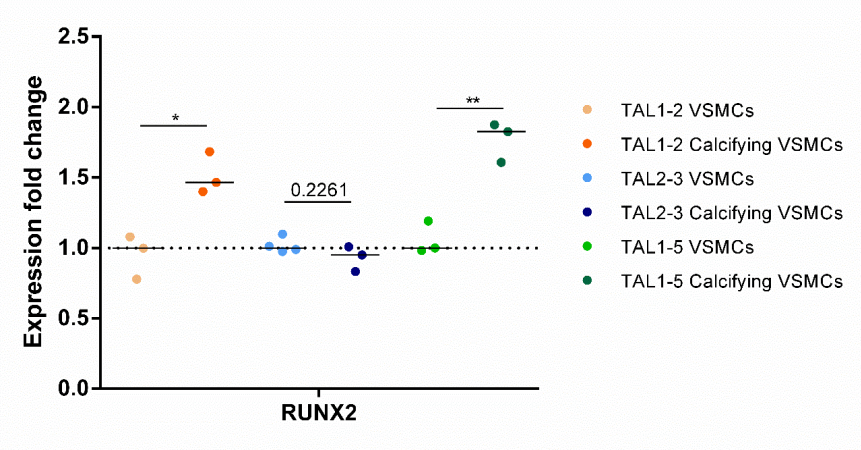

FIGURE 76: RNA expression of *RUNX2* in R WT cells
RUNX2 expression was statistically significant increased in cells of the TAL1-2 clone (orange) and the TAL1-5 clone (green) to 1.5 to 2-fold. Cells of the TAL2-3 (blue) clone did not show significant differences in *RUNX2* expression. Dots represent median per technical replicate analyzed.

Finally, *OPN/SSP* was analyzed in R WT cells. As terminal calcification marker, *OPN/SSP* was not significantly altered in all three clones (Fig. 77). However, the clone TAL2-3 (blue) showed a strong tendency of upregulation around 4-fold of *OPN/SSP* in calcifying VSMCs compared to untreated VSMCs.

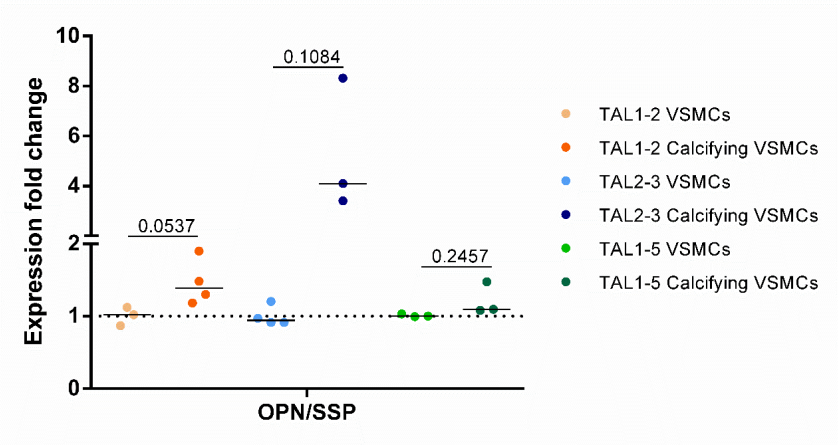

FIGURE 77: RNA expression of *OPN/SSP* in R WT cells
OPN/SSP expression is not changed in cells of all three clones. In the clone TAL2-3 (blue) the calcifying VSMCs show a tendency towards upregulation around 4-fold of *OPN/SSP* compared to untreated VSMCs. Dots represent median per technical replicate analyzed.

Altogether, a few calcification markers were changed in their expression in calcifying cells compared to untreated VSMCs. Further, the direction of regulation differed between the clones of the R WT cells line for the investigated calcification markers.

The same analyses were performed for the NR WT cells. The expression of *ALPL* was significantly reduced to zero in calcifying cells compared to VSMCs of both clones (Fig. 78).

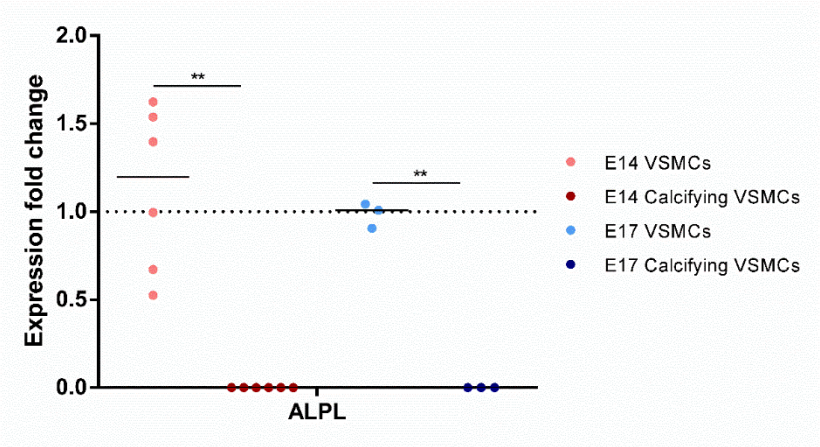

FIGURE 78: RNA expression of *ALPL* in NR WT cells
ALPL expression was significantly downregulated in calcifying cells of the clones E14 (red) and E17 (blue) to almost zero. Dots represent median per technical replicate analyzed.

The expression of *CTSK* in NR WT cells was significantly decreased to almost zero in calcifying cells compared to untreated VSMCs of both clones, E14 (red) and E17 (blue) (Fig. 79).

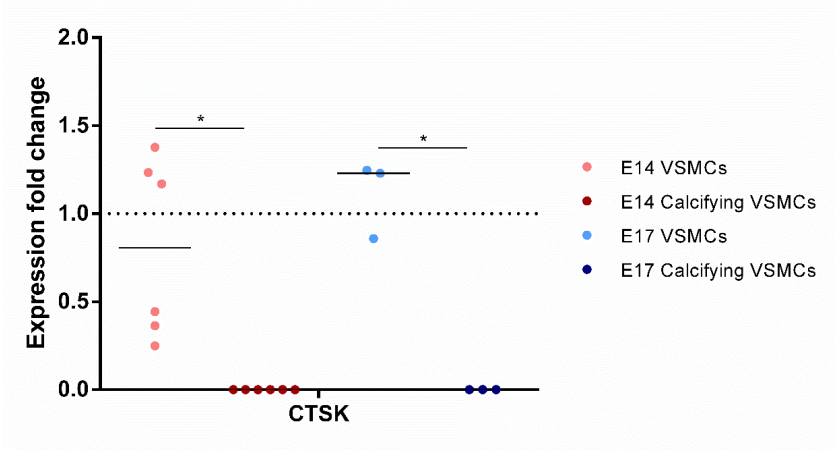

FIGURE 79: RNA expression of *CTSK* in NR WT cells
CTSK expression was significantly downregulated in calcifying cells of the clones E14 (red) and E17 (blue). Dots represent median per technical replicate analyzed.

The expression of *CSF1* as intermediate calcification marker was significantly downregulated in the clone E14 (red) to zero of the NR WT genotype. In the E17 (blue) the expression was not changed between untreated VSMCs and calcifying VSMCs, as the untreated VSMCs already did not show any expression of this gene (Fig. 80).

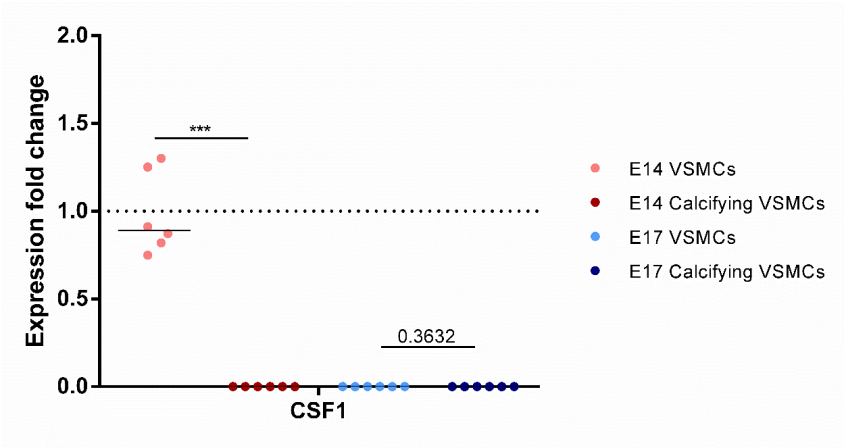

FIGURE 80: RNA expression of *CSF1* in NR WT cells
CSF1 expression was significantly downregulated in calcifying cells of the clone E14 (red). The clone E17 (blue) did not show changes in expression of *CSF1*. Dots represent median per technical replicate analyzed.

The expression of *RUNX2*, a late stage calcification marker, was unchanged in the clone E14 (red), whilst in E17 (blue) the expression of *RUNX2* was significantly downregulated to zero (Fig. 81).

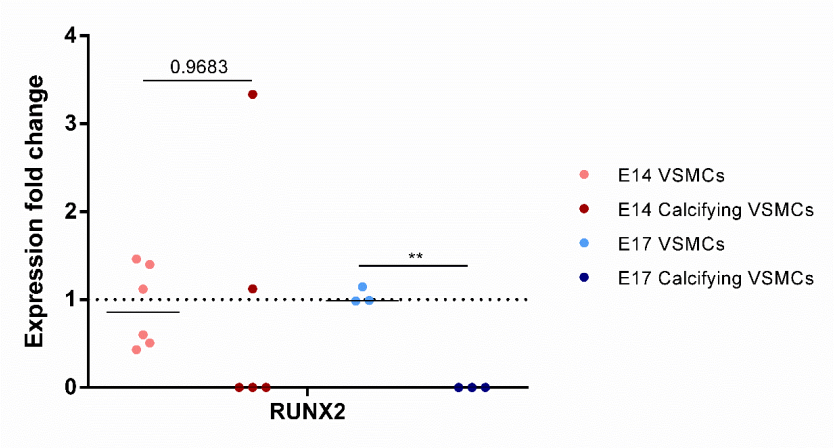

FIGURE 81: RNA expression of *RUNX2* in NR WT cells
RUNX2 expression was not changed in calcifying cells of the clone E14 (red). Cells of the clone E17 (blue) showed a decrease to zero in the expression of *RUNX2*. Dots represent median per technical replicate analyzed.

Finally, the expression of *OPN/SSP* was analyzed. In both clones, E14 (red) and E17 (blue), of the NR WT genotype the expression of *OPN/SSP* was not significantly changed in calcifying VSMCs compared to untreated VSMCs (Fig. 82).

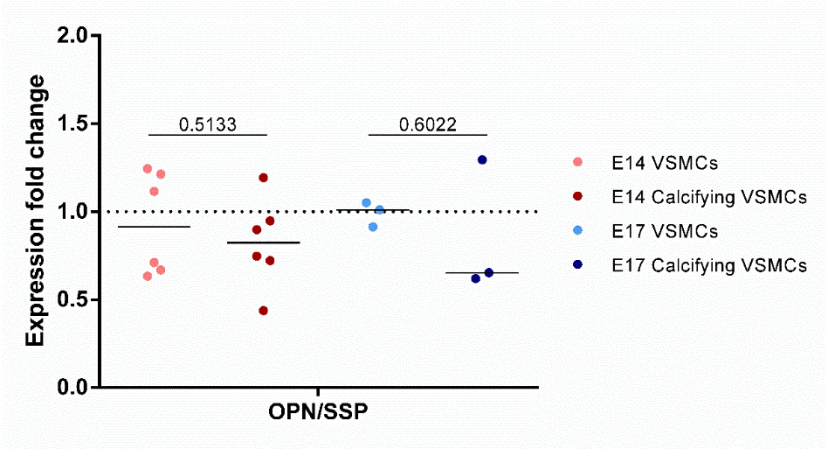

FIGURE 82: RNA expression of *OPN/SSP* in NR WT cells
OPN/SSP expression was not changed in calcifying cells of the clones E14 (red) and E17 (blue). Dots represent median per technical replicate analyzed.

Most calcification associated markers were not changed in calcifying cells of the NR WT genotype. Additionally, NR WT cells did not show positive ARS and Calcein staining in Tziakas cocktail-treated VSMCs. R WT cells on the other hand showed positive ARS and Calcein staining, but the molecular regulation differed significantly between the clones in calcifying VSMCs compared to untreated VSMCs.

3.4 Differentiation of 9p21 NR KO and R KO iPSC towards VSMCs and their calcification

KO lines served as control towards cell line-dependent effects which need to be differentiated from risk SNP-dependent effects. Therefore, KO clones of the NR cell line HE463_7 (E50, E56) and the R cell line C512 (TAL1-9, WB46) were treated in the same way as the 18i-3-6 and WT clones of both cell lines.

3.4.1 Characterization of 9p21 R KO and NR KO iPSCs

First, the NR KO and R KO iPSCs were analyzed, regarding their morphology, as well as expression and protein localization of the pluripotency-associated marker NANOG. Both, R KO and NR KO iPSCs displayed a typical iPSC morphology, such as round shaped colonies with defined colony boundaries. Further, the cells grew cobblestone-like, round shaped, with few cytoplasm and big nuclei. Human iPSCs of the NR KO and R KO cell lines were also stained for NANOG in IF staining to show its localization in the nuclei. No differences could be seen between the NR KO and R KO cells regarding their morphology or the expression of NANOG in IF staining (Fig. 83).

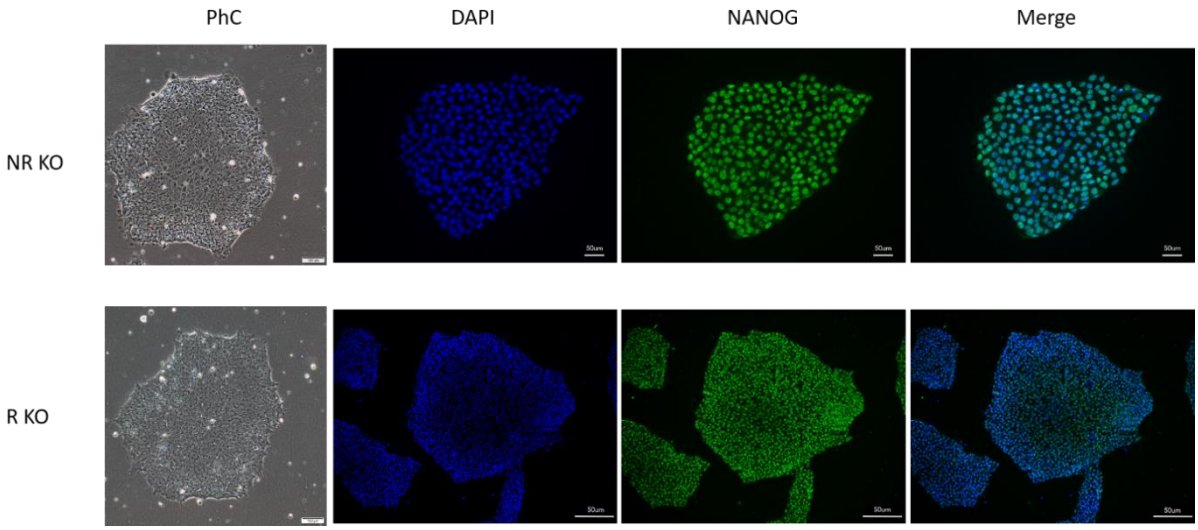

FIGURE 83: IF staining of 9p21 NR KO and R KO iPSC colonies
NR KO (top) and R KO (bottom) iPSCs display comparable, typical iPSC morphology in bright field. Further, both express NANOG (green) in the nuclei of the iPSCs; Nuclei are counterstained with DAPI (blue). Scale bars represent 200 µm for PhC and 50 µm for IF staining images.

On cellular and morphological level, we did not see any significant differences between iPSCs of the R KO or NR KO genotype.

3.4.2 Differentiation of 9p21 R KO and NR KO iPSCs towards VSMCs

Following the differentiation protocol described above, R KO and NR KO iPS cells were differentiated into VSMCs. Resulting VSMCs were characterized regarding their expression status of pluripotency-associated markers as well as SMC-specific markers on RNA and protein level. First, IF staining were performed confirming the expression of CNN1 and TAGLN on protein level and their correct localizations within the contractile fibers and the cytoplasm of the cells (Fig. 84).

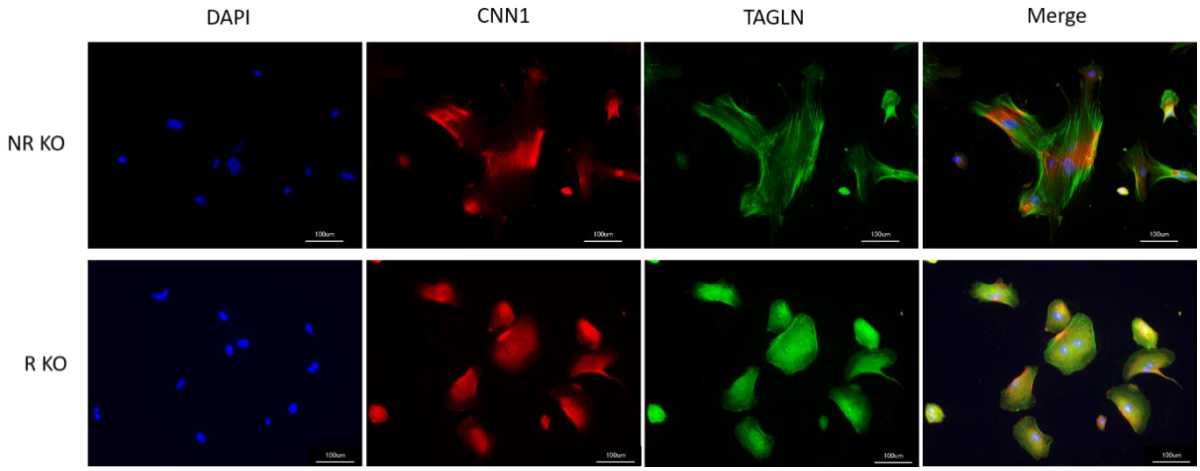

FIGURE 84: IF staining of 9p21 NR KO and R KO iPSC-derived VSMCs
NR KO (top) and R KO (bottom) VSMCs express TAGLN (green) and CNN1 (red) in the contractile apparatus and the cytoplasm of the VSMCs; Nuclei are counterstained with DAPI (blue). Scale bars represent 100 µm.

For the R KO and NR KO cells we further estimated the differentiation efficiency via the IF staining of CNN1 and TAGLN in iPSC-derived VSMCs. The majority of the R KO as well as the NR KO iPSC-derived VSMCs displayed an overall CNN1 and TAGLN overlap and, therefore a differentiation efficiency, above 95% (Fig. 85). Differentiation efficiencies were highly similar in R KO and NR KO.

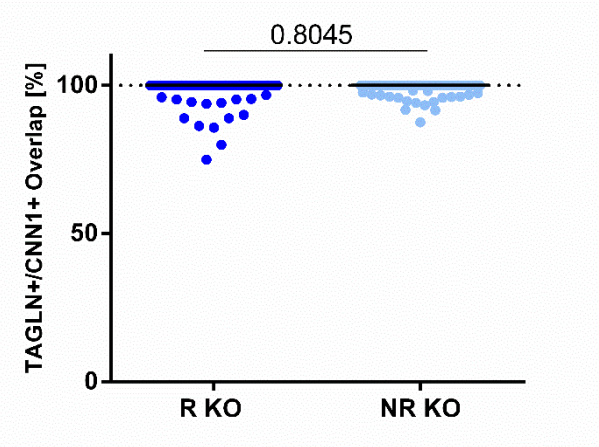

FIGURE 85: Differentiation efficiency of R KO vs NR KO cells
R KO (blue) and NR KO (light blue) VSMCs expressed TAGLN and CNN1 with an overlap of above 95%. There were no significant difference between cells of the NR KO and the R KO cell lines. Dots represent % positive cells per image analyzed.

Following the microscopical analyses we performed qPCR for pluripotency- and SMC-associated markers to examine the molecular regulation of the differentiation in iPSC-derived VSMCs for R KO and NR KO cells. At first, we started with the analysis of the single R KO (Fig. 86) and NR KO clones (Fig. 87) in order to identify possible differences between the clones.

Both R KO clones TAL1-9 and WB46 showed a significant downregulation to almost zero for the expression of pluripotency-associated markers in iPSC-derived VSMCs compared to iPSCs (Fig. 86). No significant differences were detected between the expression profiles of both clones.

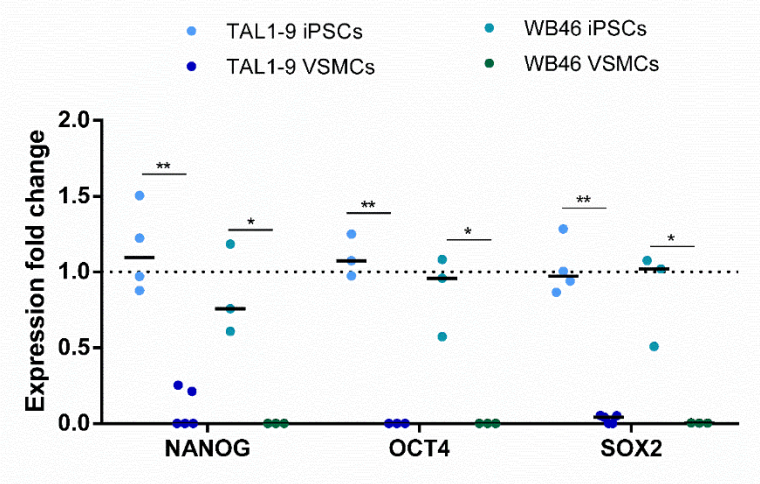

FIGURE 86: RNA expression analysis of R KO clones for pluripotency-associated markers
RNA expression analyses showed a significant downregulation of the pluripotency markers *NANOG*, *OCT4*, and *SOX2* in iPSC-derived VSMCs compared to iPSCs in both R KO clones. N.s. t-test not indicated in the Figure. Each dot represents median of technical replicates.

The same applied to the NR KO clones E50 and E56 (Fig. 87). Both clones showed a significant downregulation to almost zero in the RNA expression of the pluripotency-associated markers *NANOG*, *OCT4*, and *SOX2*. Further, a statistical difference in the expression of *SOX2* between E50 and E56 iPSC-derived VSMCs was detected (Fig. 87).

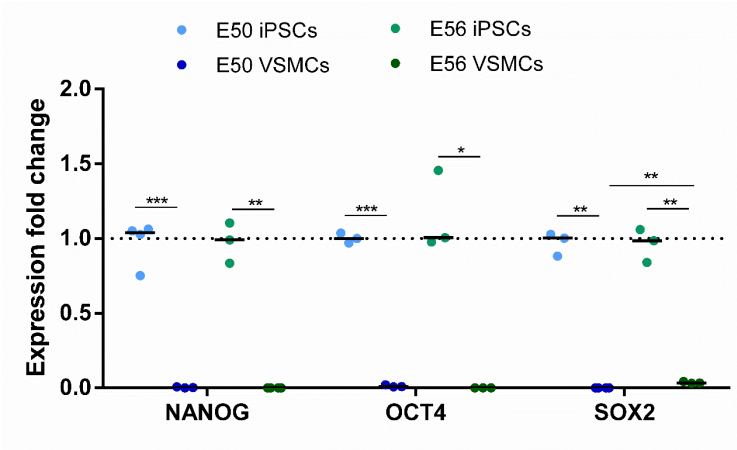

FIGURE 87: RNA expression analysis of NR KO clones for pluripotency-associated markers
RNA expression analyses showed a significant downregulation of the pluripotency markers *NANOG, OCT4,* and *SOX2* in iPSC-derived VSMCs compared to iPSCs in both NR KO clones. A statistical difference in the *SOX2* expression between E50 (blue) and E56 (green) was detected. N.s. t-test not indicated in the Figure. Each dot represents median of technical replicates.

For final analysis of the genotypes data of the R KO clones and the NR KO clones were merged respectively. The RNA expression of pluripotency-associated markers in R KO (orange) and NR KO (blue) iPSCs and iPSC-derived VSMCs did not show significant differences (Fig. 88).

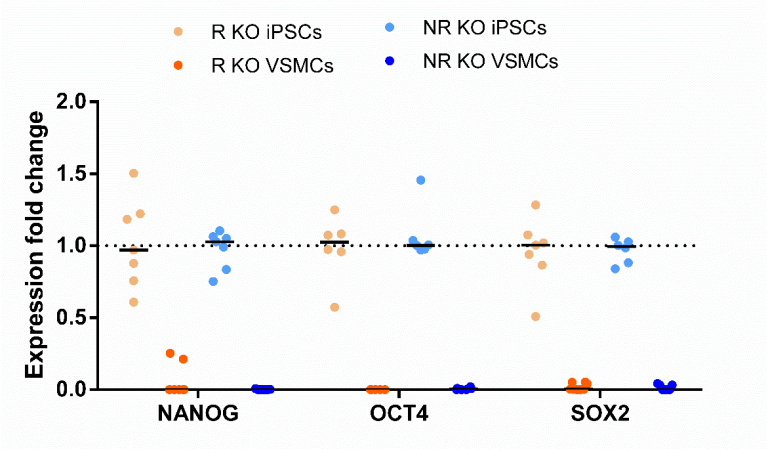

FIGURE 88: RNA expression analysis of NR KO vs R KO cells of pluripotency markers
RNA expression of the pluripotency markers *NANOG, OCT4,* and *SOX2* in iPSC-derived VSMCs compared to iPSCs showed no significant differences between R KO (orange) and NR KO (blue) cells. N.s. t-test not indicated in the Figure. Each dot represents median of technical replicates.

Further, we analyzed the RNA expression of SMC-specific markers in R KO (Fig. 89) and NR KO (Fig. 90) iPSCs and iPSC-derived VSMCs. Again, we started with the analysis in the R KO clones TAL1-9 and WB46, that both showed significant upregulation of RNA expression of SMC-specific markers between 2- and almost 15-fold (Fig. 89). Statistical significant differences between the two clones were detected in the expression of *TAGLN* and *CALD1* (Fig. 89).

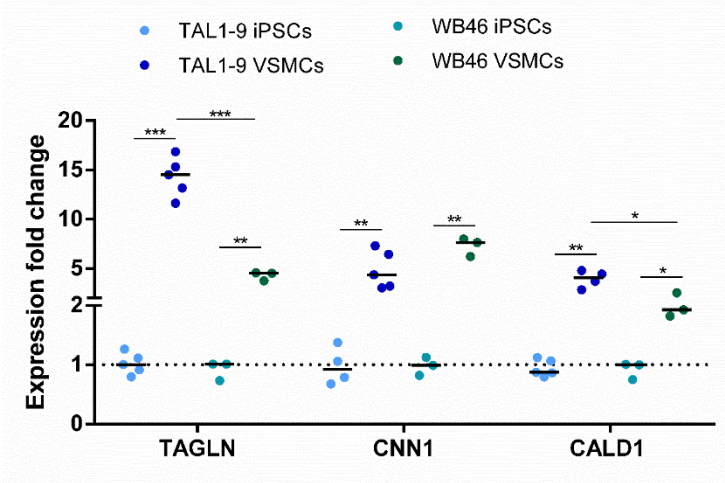

FIGURE 89: RNA expression analysis of R KO clones for SMC-markers
RNA expression analyses showed a significant upregulation of the SMC-markers *TAGLN, CNN1,* and *CALD1* in iPSC-derived VSMCs compared to iPSCs in both R KO clones. Statistical differences between the cell lines were detected in the expression of *TAGLN* and *CALD1*. N.s. t-test not indicated in the Figure. Each dot represents median of technical replicates.

The same applied to the NR KO clones E50 and E56. The RNA expression of SMC-specific markers was significantly upregulated in iPSC-derived VSMCs in both clones between 3- up to above 10-fold (Fig. 90). Statistical significant differences in the expression between both clones was detected for *TAGLN* (Fig. 90).

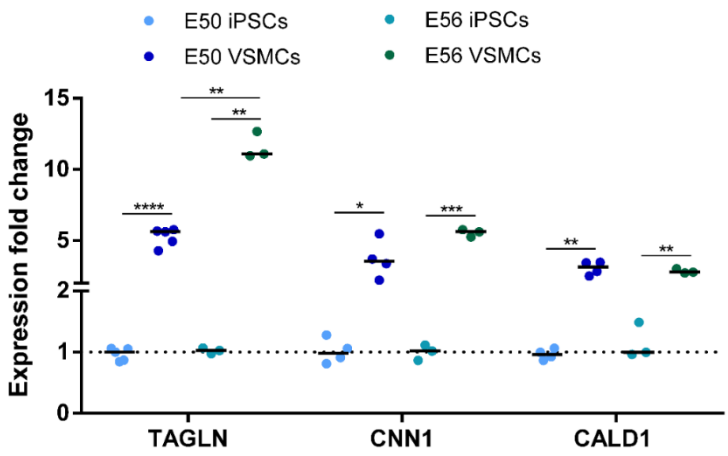

FIGURE 90: RNA expression analysis of NR KO clones SMC-markers
RNA expression analyses showed a significant upregulation of the SMC-markers *TAGLN, CNN1,* and *CALD1* in iPSC-derived VSMCs compared to iPSCs in both NR KO clones. A statistical difference in the *TAGLN* expression between E50 (blue) and E56 (green) was detected. N.s. t-test not indicated in the Figure. Each dot represents median of technical replicates.

Finally, the clones of both genotypes were merged in order to compare the RNA expression of the R KO with the NR KO (Fig. 91). No significant differences in the expression of SMC-specific markers between R KO and NR KO cells were detected (Fig. 91).

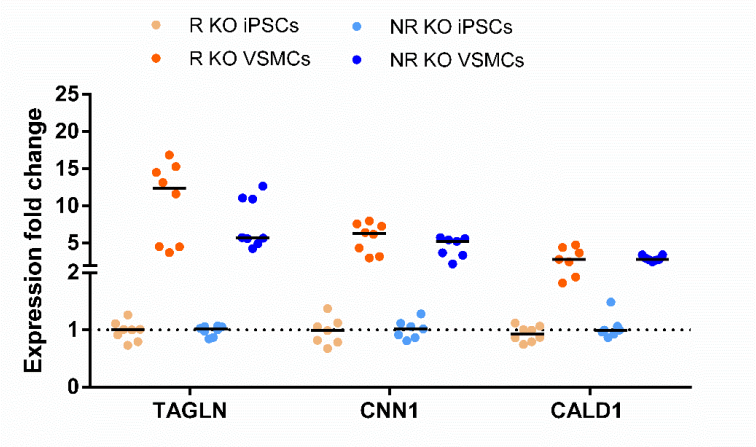

FIGURE 91: RNA expression analysis of NR KO vs R KO cells for SMC-markers
RNA expression of the pluripotency markers *TAGLN, CNN1,* and, *CALD1* in iPSC-derived VSMCs compared to iPSCs showed no significant differences between R KO (orange) and NR KO (blue) cells. N.s. t-test not indicated in the Figure. Each dot represents median of technical replicates.

The molecular regulation of the differentiation was also assessed on protein level using WB analyses.

R KO cells were analyzed for the protein expression of OCT4 and TAGLN in iPSCs and iPSC-derived VSMCs. We detected a significant downregulation of OCT4 protein

expression in R KO iPSCs-derived VSMCs compared to iPSCs to between 0.2 and zero (Fig. 92A/B). TAGLN protein expression was significantly increased in TAL1-9 iPSC-derived VSMCs compared to iPSCs to around 7.5-fold (Fig. 92A/B). In the clone WB46 TAGLN expression was not significantly increased, yet a tendency towards upregulation of protein expression was visible (Fig. 92B). Significant differences in protein expression of the VSMCs of both clones of the R KO genotype was detected for OCT4 as well as TAGLN.

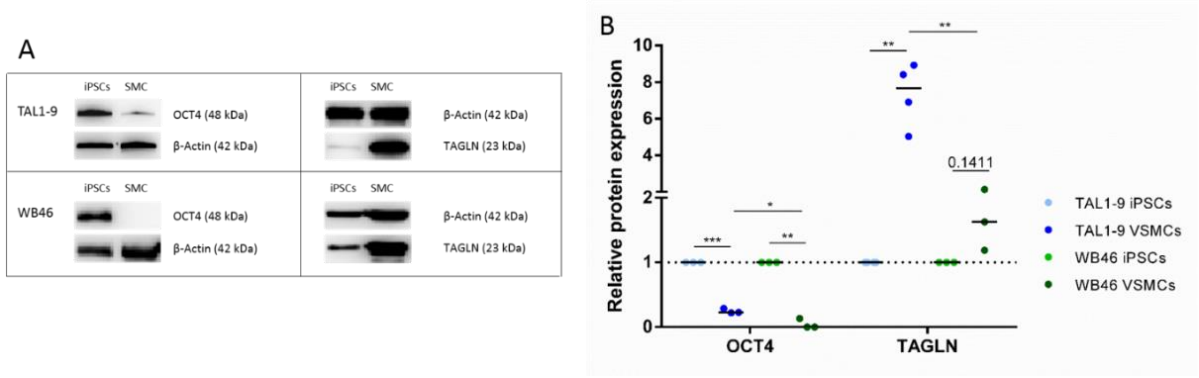

FIGURE 92: Protein expression analysis of R KO cells
A) Representative Blots for R KO cells of OCT4 and TAGLN protein expression.
B) Quantification of protein expression shows significant decrease in OCT4 expression in iPSC-derived VSMCs. TAGLN was not significantly upregulated in WB46 (green) VSMCs, but a tendency towards increased protein expression was visible. In TAL1-9 (blue) VSMCs TAGLN expression was significantly upregulated to 7.5-fold. Each dot represents blot analyzed.

NR KO cells were analyzed for the protein expression of OCT4 and TAGLN (Fig. 93A). OCT4 was significantly downregulated to almost zero in iPSC-derived VSMCs compared to iPSCs (Fig. 93B). TAGLN was not significantly upregulated in iPSC-derived VSMCs, however a tendency could be shown (Fig. 93B).

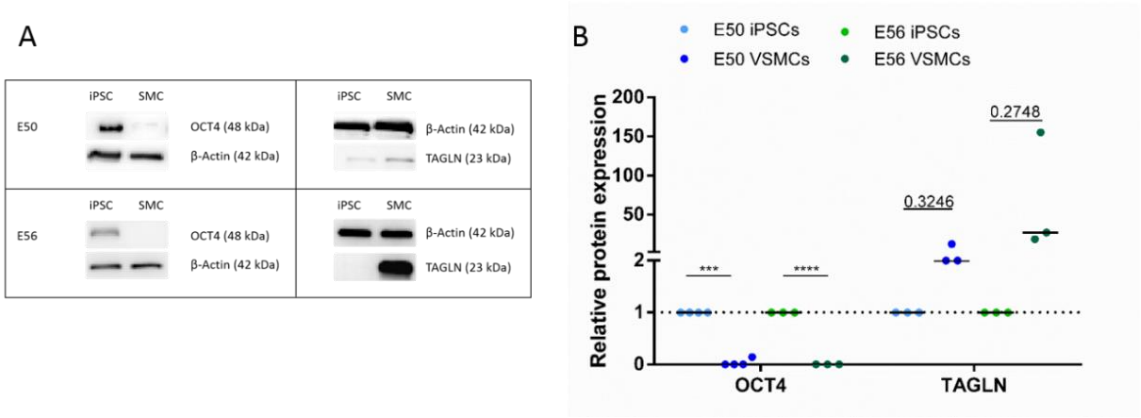

FIGURE 93: Protein expression analysis of NR KO cells
A) Representative Blots for NR KO cells of OCT4 and TAGLN.
B) Quantification of protein expression shows significant decrease to almost zero in OCT4 expression in iPSC-derived VSMCs of the NR KO clones E50 (blue) and E56 (green). TAGLN was not significantly upregulated in both clones, but a tendency towards increase in protein expression was visible in iPSC-derived VSMCs compared to iPSCs. Each dot represents Blot analyzed.

After examination of the iPSC and VSMC properties we characterized the iPSC-derived VSMCs as already described above.

In order to characterize the VSMC behavior we performed migration assays of the iPSC-derived VSMCs using a scratch assay. To begin with, we performed analyses of the R KO clones TAL1-9 and WB46 (Fig. 94). Both clones displayed a similar migration rate of 27.66% (TAL1-9) and 22.64% (WB46) in median that was not significantly different from each other (Fig. 94).

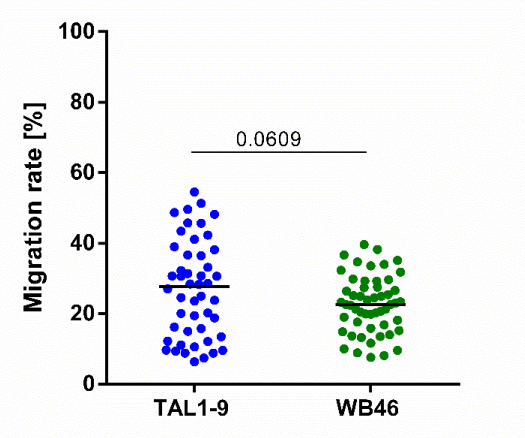

FIGURE 94: Migration rate of the R KO clones
The migration assay of the R WT clones TAL1-9 (blue) and WB46 (green) did not show significant differences in migration rate (27.66% vs 22.64%). Each dot represents migration rate per well analyzed.

Following, we performed the same analysis for NR KO iPSC-derived VSMCs. Both clones did not show significant differences in the migration rate of 23.71% (E50) versus 18.37% (E56) (Fig.95).

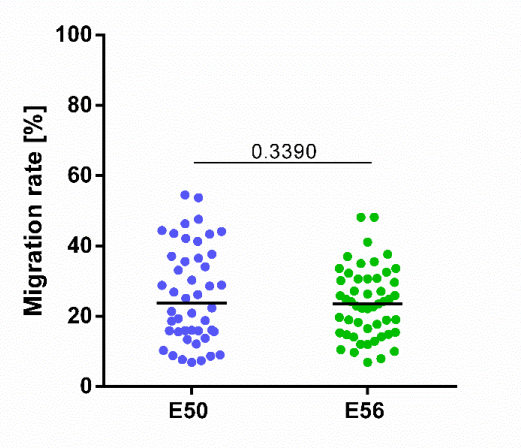

FIGURE 95: Migration rate of the NR KO clones
The migration assay of the NR WT clones E50 (blue) and E56 (green) did not show significant differences in migration rate (23.71% vs 18.37% respectively). Each dot represents migration rate per well analyzed.

We then compared the two genotypes with each other. The migration rate of R KO and NR KO iPSC-derived VSMCs did not differ significantly (23.78% vs 23.51% respectively) (Fig. 96).

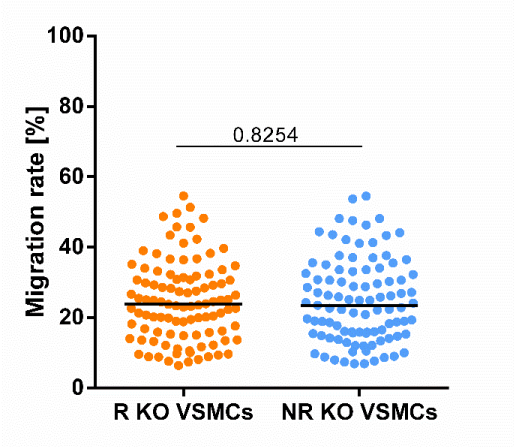

FIGURE 96: Comparison of migration rate of R KO and NR KO iPSC-derived VSMCs
The migration rate of R KO (orange) and NR KO (blue) cells did not show significant differences (23.78% vs 23.51% respectively). Each dot represents migration rate per well analyzed.

Finally, we performed proliferation assays via Ki67 staining. The percentage of Ki67+ cells was evaluated in relation to total cell number, estimated by cell count via DAPI staining. The R KO clones TAL1-9 and WB46 did just not show significant differences

in proliferation rate (Fig. 97). TAL1-9 showed a proliferation rate of approximately 38%, while WB46 cells showed a lower proliferation rate of around 22% (Fig. 97).

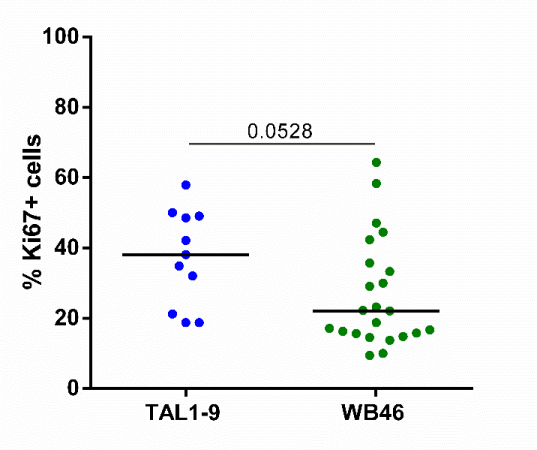

FIGURE 97: Proliferation rate of the R KO clones
The proliferation of R KO clones TAL1-9 (blue, 38.10%) and WB46 (green, 22.06%) did not differ significantly. Each dot represents migration rate per well analyzed.

The same experiment was performed for the NR KO clones E50 and E56. Again, the two clones E50 (24.24%) and E56 (20.00%) were not significantly different in their proliferation rate (Fig. 98).

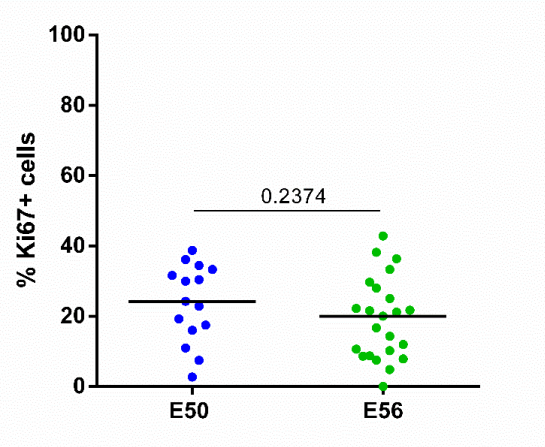

FIGURE 98: Proliferation rate of the NR KO clones
The proliferation of NR KO clones E50 (24.24%) and E56 (20.00%) did not differ significantly. Each dot represents migration rate per well analyzed.

Finally, we compared R KO and NR KO iPSC-derived VSMCs regarding their proliferative capacity. R KO cells (30.08%) displayed a significantly lower proliferation rate, than NR KO (22.12%) iPSC-derived VSMCs (Fig. 99).

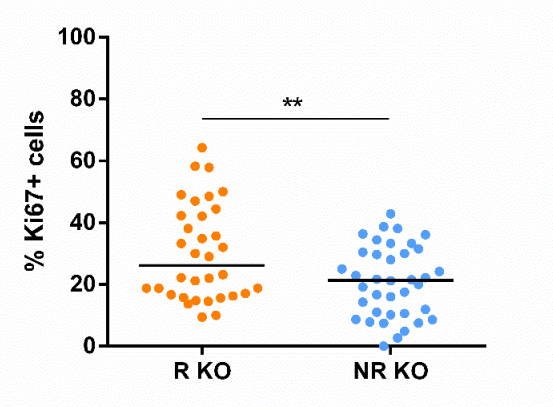

FIGURE 99: Proliferation rate of R KO and NR KO cells
The proliferation of R KO cells (orange, 30.08%) showed a significantly higher proliferation rate than NR KO cells (blue, 22.12%). Each dot represents migration rate per well analyzed.

In summary, we did not detect any significant differences in the migration rates of NR KO and R KO iPSC-derived VSMCs. In terms of proliferation rate, we identified a significantly increased proliferation rate in R KO cells compared to NR KO cells.

3.4.3 Calcification of 9p21 NR KO and R KO iPSC-derived VSMCs

As described above, iPSC-derived VSMCs of the NR KO and R KO genotype were calcified using a protocol published by Tziakas et al., in 2019. In order to determine whether the calcification was successful, ARS and Calcein staining were performed.
For the R KO clone TAL1-9 three biological replicates were analyzed. All three approaches showed positive ARS staining varying from faint to strong intensity in calcifying cells (Tziakas cocktail), while untreated VSMCs (SMC-) did not show any staining (Fig. 100).

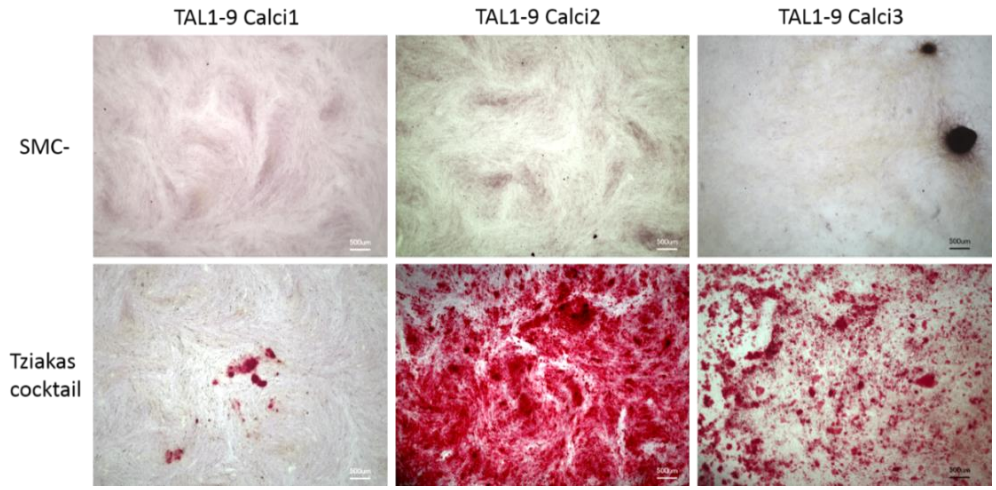

FIGURE 100: ARS staining of the R KO clone TAL1-9
Untreated cells (SMC-) did not show any CaP deposition, while treated cells (Tziakas cocktail) displayed little to strong CaP deposition represented by red staining. Representative images per biological replicate are shown above. Scale Bars represent 500 µm.

For the R KO clone WB46 three biological replicates were analyzed, too. All three calcification approaches showed little to intermediate ARS staining in Tziakas cocktail-treated cells while untreated VSMCs (SMC-) did not show signs of staining (Fig. 101).

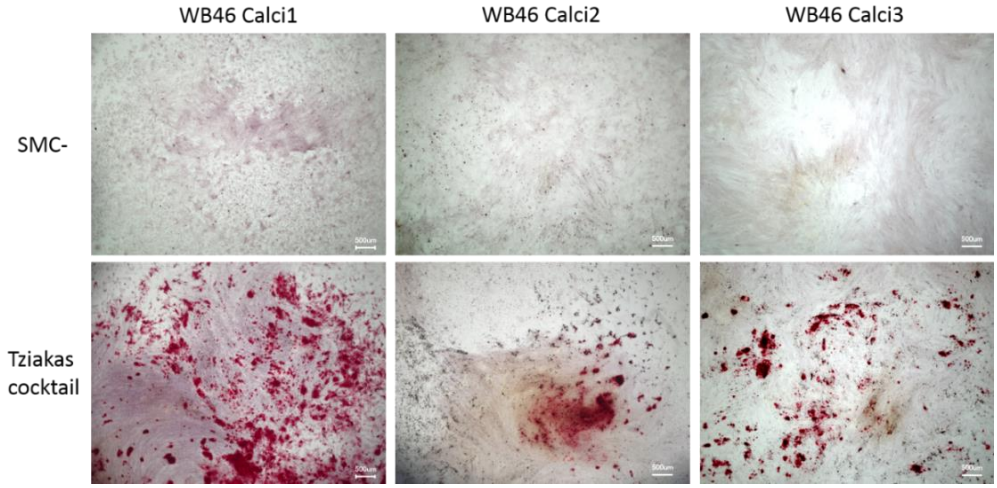

FIGURE 101: ARS staining of R KO clone WB46
Untreated cells (SMC-) did not show any CaP deposition, while treated cells (Tziakas cocktail) displayed little to strong ARS staining. Representative images per biological replicate are shown above. Scale Bars represent 500 µm.

For the NR KO cells one or two biological replicates per clone were analyzed. They showed varying results from little to strong staining in Tziakas cocktail-treated VSMCs. Untreated VSMCs (SMC-) did not show red staining (Fig. 102).

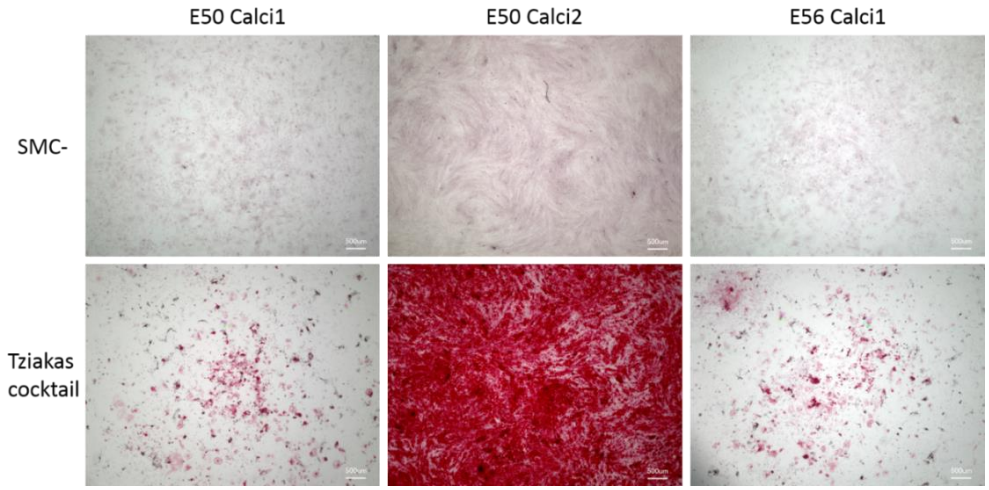

FIGURE 102: ARS staining of the NR KO calcifying cells
Untreated cells (SMC-) did not show any CaP deposition, while treated cells (Tziakas cocktail) displayed little to strong ARS staining. Representative images per biological replicate are shown above. Scale Bars represent 500 µm.

Similar results were obtained using Calcein staining represented in green fluorescent staining.

The R KO clone TAL1-9 showed little to strong staining in treated VSMCs. Untreated VSMCs (SMC-) showed no Calcein staining in all experiments (Fig. 103).

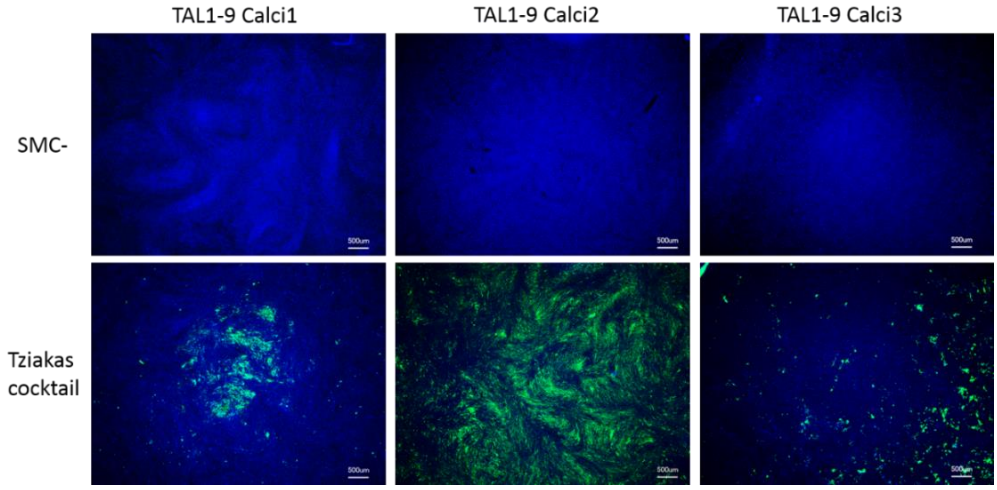

FIGURE 103: Calcein staining of the R KO clone TAL1-9
Untreated cells (SMC-) did not show any CaP deposition, while treated cells (Tziakas cocktail) displayed little to strong Calcein staining. Representative images per biological replicate are shown above. Scale Bars represent 500 µm.

The R KO clone WB46 displayed little to intermediate fluorescent signals in Calcein staining in treated VSMCs, while untreated VSMCs (SMC-) remained without green fluorescent signals (Fig. 104).

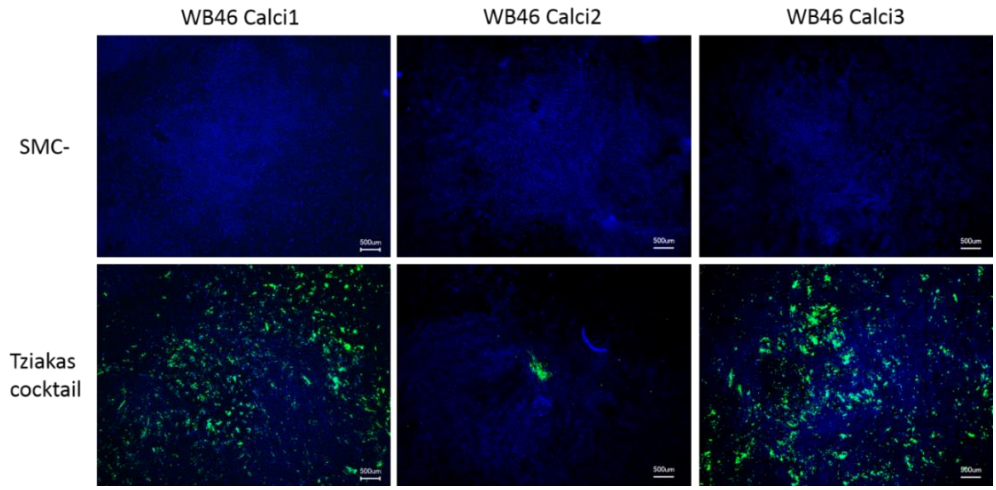

FIGURE 104: Calcein staining of R KO clone WB46
Untreated cells (SMC-) did not show any CaP deposition, while treated cells (Tziakas cocktail) displayed little to intermediate Calcein staining. Representative images per biological replicate are shown above. Scale Bars represent 500 µm.

NR KO cells displayed intermediate to strong Calcein staining in treated VSMCs, while untreated VSMCs did not display Calcein staining signals (Fig. 105).

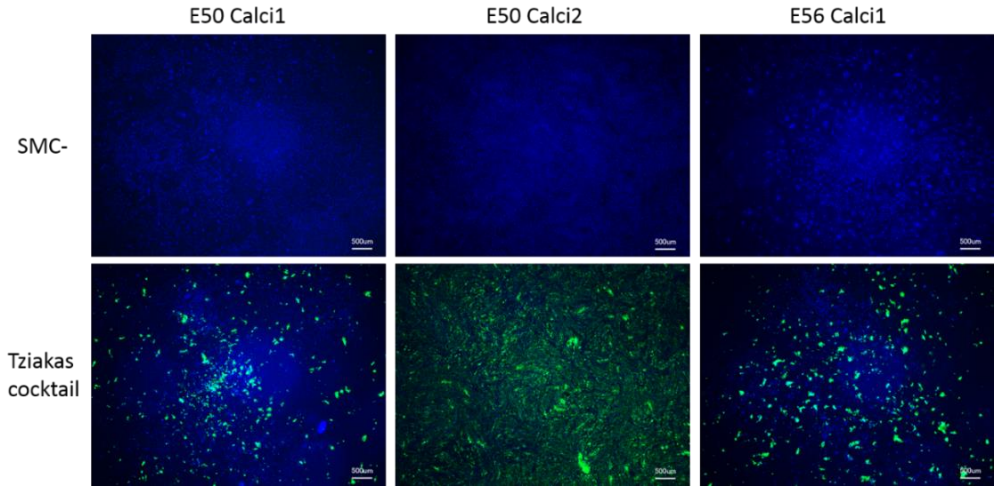

FIGURE 105: Calcein staining of the NR KO calcifying cells
Untreated cells (SMC-) did not show any CaP deposition, while treated cells (Tziakas cocktail) displayed little to intermediate Calcein staining. Representative images per biological replicate are shown above. Scale Bars represent 500 µm.

R KO and NR KO cells showed varying results in ARS and Calcein staining ranging from little to strong staining signals in between the biological replicates.

Further, we quantified the CaP depositions using the Calcein staining images and a Python script. Briefly, green staining from Calcein was related to the overall cell number estimated by DAPI staining (blue).

R KO cells of both clones, TAL1-9 and WB46, showed a significant increase in CaP depositions to around 10 to 15-fold in calcifying VSMCs compared to untreated VSMCs (Fig. 106).

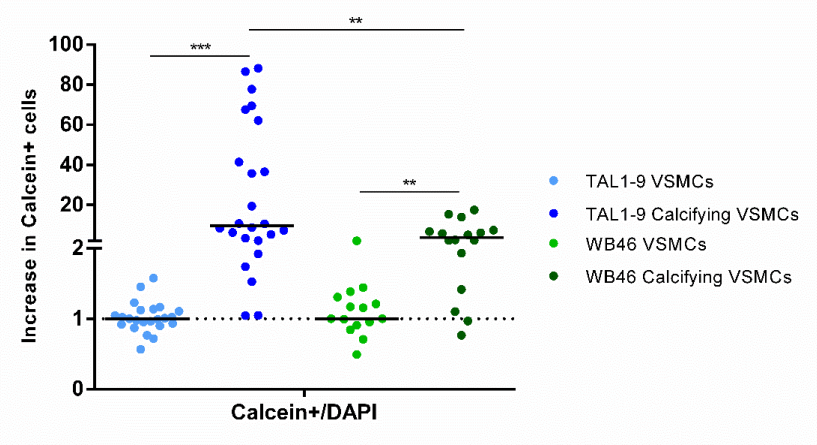

FIGURE 106: Calcium quantification in R KO cells via Calcein staining
Treated cells (calcifying VSMCs) showed a significant increase of around 10- to 15-fold in Calcein staining when compared to untreated cells (VSMCs) in both clones, TAL1-9 (blue) and WB46 (green). Dots represent value per image analyzed.

NR KO showed similar results for Calcein quantification. The clone E50 as well as the clone E56 showed significantly increased Calcein stainings to almost 10-fold (Fig. 107). No significant differences were detected between the calcifying cells of both clones.

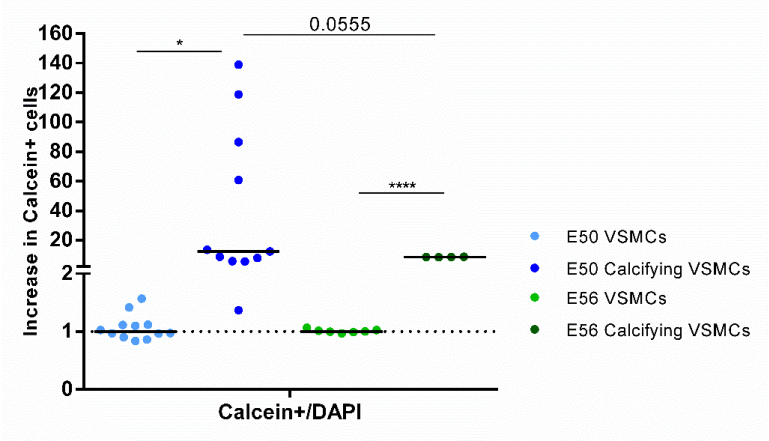

FIGURE 107: Calcium quantification in NR KO cells via Calcein quantification
Treated cells (calcifying VSMCs) of the E50 clone (blue) and the clone E56 (green) showed significantly increased Ca levels in Calcein staining to almost 10-fold. No significant differences were detected between the calcifying VSMCs of both clones. Dots represent value per image analyzed.

In order to compare the increase in Calcein staining, data of the clones of both cell lines were merged. R KO cells did not show significant differences in Calcein staining (Median: 5.1) compared to NR KO cells (Median: 8.6) (Fig. 108).

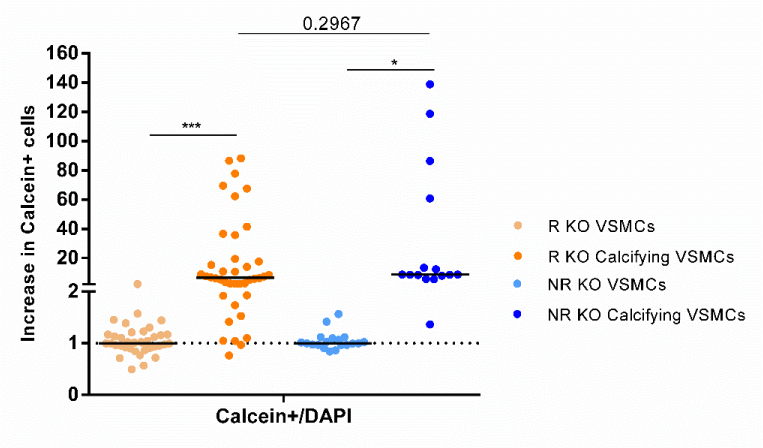

FIGURE 108: Comparison of calcium quantification between R KO and NR KO cells
R KO (orange, Median 5.1) cells and NR KO (blue, Median 8.6) do not show significant differences in the Calcein staining of Calcifying VSMCs. Dots represent value per image analyzed.

Following the macroscopical analyses we performed RNA-expression analyses to identify calcification-associated markers that were changed in calcifying VSMCs compared to untreated VSMCs in R KO as well as NR KO cells. For that we used the calcification markers *ALPL*, *CTSK*, *CSF1*, *RUNX2* and *OPN/SSP*.
For R KO cells the expression of *ALPL* was significantly increased in calcifying VSMCs in both clones up to 2-fold in TAL1-9 and over 4-fold in WB46 cells (Fig. 109).

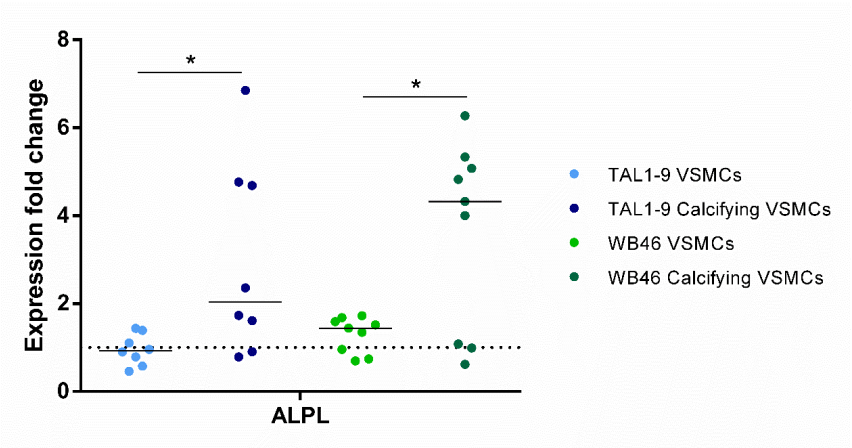

FIGURE 109: *ALPL* expression in R KO cells
R KO cells showed an increase in *ALPL* expression in calcifying VSMCs compared to untreated VSMCs in both clones. TAL1-9 (blue) showed a 2-fold expression fold change and WB46 (green) cells displayed an almost 4-fold increase. Each dot represents median of technical replicates.

The expression of *CTSK* was increased in the clone WB46 around 1.5-fold, but not in TAL1-9. However, the same tendency is visible in cells of the TAL1-9 clone (Fig. 110).

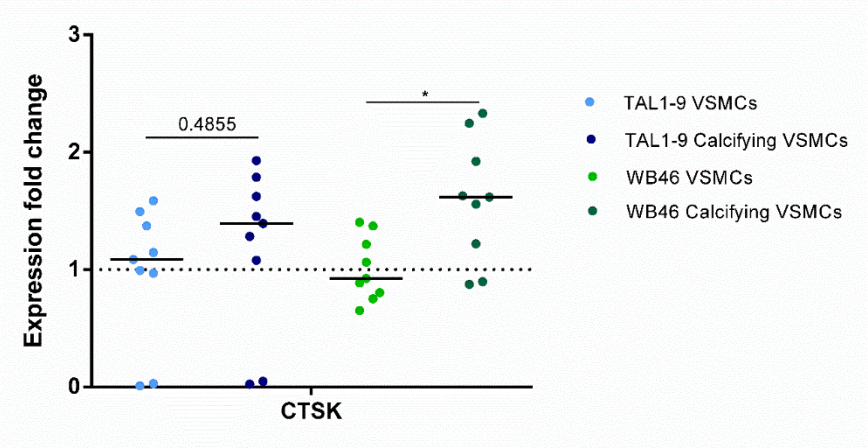

FIGURE 110: *CTSK* expression in R KO cells
R KO cells show an increase in *CTSK* expression in calcifying VSMCs compared to untreated VSMCs in WB46 (green) cells. Cells of the clone TAL1-9 (blue) do not show a significant difference. Each dot represents median of technical replicates.

CSF1 expression was significantly increased in calcifying cells of both R KO clones, between 4-fold in TAL1-9 and around 5-fold in WB46 cells (Fig. 111).

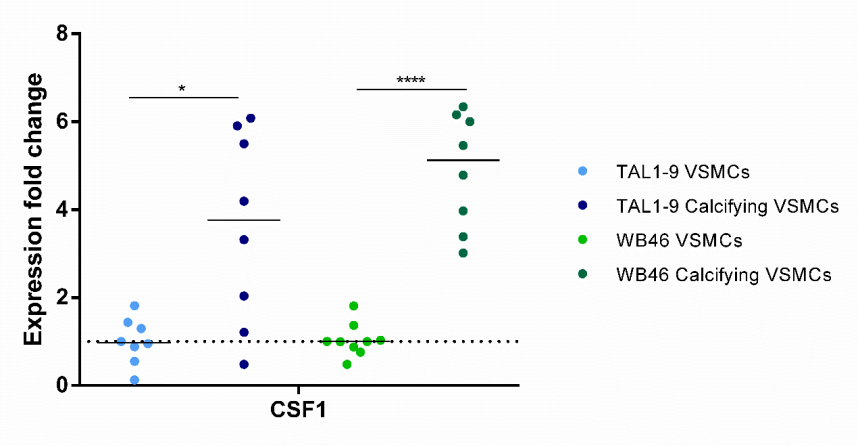

FIGURE 111: *CSF1* expression in R KO cells
R KO cells showed a significant increase in *CSF1* expression in calcifying VSMCs compared to untreated VSMCs in WB46 (green; 5-fold) cells and TAL1-9 (blue; 4-fold) cells. Each dot represents median of technical replicates.

The R KO clones TAL1-9 and WB46 showed a significant increase in the expression of *RUNX2* in calcifying cells compared to untreated VSMCs between 2.5 and 3-fold (Fig. 112).

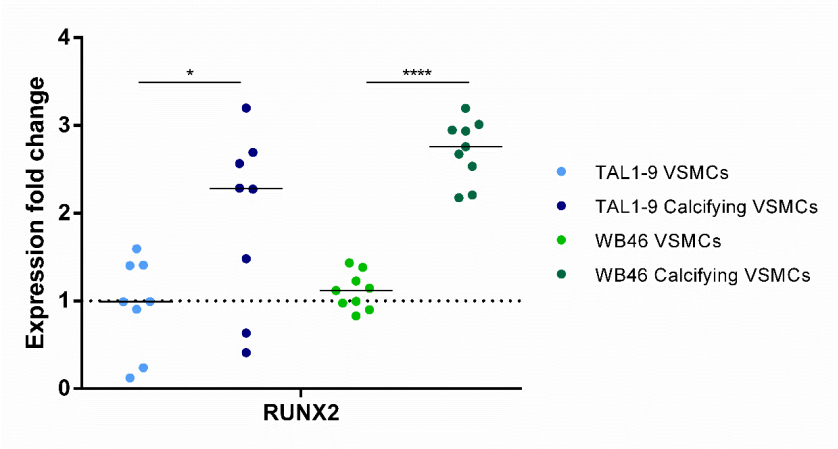

FIGURE 112: *RUNX2* expression in R KO cells
R KO cells showed a significant increase in *RUNX2* expression in calcifying VSMCs compared to untreated VSMCs in WB46 (green) cells and TAL1-9 (blue) cells of 2.5 to 3-fold. Each dot represents median of technical replicates.

Finally, the expression of *OPN/SSP* was analyzed in R KO cells. In cells of the clone TAL1-9 *OPN/SSP* was significantly upregulated approximately 8-fold in calcifying VSMCs (Fig. 113). In cells of the WB46 clone, RNA expression of *OPN/SSP* was significantly downregulated to around 0.5-fold in calcifying cells compared to VSMCs (Fig. 113).

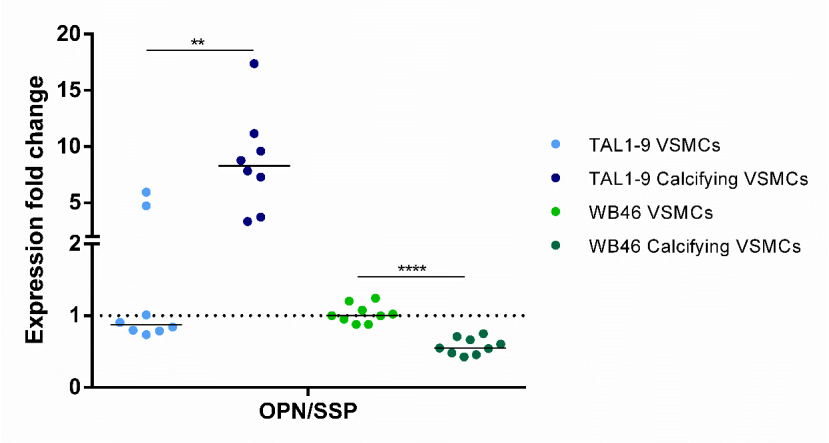

FIGURE 113: *OPN/SSP* expression in R KO cells
R KO cells of the TAL1-9 clones (blue) showed a significant increase in *OPN/SSP* expression of approximately 8-fold in calcifying VSMCs compared to untreated VSMCs. Cells of the WB46 clone showed a significant downregulation in *OPN/SSP* expression to around 0.5-fold. Each dot represents median of technical replicates.

Overall, the expression of most calcification-associated markers was increased in calcifying cells of the R KO genotype.

The same analyses were performed in NR KO cells. The expression of *ALPL* was not altered in both clones of the NR KO cells, E50 and E56 (Fig. 114).

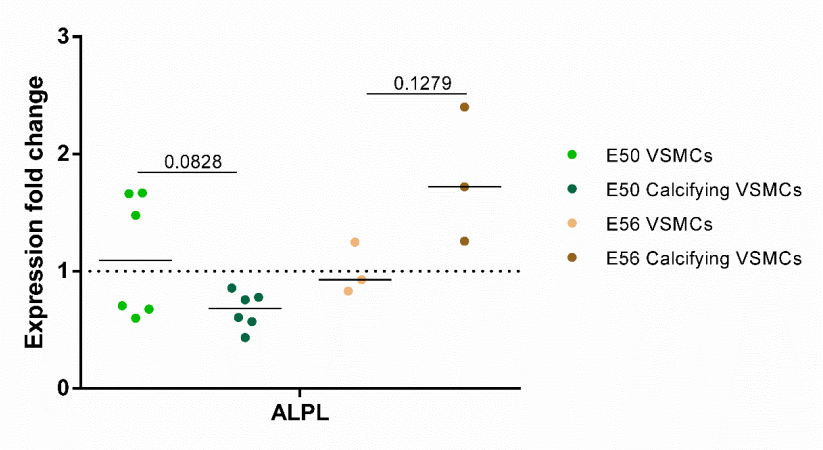

FIGURE 114: *ALPL* expression in NR KO cells
NR KO cells did not show changes in the expression of *ALPL* in calcifying cells compared to untreated VSMCs. Each dot represents median of technical replicates.

The expression of *CTSK* was unchanged in calcifying VSMCs of the NR KO clone E50 and displayed big variations (Fig. 115). Cells of the NR KO clone E56 showed a significant decrease in *CTSK* expression to zero in calcifying cells compared to VSMCs (Fig. 115).

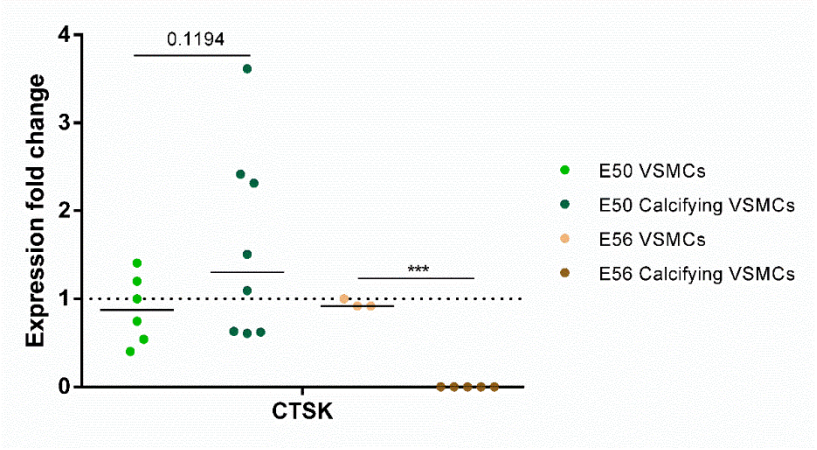

FIGURE 115: *CTSK* expression in NR KO cells
Cells of the NR KO clone E50 (green) did not show changes in expression of *CTSK*. Cells of the clone E56 (brown) showed a significant downregulation of *CTSK* expression to zero in calcifying cells compared to untreated VSMCs. Each dot represents median of technical replicates.

The *CSF1* expression was significantly upregulated in clone E50 to almost 7-fold, and unchanged in clone E56 in calcifying VSMCs (Fig. 116). However, in cells of the clone

E56 a tendency towards upregulation of the RNA expression of *CSF1* was visible (Fig. 116).

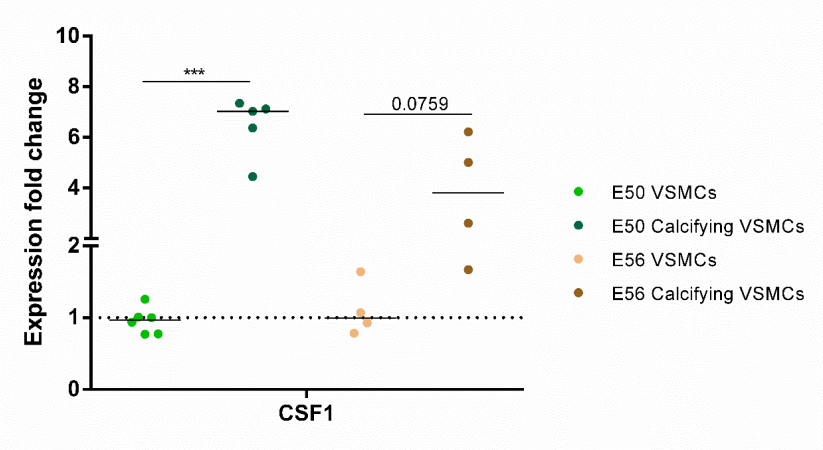

FIGURE 116: *CSF1* expression in NR KO cells
Cells of the NR KO clone E50 (green) showed a significant upregulation in expression of *CSF1* to around 7-fold. Cells of the clone E56 (brown) did not show significant changes of *CSF1* expression in calcifying cells compared to untreated VSMCs. Each dot represents median of technical replicates.

The expression of *RUNX2* as a late calcification marker was significantly increased in calcifying VSMCs both clones of the NR KO genotype. Cells of the clone E50 displayed an upregulation of approximately 2.5-fold, while E56 cells showed increased expression of almost 4-fold (Fig. 117).

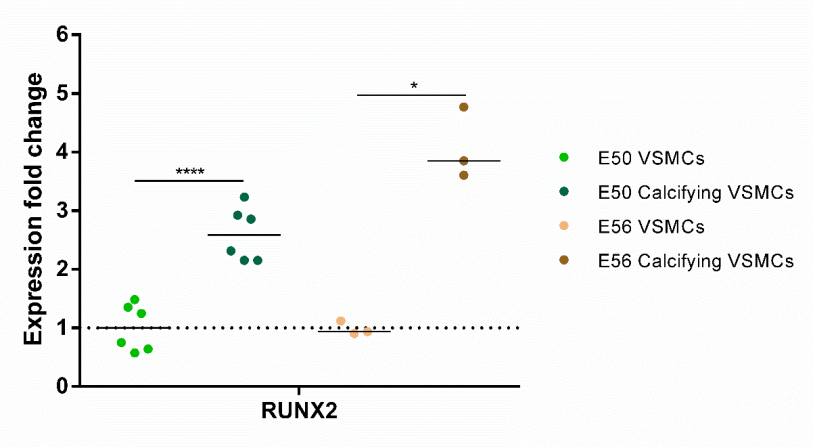

FIGURE 117: *RUNX2* expression in NR KO cells
Cells of the NR KO genotype showed a significant increase in the expression of *RUNX2*. E50 (green) cells showed a 2.5-fold increase, while E56 (brown) cells showed almost 4-fold increase. Each dot represents median of technical replicates.

Finally, *OPN/SSP* expression was not altered in the NR KO clone E50 (Fig. 118). In the clone E56 the expression of *OPN/SSP* was statistically significant changed by around 1.5-fold (Fig. 118).

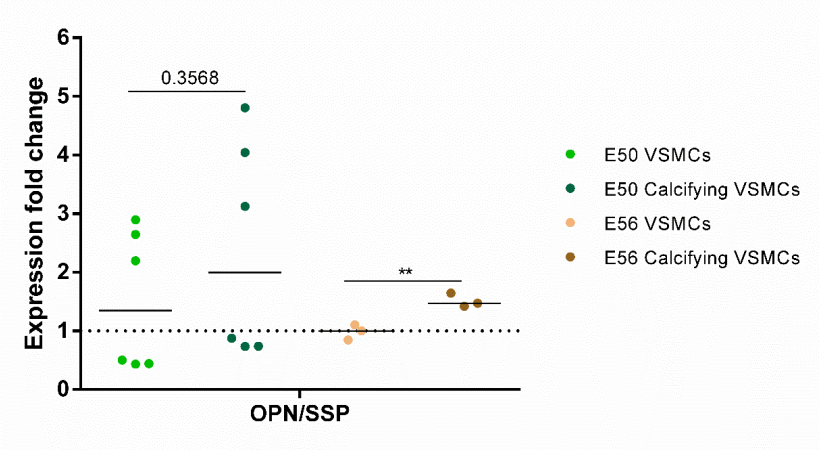

FIGURE 118: *OPN/SSP* expression in NR KO cells
Cells of the NR KO clone E50 (green) did not show changes in the expression of *OPN/SSP*. In the clone E56 (brown) the expression of *OPN/SSP* was significantly increased to 1.5-fold. Each dot represents median of technical replicates.

Altogether, cells of the NR KO genotype showed increased expression of early and intermediate stage calcification markers. Late-stage markers were variably expressed.

Finally, we aimed at analyzing protein expression of calcification markers in order to confirm the findings from RNA expression. However, we were not able to detect most of the proteins (data not shown). ALPL expression was detected, but no difference between the expression levels of ALPL between untreated and treated VSMCs could be seen (Fig.119). Cells from the R KO clone TAL1-9 calcifications 1 and 2 were used for the WB analysis, as the ARS and Calcein staining suggested that CaP depositions had taken place. Neither cells of the first nor the second calcification experiment showed a more prominent ALPL protein expression in calcified cells compared to untreated VSMCs (Fig. 119A). Quantification of the protein expression using ImageLab showed an ALPL protein expression that was located between 0.9 and 1.4 (Fig. 119).

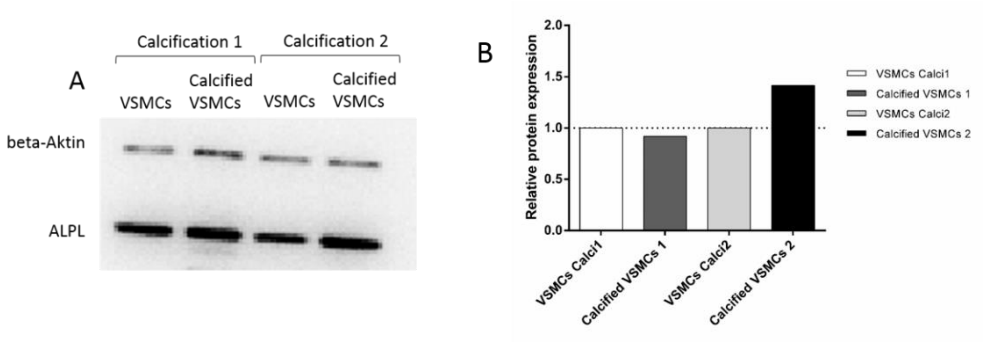

FIGURE 119: ALPL protein expression in Calcifications 1 and 2 of the R KO clone TAL1-9
A) Image of WB membrane showing beta-Actin and ALPL expression in two calcification experiments using the R KO clone TAL1-9.
B) Protein expression quantification shows no significant increase in the expression of ALPL in calcified VSMCs. Data are presented as bar diagrams in n=1 technical replicate each.

As the WB of ALPL shows, changes in the protein expression of calcification associated markers could not be quantified. We therefore decided to not perform WB for all calcifications.

Altogether, the results for calcification of 9p21 R and NR cells are highly variable. Overall, only around 39.5% of calcification approaches performed during this thesis were successful in terms of positive staining (Fig. 120). The highest number of successful calcifications was detected in R KO clones resulting in 67.5% positive calcifications (Fig. 120).

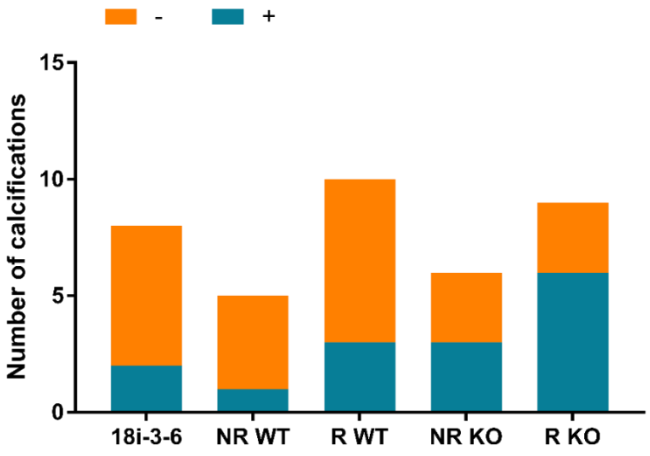

FIGURE 120: Overview of all Calcification approaches using the Tziakas cocktail
All calcification approaches using the Tziakas cocktail are shown above. Successful calcifications are displayed in green, unsuccessful in orange. R KO cells show the highest success rate with 67.5% of positive calcifications. Data are presented as stacked bar diagrams.

Concluding, R WT as well as R KO and NR KO cells showed cellular calcification in ARS and Calcein staining, Calcein quantification and RNA expression of calcification-associated. NR WT cells remained rather negative in ARS and Calcein staining, Calcein quantification, as well as RNA expression of calcification-associated markers.

4. Discussion

4.1 Establishing a differentiation protocol from iPSCs towards VSMCs

The establishment of differentiation protocols of iPSCs towards VSMCs was firstly carried out using the GM iPSC line, and subsequently the 18i-3-6 iPSC line. As described above the GM cell line was identified during the course of this work with a COL1A2 mutation that would influence the results on calcification, and the patient presents with a heart phenotype, too. Therefore, we stopped all experiments using this line at the point where we learned of the status of these cells.

However, the work performed with the GM cell line consumed a great part of the time, effort and materials that had gone into this thesis which lead us to the conclusion to include the data obtained with the GM cell line in this thesis. Further, the publication released in 2018 in Stem Cell Research (Trillhaase et al., 2018;) presented mainly data with the GM cell line. In 2020 we had to retract the publication, as the data were not reproducible with other cell lines, neither the 18i-3-6 nor the C512 or the HE463_7 cells (retracted 2020).

We examined two independent differentiation protocols leading from iPSCs to iPSC-derived VSMCs. An undirected, short protocol formerly published by Xie and colleagues (Xie et al., 2009) and a lineage-directed protocol published by Cheung et al (Cheung et al., 2014). Both protocols proved sufficient to result in VSMCs. However, we decided to use the directed, lineage-specific protocol published by Cheung et al., as we decided it would be more convenient to use a protocol that follows paths of the embryonic development in order to generate one specific subgroup of VSMCs. Anyhow, we saw the need to modify the original differentiation protocol published by Cheung and colleagues in 2014 (Cheung et al., 2014) in order to reduce cell death and increase the efficiency, such as increasing the cell density for replating on d5 and changing the complete medium instead of 50% during differentiation in order to wash out dead cells. We however noticed that modifications of the original protocol were donor-dependent, as not all cell lines required adaptations.

Nonetheless, we were able to establish a stable working differentiation protocol, resulting in >95% CNN1+ and TAGLN+ cells in IF staining, both markers that are

commonly used to characterize VSMCs identity and phenotype on molecular level (Cheung et al., 2014; Marchand et al., 2014), in addition to their morphology that is detected microscopically. Furthermore, we were able to show a reduction in RNA and protein expression of pluripotency-associated markers *NANOG*, *OCT4*, and *SOX2*. This reflects the progressing of differentiation, as pluripotency-associated genes are rapidly downregulated (or silenced) during the course of differentiation (Jaenisch and Young, 2008). Simultaneously, the commonly used SMC-specific markers *TAGLN*, and *CNN1*, as well as *CALD1* were upregulated on RNA level leading to the conclusion that VSMCs were generated from iPSCs, as those markers are highly expressed in VSMCs (Beamish et al., 2010; Cheung et al., 2014; Rensen et al., 2007). As there were issues with the identity of the GM iPSCs, we switched into 18i-3-6 iPSC-derived VSMCs for functional characterizations, and stopped further experiments with the GM cell line. The characterization of 18i-3-6 iPSC-derived VSMCs displayed a rather high migration rate of almost 43% (reflecting confluency in our case) within 24 h. Reported migration rates of healthy VSMCs usually range around 20% in rat aortic SMCs and 2% FBS containing medium (Feng et al., 2019). However, the data regarding migration rates of healthy human VSMCs and especially iPSC-derived VSMCs are rather poor if not non-existent, making it hard to find comparable values.

Further, 18i-3-6 iPSC-derived VSMCs showed a proliferation rate of around 20%. This proliferation rate is compatible to data in the literature, showing proliferation rates of different types of SMCs of up to 30%, depending on source and treatment (Riches et al., 2013). Especially, used matrices, SMC phenotype and growth factors highly impact the migratory and proliferative capacity. However, we must admit that very different methods for the analysis of cell proliferation are used in the literature and in this thesis. Further, there are almost no data on proliferation and migration of iPSC-derived VSMCs. Lo Sardo and colleagues did show results on proliferation of the 9p21 genome engineered cell lines used in this thesis (Lo Sardo et al., 2018). Nevertheless, the healthy “normal” proliferative state of iPSC-VSMCs is not commented on. Therefore, we can only rely on data for primary SMCs or animal models like mouse, porcine, rat or bovine, where we see a similar trend. Overall, we were able to generate iPSC-derived VSMCs of the lateral mesoderm, expressing important SMC markers and showing typical SMC morphology as well as SMC behavior.

4.2 Establishing a calcification protocol of iPSC-derived VSMCs *in vitro*

Vascular calcification is known as the deposition of CaP mineral in cardiovascular tissues like arteries and heart valves (Jono et al., 2000a). Pathological calcification goes hand in hand with the formation of atherosclerotic lesions (Aherrahrou and Schunkert, 2013). As primary vascular cells are hardly accessible and quickly lose their typical properties, thus less dynamic, the use of these cells for *in vitro* studies is limited (Alexander and Owens, 2012). The iPSC-technology enables such studies *in vitro* without putting patients at risk for the extraction of cells. Differentiation protocols of PSCs towards vascular cells have been published before (Cheung et al., 2014; Xie et al., 2009), but there are no protocols for the calcification of human iPSC-derived VSMCs *in vitro* until today.

To enhance calcification in iPSC-derived VSMCs, the differentiation protocol was extended with an additional calcification period, where cells were treated with several agents for different time periods. As described previously, various methods exist today to calcify or mineralize primary human, murine or bovine VSMCs such as supplementation with β-GP, L-AP or Pi (≥2 mM) (Byon et al., 2008; Tintut et al., 2003; Wada et al., 1999; Yang et al., 2004). All methods were shown before to lead to calcification *in vitro* in a concentration- as well as time-dependent manner.
For our study we initially used Pi and β-GP/L-AP supplemented media. We additionally examined whether the onset of calcification during or after the differentiation of iPSCs towards VSMCs would change the calcification outcome. Pi turned out to be inappropriate for most of our experiments, as massive cell death and detaching of cells appeared during the first days of calcification. Cells surviving the treatment either did not show positive ARS and Calcein staining or only very scarce. Expression analyses did not show changes in the expression of OPN, neither for Pi nor for β-GP/L-AP. Therefore, we considered these approaches as not sufficient to introduce calcification in iPSC-derived VSMCS. There are different factors that influence calcification *in vitro*. Firstly, often an unphysiologically high concentration of Pi is used for the induction of calcification *in vitro*. Pathological P concentrations range between 1.5 to 2 mM (Jono et al., 2000a, 2000b; Lanzer et al., 2014), whilst *in vitro* assays commonly apply 2.8 up to 4 mM Pi (Reynolds et al., 2004; Yang et al., 2004). Therefore, the used concentration

of 3.8 mM can of course act toxic on the cells leading to premature cell death, as we observed in our approach.

The combination of L-AP (0.28 mM) and β-GP (10 mM) was not able to enhance calcification either. Here maybe the concentration was too low, even though we adjusted the concentrations on data published before. In previous studies concentration between 5 mM up to 10 mM for β-GP and L-AP concentrations 0.25 mM or 50 µg/mL were usually applied for 7d up to 21d (Sun et al., 2012; Tintut et al., 2003; Tziakas et al., 2019; Zwergel et al., 2019).

In the beginning we also tested calcification in parallel and after differentiation of iPSCs towards VSMCs. When the calcification was started in parallel to the differentiation, maybe the stress and cell death during differentiation may have hindered successful calcification, even though the duration of 27d was long enough. In the case of starting the calcification after the differentiation was finished the calcification duration of 10d may have been too short especially for the combination of β-GP and L-AP to properly induce calcification. Calcification in a physiological setting is a very slow progress, speaking of decades. *In vitro* calcification models usually use durations of 7d up to 21d (Sun et al., 2012; Tintut et al., 2000; Tziakas et al., 2019; Zwergel et al., 2019), depending on the cell type and origin as well as the calcifying agents used. As L-AP and β-GP need to be metabolized by the cells in order to release CaP that can be excreted into the matrix some more time than 10d might be needed if no other components are added that enforce calcification. However, often other agents were added, such as H_2O_2, insulin, $CaCl_2$, or dexamethasone (Sun et al., 2012; Tziakas et al., 2019).

In the following approach, we used StemXVivo™ human Osteogenic Medium that uses β-GP as calcification agent and is free of serum, but also contains various growth factors. The group of Brady and colleagues showed that the application of StemXVivo™ Osteogenic medium on mesenchymal stem cells lead to osteogenic differentiation of the cells after 14d, as detected by e.g. ARS staining (Brady et al., 2014). Generally, staining like von Kossa or ARS are commonly used to initially demonstrate calcification (Jono et al., 2000b; Reynolds et al., 2004; Wada et al., 1999). In order to verify successful calcifications in our experiments we used similar standard methods, including Alizarin Red S and Calcein staining, calcium quantification and osteogenic

marker gene expression analyses. Using the GM cell line, we were able to show concurrent results as obtained with primary human, bovine or murine cells, such as increased calcium depositions in stainings and quantification, as well as upregulation of calcification-associated gene and protein expressions after 30d ((Trillhaase et al., 2018); retracted 2020). However, transferring the same protocol to the other iPSC donor lines did not result in positive calcification, or cells did not survive the course of treatment due to cell death or detachment of cells.

A theory we developed in this context was that the mutation in the COL1A2 that is present in the GM cell line leads to increased ALPL expression. ALPL is an important mediator in the process of calcification as it activates the expression of extracellular matrix proteins and promotes CaP deposition (Byon et al., 2008; Vasuri et al., 2014). Further, it was shown that the inhibition of the COL1A2 in SMCs contributes to the destabilization of atherosclerotic plaques (Liu et al., 2015). They also assumed that the demethylation of the ALPL promoter could lead to increased calcification (Liu et al., 2015). Additionally, the group of Azechi et al. stated that osteoblastic differentiation of mesenchymal stem cells would be promoted by DNMT inhibitors probably via the upregulation of osteogenic gene expression (Azechi et al., 2014). They showed that the inhibition of DNMT1 in HASMCs lead to an increased expression of ALPL and other calcification associated markers (Azechi et al., 2014). However, the inhibition of DNMT1 did not show an effect on the expression of commonly used osteogenic genes RUNX2 and OPN (Azechi et al., 2014). Concluding, the group of Azechi and colleagues reported an increase in Ca levels in DNMT1 inhibited HASMCs under high phosphorus concentrations (Azechi et al., 2014). Another study confirmed that COL1A2 is an important factor expressed during early osteogenic differentiation, while ALPL is rather expressed in intermediate-stage calcification (Zwergel et al., 2019). Indeed, we were able to show that GM iPSCs show an increased expression of ALPL and DNMT1 in VSMCs compared to 18i-3-6 VSMCs, whilst COL1A2 was significantly decreased in its expression (Appendix B). However, we were not able to confirm this relation in calcification of VSMCs, as the final calcification protocol used for the analyses of the effect of 9p21 on calcification was not examined in GM cells. A good alternative to random testing of various genes influencing calcification in the vascular system could be to perform RNA sequencing analyses in order to identify differently regulated pathways in the GM cells compared to 18i-3-6 cells, as well as in between the 9p21 R

and NR cells. Further, it would make sense to perform single cell sequencing of the iPSC-derived VSMCs in order to identify different VSMC subtypes that might exist after the differentiation of cells of different genotypes.

Anyhow, we needed to find a calcification protocol that was stably working not only for the 18i-3-6, but also for our target 9p21 in the respective R and NR cell lines. Therefore, we started investigating the applicability of various other protocols published previously, in our 18i-3-6 as well as the 9p21 R and NR cells. The first attempt we made was to supplement the StemXVivo™ Osteogenic Medium with 20 ng/mL TNFα, as TNFα was described as promoting calcification *in vitro* before (Tintut et al., 2000). However, we were not successful in applying this method stably on our iPSC-derived VSMCs resulting in an efficiency of below 20% (data not shown). Again, we observed massive detachment of cells, maybe due to the high proliferation rate of the R cells that was further intensified by the growth factors incorporated in the medium. In the rest of the approaches we observed very unstable results within one biological replicate. This and the low success rate initiated the screening for other calcification protocols.

Next, we examined the application of H_2O_2 (0.4 mM) with 20 ng/mL TNFα and/or 200 ng/mL BMP2 on either SMC-maintenance medium or StemXVivo™ Osteogenic Medium. This approach was based on the findings that oxidative stress caused by 0.4 mM H_2O_2 induces calcification in mice aortic VSMCs *in vitro* (Byon et al., 2008), combined with publications proving the effect of BMP2 and TNFα have on vascular calcification (Balderman et al., 2012; Byon et al., 2008). Unfortunately, none of the approaches resulted in positive calcification, neither in SMC-maintenance medium nor in StemXVivo™ Osteogenic Medium. We mainly observed massive cell death especially in VSMCs treated with H_2O_2 after 5-6d already. This is one of the reasons why the experiment was stopped after 6d. For BMP2 and TNFα supplementation we saw mainly negative stainings in ARS and Calcein after 6d independent of the medium that was used. Either, the time was too short for the inductors to be metabolized and successfully induce the calcification cascade in the cells, or both of the inductors are not adequate to solely induce calcification in iPSC-derived VSMCs.

Hereafter, we applied a calcification cocktail published by Alves and colleagues in 2014 that consists of 1.8 mM $CaCl_2$, 20 mM HEPES, 0.1 mM L-AP, 10 mM β-GP, and

100 nM dexamethasone (Alves et al., 2014) in SMC medium. However, again our calcification approaches of two independent iPSC lines remained negative after 9d of treatment. Originally, Alves and colleagues applied this protocol to human bone-marrow derived mesenchymal stem cells and human coronary artery VSMCs and took samples after 1, 2, and 3 weeks (Alves et al., 2014). Therefore, we considered 9d a suitable time where we should be able to see calcifications in iPSC-derived VSMCs. Unfortunately, this was not the case. All approaches remained negative, but an extension of the incubation time was not possible due to detachment of the R WT cells in particular. Further critical factors influencing the success of calcification are the capacity to metabolize the given substances into hydroxyapatite, Ca and P that can be secreted and then form mineralization (Jono et al., 2000b; Vasuri et al., 2014). Most importantly, an intact ECM is necessary for calcification, as calcifying products are secreted into the ECM (Alam et al., 2009; Amann, 2008; Balderman et al., 2012; Byon et al., 2008; Tintut et al., 2003). A high content of ECM is mainly secreted by synthetic VSMCs or VSMCs undergoing osteoblastic differentiation (Amann, 2008; Beamish et al., 2010). Therefore, analyses concerning the SMC phenotype as well as RNA sequencing will help to identify the underlying cell type and metabolic processes occurring during calcification, and may help to understand why the abovementioned calcification protocols were not successful. We therefore went on to look for another calcification protocol.

Finally, we applied the calcification cocktail published by Tziakas et al. to our cells. Briefly, the cocktail consists of 4 mM $CaCl_2$, 5 mM β-GP, 50 µg/mL L-AP, 1 mM insulin, and 0.1 µM dexamethasone (Tziakas et al., 2019) in SMC medium. Tziakas and his colleagues applied this cocktail to human and murine arterial smooth muscle cells for around 7d (Tziakas et al., 2019). We therefore decided that in our case 7d should be enough to see calcifications as well. Indeed, we had a positive staining result in both our independent test cell lines as confirmed by ARS and Calcein staining. Additionally, we performed an RT^2 Profiler Array for the expression analysis of osteogenic differentiation markers in 18i-3-6 cells from the test session, to identify markers that were differentially expressed between iPSC-derived VSMCs and calcifying VSMCs in order to enable molecular analyses in the R and NR cells. The Profiler Array revealed the upregulation of calcification associated markers *CTSK*, *CSF1*, *RUNX2* and *DLX5*,

whilst *ALPL* was downregulated. This reflected the assumption that calcification was initiated on molecular level, as *CTSK*, *CSF1*, *RUNX2* and *DLX5* are well known calcification markers (Balderman et al., 2012; Byon et al., 2008; Giachelli, 2009). *ALPL*, another well-known calcification marker however was downregulated. This could be the case because ALPL is expressed in the very early stages of osteogenesis and gets quickly downregulated after calcification is induced (Byon et al., 2008). We further added *OPN/SSP* to this screening panel for RNA expression, as it is another typical marker that is used for calcification (Giachelli, 2009; Vasuri et al., 2014). Due to these positive results in two independent test cell lines we decided to continue all calcification experiments with this approach and the calcification associated markers mentioned above generated by the profiler array.

In the following acquisition of results and therefore replications of the initial approach the 18i-3-6 cell line however showed rather negative calcification in ARS and Calcein staining, even though some replicates showed positive results. Further, no significant increase in Calcein staining was detected. However, the molecular regulation showed mainly increased expression of calcification associated markers. Intermediate and late stage calcification markers *CTSK*, *CSF1*, and *RUNX2* showed a significant upregulation in calcifying VSMCs. The early stage calcification marker *ALPL* as well as terminal marker *OPN/SSP* however did not show a significantly changed expression in calcifying VSMCs compared to untreated VSMCs. Therefore, on molecular level calcifying processes seemed to progress, even though we were not able to macroscopically detect CaP deposits in calcifying VSMCs of the 18i-3-6 line. Another option to identify CaP deposits on cellular level would be the use of electron microscopy that would pick up very small amounts of calcification.

4.3 Differentiation and calcification of 9p21 NR WT and R WT cells

Following the differentiation protocol we had established at our Institute, we performed differentiations of 9p21 NR WT and R WT cells. As described before we closely monitored the iPSC status as well as the VSMC status according to cell morphology, RNA expression and protein expression as well as protein localization.

NR WT and R WT iPSCs showed the cobblestone-like morphology with big nuclei and small cytoplasm that is typical for iPSCs and closely resembles ESC morphology

(Takahashi et al., 2007). As expected, we were not able to detect any differences in the morphology based on the absence or presence of the risk variant in the 9p21 locus, as the 9p21 locus influences disease-specific cell types, but not stem cells. The same results were also reported in a recent publication by Lo Sardo and coworkers (Lo Sardo et al., 2018).

Comparable results were obtained for the iPSC-derived VSMCs of cells of both genotypes. They appeared as star- or stellate shaped, with a lot of cytoplasm that contains contractile fibers (Alexander and Owens, 2012; Beamish et al., 2010; Rensen et al., 2007; Sinha et al., 2014). To further validate the cell identity, we performed IF staining of either NANOG as a pluripotency-associated marker, or TAGLN and CNN1 as VSMC-specific markers. NANOG in all cases was located in the nucleus of the iPSCs, where it is expected to be located as it is a transcription factor that can be discovered in 8-cell stage embryos and is necessary for the maintenance of pluripotency *in vitro* (Hanna et al., 2010). However, we did not find NANOG expression in iPSC-derived VSMCs (data not shown), as pluripotency markers get silenced quickly during differentiation (Ramirez et al., 2011; Takahashi et al., 2007; Thomson et al., 2011). Depending on the differentiation into the respective germinal layers, loss of gene expression of pluripotency-associated markers happens between d1 (OCT4) up to d6-9 (NANOG) after differentiation initiation (Ramirez et al., 2011; Takahashi et al., 2007; Thomson et al., 2011). Further, we were not able to detect differences in the intensity or the localization of NANOG in iPSCs of the NR WT and the R WT. As VSMCs markers we used TAGLN and CNN1. Expectedly, both proteins were located in the contractile fibers and the cytoplasm of the iPSC-derived VSMCs of both genotypes, and were colocalized to a large extend, as reported before (Cheung et al., 2014; Dash et al., 2016; Sinha et al., 2014).

Finally, we examined the RNA expression of the pluripotency-associated markers *NANOG*, *OCT4*, and *SOX2* as well as the VSMC-specific markers *TAGLN*, *CNN1*, and *CALD1* in iPSCs and iPSC-derived VSMCs. The expression of the pluripotency-associated markers was significantly downregulated in iPSC-derived VSMCs compared to iPSCs in cells of the R WT as well as the NR WT cells. Additionally, we were not able to detect significant differences between cells of the R WT and the NR WT lines. VSMC-specific markers however were significantly upregulated in iPSC-derived VSMCs compared to iPSCs in both the R WT and the NR WT cells. Again, we

did not see any significant differences between R WT and NR WT cells. As stated before, the RNA expression was examined on cell-type specific markers. Therefore, it is common sense, that pluripotency-associated markers are highly expressed in pluripotent stem cells whilst VSMC-specific markers are highly expressed in their respective cell type. During differentiation pluripotency-associated markers get silenced depending on the germ layer at different time points between d1 and d9 of differentiation (Ramirez et al., 2011; Takahashi et al., 2007; Thomson et al., 2011).

Concluding, the morphology, RNA expression and protein localization are corresponding for their respective cell type and therefore the lineage-specific differentiation of iPSCs into LM-derived VSMCs can be considered successful. Of course the identification of the SMC phenotype or SMC sub species is not possible using only these three markers. The most convenient methods for distinguishing sub species or phenotypes would be RNA sequencing and/or metabolic analyses of the cells that indeed differ between cell types. In protein expression however, we were not always able to detect a significant increase in the expression of TAGLN in iPSC-derived VSMCs, though a tendency was always visible. This could be due to immaturity of the harvested VSMCs that were used for the protein expression analysis, or the insensitivity of the detection method. Alternatively, more sensitive methods like IF staining with quantification or ELISA arrays could be used. However, we could show in all cells that OCT4 was significantly downregulated on protein level in iPSC-derived VSMCs compared to iPSCs of the R WT and the NR WT cell line. Looking at the differentiation efficiency based on TAGLN and CNN1 staining we were able to show that we reached a differentiation efficiency of above 95% in all approaches analyzed without a significant difference between cells of the 9p21 R WT and the NR WT genotype.

Finally, we can state that the establishment of the differentiation protocol was successful at our Institute, and the efficiency was equal for cells of the R WT and the NR WT, and even higher than reported previously (Cheung et al., 2014). There were no significant differences in the cell type identity of iPSCs or iPSC-derived VSMCs of the R WT or the NR WT. Therefore, we can conclude that the 9p21 risk locus does not have an effect on the cell identity or the differentiation efficiency. This basically reflects results with the same cells previously published by Lo Sardo and colleagues (Lo Sardo et al., 2018).

Following the cell characterization on cellular and molecular level, we also wanted to know if the 9p21 risk locus has an influence on the behavior of iPSC-derived VSMCs. We therefore analyzed the proliferation and migration rate. For the analysis of the proliferation rate, we used IF staining of the proliferation marker Ki67. We here observed an increased proliferation rate in R WT cells compared to NR WT cells. The data published by Lo Sardo et al showed the same differences in proliferation between the R WT and the NR WT cells (Lo Sardo et al., 2018). For the migration rate, we were able to show that R WT cells presented with a much higher migration rate than NR WT cells. These parameters however were not analyzed in the study of Lo Sardo et al. The authors of the paper generally state that various cell characteristics, like proliferation or adhesion, in the iPSC-derived VSMCs containing the R locus are significantly changed compared to the healthy (NR) cells (Lo Sardo et al., 2018), what confirms the observations we made using the same cell lines. We can therefore state that we were able to verify the influence of the 9p21 risk locus has on VSMC characteristics.

Still our main aim was to investigate vascular calcification, and to examine what influence the 9p21 risk locus has on this pathological process. We applied the calcification protocol previously published by Tziakas et al. 2019 as described above. Cells containing the 9p21 R locus showed positive ARS and Calcein staining ranging from low to intermediate intensities. NR WT cells on the other hand did not show any positive stainings, suggesting that no detectable calcification took place. Calcein quantifications showed a significant increase in the CaP depositions in R WT but not in NR WT cells. Accordingly, we detected a significant difference in the deposition of CaP in calcifying VSMCs of the 9p21 R WT compared to NR WT cells. This already led to the presumption that the 9p21 risk locus increases the CaP depositions in iPSC-derived VSMCs. Molecular analyses on RNA level using the well-known calcification markers *ALPL*, *CTSK*, *CFS1*, *RUNX2*, as well as *OPN/SSP* (Alves et al., 2014; Doherty et al., 2003; Lutgens et al., 2007; Tziakas et al., 2019; Wada et al., 1999) revealed rather inconsistent calcification outcomes. First of all, we noticed that Ct values in qPCR results were comparatively high (28-33), whilst β-Actin showed normal Ct values (~17). This was an obstacle that impeded the analysis of the data. Another problem was that expression data and the direction of molecular regulation was significantly different even between the biological replicates and/or clones of the same genotype. For the R WT cells for example we saw a significant increase in the RNA expression

of most of the calcification markers in one clone, while the other two clones showed a decreased expression or no significant difference in the RNA expression of calcification-associated markers in calcifying VSMCs compared to untreated VSMCs. Overall, the expression of calcification-associated markers was indifferent or rather increased in R WT calcifying cells compared to VSMCs. NR WT cells on the other hand showed a decrease in the RNA expression of calcification associated markers in calcifying cells compared to VSMCs. This, again points toward an elevated deposition of CaP and true calcifying events in R WT cells. NR WT cells on the other hand did not calcify, as expected from the results seen in behavioral analyses of the VSMCs (Lo Sardo et al., 2018).

The challenges we observed with the calcification experiments can have different reasons. One reason could be that the cells, due to their different proliferative and migratory behavior would also metabolize calcifying agents such as $CaCl_2$, Pi, β-GP or L-AP differently. Further, the cell density is a crucial factor for the success of *in vitro* calcification. Already in 1995 it was shown that post-confluently cultured cells showed signs of calcification after the treatment with β-GP (McQuillan et al., 1995). Mainly the collagen scaffold produced by those cells mineralized showing crystal formation (McQuillan et al., 1995). As NR WT cells have a much lower proliferation rate, it took them longer to reach the same confluency and to produce the needed ECM, as the R WT cells did. We tried to compensate that by seeding different cell numbers. However, we observed much more apoptosis and a decrease in cell number in the NR WT cells. Further, the high proliferation rate in R WT cells often led to a detachment of cells, before the treatment period with calcifying agents was finished. A reason for that could also be the coating we used for the calcification. Different proteins in the coating may have varying effects on SMC phenotype and therefore on calcification (Alves et al., 2014; Beamish et al., 2010). However, in one test where we applied different coatings, we observed massive cell death and no differences in calcification outcome (data not shown). Whether the negative calcification outcome resulted from the applied calcification protocol or the changes in coating we cannot say. Clearly, we saw no improvement depending on the coating we used for all calcification experiments. However, usually no coating is used in calcification studies using human or animal cells (Alves et al., 2014; McQuillan et al., 1995; Proudfoot et al., 2000; Reynolds et al., 2004; Tziakas et al., 2019). As the differentiation and VSMC maintenance was performed on

0.1% gelatin-coated plates and flasks, and cells behaved normal, we did not intend to change or skip coating for experiments. For future experiments it should be taken into consideration to apply other or no coating at all for examining iPSC-derived VSMCs or for performing calcification experiments.

Additionally, as mentioned above, we saw quite some variation in between, as well as within the biological replicates. One reason here could be that both, the SMC and the calcification medium, were based on FBS. Serum however has been shown before to lead to very uneven distribution of calcifying events and to inhibit VSMC calcification probably due to fetuin-A (Reynolds et al., 2004). Fetuin-A is produced in the liver and is suggested to inhibit CaP precipitation by specifically binding the minerals in cells (Reynolds et al., 2004). Fetuin-A has anti-inflammatory effects and generally reduces the inflammatory response (Jahnen-Dechent Willi et al., 2011). Further, it was shown to inhibit *de novo* apatite formation as well as binding CaP and Ca carbonate with very high affinities (Jahnen-Dechent Willi et al., 2011). *In vitro* experiments in rat osteoblastic cells and VSMCs have shown previously that cellular calcification was inhibited in the presence of fetuin-A under calcifying stimuli like β-GP and L-AP (Jahnen-Dechent Willi et al., 2011). The suggested mechanism here is that fetuin-A accumulates in intracellular vesicles that are then secreted from the cells. Due to the accumulation of fetuin-A within the vesicles there is no possibility CaP can precipitate (Jahnen-Dechent Willi et al., 2011). Therefore, CaP cannot form and precipitate in the ECM in the presence of fetuin-A and consequently, serum. Thus, it would be desirable to eliminate fetuin-A and therefore serum from SMC, and especially calcification medium, in order to increase the efficiency of the calcification protocol. Further, another impediment could be that we did not screen for the SMC phenotype. As explained in the introduction SMCs are quite flexible in their phenotype, meaning they can change from synthetic to contractile SMCs and back (Alexander and Owens, 2012; Beamish et al., 2010). Probably, one of the phenotypes is more prone to calcification. Therefore, a screening panel, including various markers (and not only three as described here) for either of the phenotypes should be established in our Institute to be able to discriminate between SMC phenotypes which can contribute to a higher efficiency in calcification. Another question that needs to be answered is if the iPSC-derived VSMCs rather resemble aortic or coronary artery properties which would explain their amenability to calcify. As we focused on lateral mesoderm-derived VSMCs that mainly

make up the coronary arteries (Ayoubi et al., 2017) we would expect them to resemble a profile similar to human coronary artery SMCs. Further, other characteristics like contractility and adhesion should be examined as they give further evidence for the existing phenotype. Therefore, it could be analyzed if differentiations of 9p21 R WT and NR WT iPS cells result in VSMCs of different phenotypes, that would then also be an explanation of why R WT cells calcify and NR WT cells do not.
Concluding we can state that SNPs in the 9p21 locus lead to an increased risk of vascular calcification.

4.4 Differentiation and calcification of 9p21 NR KO and R KO cells

Once more, following the differentiation protocol we have established at our Institute, we differentiated KO cells of the 9p21 R and NR donor towards lateral-mesoderm derived VSMCs. We performed the same analyses as for the WT cells of the respective donors as described above. For iPSC status as well as VSMC status we were not able to detect significant differences in cell appearance or protein localization in the respective cell types of the R KO and NR KO cells.
We also examined the migration rate of iPSC-derived VSMCs of the 9p21 R KO and NR KO cells as described before. We did not observe significant differences in the migration rate of R KO and NR KO cells. Unexpectedly, for proliferation on the other hand we detected a significantly higher proliferation rate in R KO cells compared to NR KO cells. These results for proliferation differ from the findings published by Lo Sardo and colleagues. They stated that KO cells would have a restored function comparable to that of the NR WT cells (Lo Sardo et al., 2018). However, the group of Lo Sardo et al., solely used the number of passages performed for a particular cell line in a given time as measurement for proliferation rate (Lo Sardo et al., 2018). We on the other hand determined the proliferation rate by specific staining of proliferating cells related to the overall cell number. Technical issues of both protocols can lead to the differences we observed. The method used by Lo Sardo and colleagues is highly dependent on the cell confluency upon seeding as well as differences in the medium exchange scheme. Higher cell confluencies at seeding as well as differences in cell

death that occurs due to stress during passaging leads to a variation in the recovery time of the cells and the following proliferation rate. Our method on the other hand depends on the confluency seeded for staining as well, as a low confluency increases apoptosis, while a high confluency leads to hyperproliferative cell clusters that can hardly be counted.

However, the migration rates were quite similar, which proves the overall assumption of the publication from Lo Sardo that the 9p21 KO cells were indifferent between the R and the NR donor, and functions were, in our case at least in some parameters, restored to almost normal function (Lo Sardo et al., 2018). Furthermore, we must admit that proliferation was not inhibited during migration experiments. Therefore, we cannot exclude that higher migration rates were partly superposed by proliferation, especially in R WT cells that show higher proliferation rates as well. But, as published before differences in cell properties like migration, proliferation and adhesion may contribute to the onset and development of the disease (Lo Sardo et al., 2018).

Subsequently, we also performed calcifications of the 9p21 R KO and NR KO cells using the calcification cocktail published by Tziakas et al. Cells of both genotypes showed positive calcifications in ARS and calcein stainings ranging between intermediate to strong staining. As described earlier for the WT cells we saw strong variability within and in between the biological replicates independent of the R or NR donor. Calcein quantification showed a significant increase in the CaP deposits in calcifying cells of both genotypes. Statistically, we also saw a significant difference between calcifying cells of the R and the NR donor that might be due to different genetic background between the two donors.

Overall, we saw mostly an upregulation in RNA expression of the analyzed markers in calcified VSMCs compared to VSMCs of the R KO as well as the NR KO cells. However, as described for the WT cells we again observed large variations and even contradictory results for cells of the same genotype. The reasons for that can be numerous. As explained above, most likely the cell density as well as the utilization of serum containing fetuin-A leads to those inconsistencies (Jahnen-Dechent Willi et al., 2011; Reynolds et al., 2004).

As the data for calcification associated markers in the 9p21 R and NR cell lines were inconsistent we did not perform analyses of the relation of ALPL, COL1A2, and DNMT1 in these cells.

Concluding, we were able to report that R KO and NR KO cells did calcify and displayed parameters that were alike. However, we expected the KO cells to behave similar to what was published before for their differentiation namely that they would show patterns more similar to the NR WT cells. Nevertheless, the patterns and expression data observed rather resembles the data obtained for the R WT than the NR WT.

We can therefore come to the conclusion that risk variants within or the loss of the 9p21 risk region seemingly increases the likelihood for calcifications in VSMCs. Patients containing a risk variant would therefore be of higher risk to suffer from CAC than patients without variants in this risk region. Until today, it remains unclear what the mechanism could be that leads to the effect of increased risk of CAC in carriers of the risk variant. For the effect on atherosclerosis and thus on CAD there is evidence that the different isoforms of the ANRIL are responsible for the increased risk. It is known that ANRIL, as most long noncoding RNAs works via RNA-RNA, RNA-DNA, or RNA-protein interaction (Holdt and Teupser, 2012). More recent studies showed that different isoforms of the ANRIL exist, that can be roughly divided into circular (circANRIL) and linear ANRIL (linANRIL) isoforms. Holdt and colleagues showed that patients with a high content of circANRIL had less CAD (Holdt et al., 2016). Therefore, circANRIL isoforms seem to be protective for CAD. On a cellular level it was shown that a high circANRIL content increased apoptosis and decreased proliferation which are very important factors in the development of CAD. They described circANRIL as a “physiologically relevant modulator of apoptosis and proliferative capacity” (Holdt et al., 2016). However, they stated that the function of ANRIL is independent of the close-by encoded cell cycle regulators CDKN2A/B (Holdt et al., 2016). It therefore seems plausible that the ratio of circANRIL to linANRIL and their physiological function also has a great impact on the development of CAC and therefore the vascular calcification. On the other hand, as mentioned before, important cell cycle regulators like CDKN2A and B are encoded close to the risk region. It is likely that the variants in the risk region might change regulatory processes that directly influence the transcription or activity of genes in close proximity. A change in the cell cycle regulation might influence the proliferative capacity that then in turn has effects on disease onset and progression. Future studies are required to mechanistically highlight the underlying mechanisms involving the 9p21 locus in CAC.

Concluding, we report the successful establishment of a protocol for the differentiation of LM-derived VSMCs from iPSCs of three independent donor cell lines after introduction of slight changes ((Trillhaase et al., 2018); retracted 2020). We provided evidence that neither the absence nor the presence of the 9p21 risk locus or SNPs within this risk locus influence iPSC or VSMC cell identity as well as differentiation efficiency. Differences in cell characteristics like proliferation or migration however can be assigned to genotype as described before (Lo Sardo et al., 2018). For calcification we applied the protocol that after our analyses worked the most reliable. However, the protocol is not very stable and should be improved for further research on this topic. Nevertheless, it is the first calcification protocol applied to iPSC-derived VSMCs until today. Analyzing calcification on the background of 9p21 resulted in the cognition that a loss of the 9p21 risk locus or SNPs in the risk region lead to an increased risk of calcification and therefore of suffering from CAC.

4.5 Outlook

Further experiments need to be performed to unravel the mechanisms underlying the increased calcification in 9p21 risk cells and later patients. First, the present SMC phenotype available after the differentiation of iPSCs into VSMCs needs to be identified, which could be achieved by single cell RNA sequencing technology. Additionally, it might be of great interest to determine if there are differences in the ratio of contractile versus synthetic VSMCs after the differentiation of 9p21 R and NR cells. As mentioned before different phenotypes might be divergingly prone to calcification. This can be performed by establishing an SMC screening panel at the Institute that discriminates between contractile and synthetic VSMCS. In order to provide further robust data on calcification a more stable calcification protocol is of need. Certainly, the replacement of serum in the SMC medium will increase the efficiency and reproducibility of the calcification protocol as the inhibitory factors present in the serum are missing. Further, the usage of different coatings or abandonment of coatings in general may contribute to a better result in calcification efficiencies. RNA sequencing might also be useful to obtain insights on the processes taking place during calcification.

Furthermore, as indicated in the last section it is of great need to unravel the role of the ANRIL isoforms in calcification. First of all, it should be examined whether the iPSC-derived VSMCs of the R and the NR donor show different ratios of circANRIL to linANRIL. Various experiments might be needed to deeply investigate the physiological role the ANRIL isoforms play in the process of calcification. It could be an idea to investigate the application of different calcifying agents to detect the relevant calcification pathways that might be affected by ANRIL.

Finally, the role of the cell cycle regulators encoded close to the risk region could be examined. Different expression rates of cell cycle inhibitors and therefore differences in cell cycle progression might point towards currently unknown mechanisms.

This thesis mainly regarded vascular calcification as something negative. However, there is also the possibility that the increased calcification in risk patients would also lead to plaque stabilization (Finn Aloke V. et al., 2010). This would hinder the rupture of a plaque and therefore protect the patient from secondary events like stroke. It greatly depends on where physiologically the calcification takes place, in the plaque or in the media. As we examined only VSMC calcification we rather resembled media calcification and can therefore only comment on this process which has a rather negative outcome for patients, as the vessel walls stiffen.

All those additional aspects might help to understand how VSMCs phenotype might influence the calcification outcome, and clarify the role and mechanism the 9p21 risk locus and ANRIL have in the development of vascular calcification and CAC.

5. Literature

Adam, P.J., Regan, C.P., Hautmann, M.B., and Owens, G.K. (2000). Positive- and negative-acting Kruppel-like transcription factors bind a transforming growth factor beta control element required for expression of the smooth muscle cell differentiation marker SM22alpha in vivo. J. Biol. Chem. *275*, 37798–37806.

Aherrahrou, Z., and Schunkert, H. (2013). Genetics of atherosclerosis and vascular calcification go hand-in-hand. Atherosclerosis *228*, 325–326.

Alam, M., Kirton, J.P., Wilkinson, F.L., Towers, E., Sinha, S., Rouhi, M., Vizard, T.N., Sage, A.P., Martin, D., Ward, D.T., et al. (2009). Calcification is associated with loss of functional calcium-sensing receptor in vascular smooth muscle cells. Cardiovasc. Res. *81*, 260–268.

Alexander, M.R., and Owens, G.K. (2012). Epigenetic Control of Smooth Muscle Cell Differentiation and Phenotypic Switching in Vascular Development and Disease. Annu. Rev. Physiol. *74*, 13–40.

Alfrey, A.C. (2004). The role of abnormal phosphorus metabolism in the progression of chronic kidney disease and metastatic calcification. Kidney Int. *66*, S13–S17.

Alves, R.D., Eijken, M., van de Peppel, J., and van Leeuwen, J.P. (2014). Calcifying vascular smooth muscle cells and osteoblasts: independent cell types exhibiting extracellular matrix and biomineralization-related mimicries. BMC Genomics *15*.

Amann, K. (2008). Media Calcification and Intima Calcification Are Distinct Entities in Chronic Kidney Disease. Clin. J. Am. Soc. Nephrol. *3*, 1599–1605.

Ayoubi, S., Sheikh, S.P., and Eskildsen, T.V. (2017). Human induced pluripotent stem cell-derived vascular smooth muscle cells: differentiation and therapeutic potential. Cardiovasc. Res. *113*, 1282–1293.

Azechi, T., Sato, F., Sudo, R., and Wachi, H. (2014). 5-aza-2´-Deoxycytidine, a DNA Methyltransferase Inhibitor, Facilitates the Inorganic Phosphorus-Induced Mineralization of Vascular Smooth Muscle Cells. J. Atheroscler. Thromb. *advpub*.

Balderman, J.A.F., Lee, H.-Y., Mahoney, C.E., Handy, D.E., White, K., Annis, S., Lebeche, D., Hajjar, R.J., Loscalzo, J., and Leopold, J.A. (2012). Bone morphogenetic protein-2 decreases microRNA-30b and microRNA-30c to promote vascular smooth muscle cell calcification. J. Am. Heart Assoc. *1*, e003905.

Banerjee, A. (2012). A review of family history of cardiovascular disease: risk factor and research tool. Int. J. Clin. Pract. *66*, 536–543.

Bansal, V.K. (1990). Serum Inorganic Phosphorus. In Clinical Methods: The History, Physical, and Laboratory Examinations, H.K. Walker, W.D. Hall, and J.W. Hurst, eds. (Boston: Butterworths), p.

Beamish, J.A., He, P., Kottke-Marchant, K., and Marchant, R.E. (2010). Molecular Regulation of Contractile Smooth Muscle Cell Phenotype: Implications for Vascular Tissue Engineering. Tissue Eng. Part B Rev. *16*, 467–491.

Björkegren, J.L.M., Kovacic, J.C., Dudley, J.T., and Schadt, E.E. (2015). Genome-Wide Significant Loci: How Important Are They? J. Am. Coll. Cardiol. *65*, 830–845.

Boyer, L.A., Lee, T.I., Cole, M.F., Johnstone, S.E., Levine, S.S., Zucker, J.P., Guenther, M.G., Kumar, R.M., Murray, H.L., Jenner, R.G., et al. (2005). Core Transcriptional Regulatory Circuitry in Human Embryonic Stem Cells. Cell *122*, 947–956.

Brady, K., Dickinson, S.C., Guillot, P.V., Polak, J., Blom, A.W., Kafienah, W., and Hollander, A.P. (2014). Human Fetal and Adult Bone Marrow-Derived Mesenchymal Stem Cells Use Different Signaling Pathways for the Initiation of Chondrogenesis. Stem Cells Dev. *23*, 541–554.

Burton, P.R., Clayton, D.G., Cardon, L.R., Craddock, N., Deloukas, P., Duncanson, A., Kwiatkowski, D.P., McCarthy, M.I., Ouwehand, W.H., Samani, N.J., et al. (2007). Genome-wide association study of 14,000 cases of seven common diseases and 3,000 shared controls. Nature *447*, 661–678.

Byon, C.H., Javed, A., Dai, Q., Kappes, J.C., Clemens, T.L., Darley-Usmar, V.M., McDonald, J.M., and Chen, Y. (2008). Oxidative stress induces vascular calcification through modulation of the osteogenic transcription factor Runx2 by AKT signaling. J. Biol. Chem. *283*, 15319–15327.

Chen, I.Y., Matsa, E., and Wu, J.C. (2016). Induced pluripotent stem cells: at the heart of cardiovascular precision medicine. Nat. Rev. Cardiol. *13*, 333–349.

Cheung, C., Bernardo, A.S., Pedersen, R.A., and Sinha, S. (2014). Directed differentiation of embryonic origin–specific vascular smooth muscle subtypes from human pluripotent stem cells. Nat. Protoc. *9*, 929–938.

Dash, B.C., Jiang, Z., Suh, C., and Qyang, Y. (2015). Induced Pluripotent Stem Cell-derived Vascular Smooth Muscle Cells: Methods and Application. Biochem. J. *465*, 185–194.

Dash, B.C., Levi, K., Schwan, J., Luo, J., Bartulos, O., Wu, H., Qiu, C., Yi, T., Ren, Y., Campbell, S., et al. (2016). Tissue-Engineered Vascular Rings from Human iPSC-Derived Smooth Muscle Cells. Stem Cell Rep. *7*, 19–28.

Demer, L.L., Watson, K.E., and Boström, K. (1994). Mechanism of calcification in atherosclerosis. Trends Cardiovasc. Med. *4*, 45–49.

Doherty, T.M., Asotra, K., Fitzpatrick, L.A., Qiao, J.-H., Wilkin, D.J., Detrano, R.C., Dunstan, C.R., Shah, P.K., and Rajavashisth, T.B. (2003). Calcification in atherosclerosis: Bone biology and chronic inflammation at the arterial crossroads. Proc. Natl. Acad. Sci. U. S. A. *100*, 11201–11206.

Erdmann, J., Kessler, T., Munoz Venegas, L., and Schunkert, H. (2018). A decade of genome-wide association studies for coronary artery disease: the challenges ahead. Cardiovasc. Res. *114*, 1241–1257.

Feng, S., Gao, L., Zhang, D., Tian, X., Kong, L., Shi, H., Wu, L., Huang, Z., Du, B., Liang, C., et al. (2019). MiR-93 regulates vascular smooth muscle cell proliferation, and neointimal formation through targeting Mfn2. Int. J. Biol. Sci. *15*, 2615–2626.

Finn Aloke V., Nakano Masataka, Narula Jagat, Kolodgie Frank D., and Virmani Renu (2010). Concept of Vulnerable/Unstable Plaque. Arterioscler. Thromb. Vasc. Biol. *30*, 1282–1292.

Forlino, A., Cabral, W.A., Barnes, A.M., and Marini, J.C. (2011). New Perspectives on Osteogenesis Imperfecta. Nat. Rev. Endocrinol. *7*, 540–557.

Gaj, T., Gersbach, C.A., and Barbas, C.F. (2013). ZFN, TALEN, and CRISPR/Cas-based methods for genome engineering. Trends Biotechnol. *31*, 397–405.

Giachelli, C.M. (2009). The emerging role of phosphate in vascular calcification. Kidney Int. *75*, 890–897.

Gomez, D., and Owens, G.K. (2012). Smooth muscle cell phenotypic switching in atherosclerosis. Cardiovasc. Res. *95*, 156–164.

Hanna, J.H., Saha, K., and Jaenisch, R. (2010). Pluripotency and Cellular Reprogramming: Facts, Hypotheses, Unresolved Issues. Cell *143*, 508–525.

Handschick, K. (2014). Cyclin-dependent kinase (CDK) 6: ein molekularer Schalter zwischen dem Zellzyklus und der inflammatorischen Genregulation. (Diss.), Justus-Liebig-Universität Gießen

Hansson, G.K., and Libby, P. (2006). The immune response in atherosclerosis: a double-edged sword. Nat. Rev. Immunol. *6*, 508–519.

Hayashi, K., Shibata, K., Morita, T., Iwasaki, K., Watanabe, M., and Sobue, K. (2004). Insulin Receptor Substrate-1/SHP-2 Interaction, a Phenotype-dependent Switching Machinery of Insulin-like Growth Factor-I Signaling in Vascular Smooth Muscle Cells. J. Biol. Chem. *279*, 40807–40818.

Helgadottir, A., Thorleifsson, G., Manolescu, A., Gretarsdottir, S., Blondal, T., Jonasdottir, A., Jonasdottir, A., Sigurdsson, A., Baker, A., Palsson, A., et al. (2007). A common variant on chromosome 9p21 affects the risk of myocardial infarction. Science *316*, 1491–1493.

Heusch, G. (1997). 'Myocardial hibernation'—questions and controversies. Cardiovasc. Res. *36*, 301–309.

Hirschhorn, J.N., and Daly, M.J. (2005). Genome-wide association studies for common diseases and complex traits. Nat. Rev. Genet. *6*, 95–108.

Holdt, L.M., and Teupser, D. (2012). Recent Studies of the Human Chromosome 9p21 Locus, Which Is Associated With Atherosclerosis in Human Populations. Arterioscler. Thromb. Vasc. Biol. *32*, 196–206.

Holdt, L.M., and Teupser, D. (2013). From genotype to phenotype in human atherosclerosis - recent findings. Curr. Opin. Lipidol. *24*, 410–418.

Holdt, L.M., Stahringer, A., Sass, K., Pichler, G., Kulak, N.A., Wilfert, W., Kohlmaier, A., Herbst, A., Northoff, B.H., Nicolaou, A., et al. (2016). Circular non-coding RNA ANRIL modulates ribosomal RNA maturation and atherosclerosis in humans. Nat. Commun. *7*.

Horii, T., and Hatada, I. (2016). Production of genome-edited pluripotent stem cells and mice by CRISPR/Cas [Review]. Endocr. J. *63*, 213–219.

Hsu, P.D., Lander, E.S., and Zhang, F. (2014). Development and Applications of CRISPR-Cas9 for Genome Engineering. Cell *157*, 1262–1278.

Jaenisch, R., and Young, R. (2008). Stem Cells, the Molecular Circuitry of Pluripotency and Nuclear Reprogramming. Cell *132*, 567–582.

Jahnen-Dechent Willi, Heiss Alexander, Schäfer Cora, Ketteler Markus, and Towler Dwight A. (2011). Fetuin-A Regulation of Calcified Matrix Metabolism. Circ. Res. *108*, 1494–1509.

Jono, S., McKee, M.D., Murry, C.E., Shioi, A., Nishizawa, Y., Mori, K., Morii, H., and Giachelli, C.M. (2000a). Phosphate Regulation of Vascular Smooth Muscle Cell Calcification. Circ. Res. *87*, e10–e17.

Jono, S., Peinado, C., and Giachelli, C.M. (2000b). Phosphorylation of Osteopontin Is Required for Inhibition of Vascular Smooth Muscle Cell Calcification. J. Biol. Chem. *275*, 20197–20203.

Kim, J.B., Deluna, A., Mungrue, I.N., Vu, C., Pouldar, D., Civelek, M., Orozco, L., Wu, J., Wang, X., Charugundla, S., et al. (2012). Effect of 9p21.3 Coronary Artery Disease Locus Neighboring Genes on Atherosclerosis in MiceCLINICAL PERSPECTIVE. Circulation *126*, 1896–1906.

Lanzer, P., Boehm, M., Sorribas, V., Thiriet, M., Janzen, J., Zeller, T., St Hilaire, C., and Shanahan, C. (2014). Medial vascular calcification revisited: review and perspectives. Eur. Heart J. *35*, 1515–1525.

Libby, P., and Theroux, P. (2005). Pathophysiology of Coronary Artery Disease. Circulation *111*, 3481–3488.

Libby, P., Ridker, P.M., and Hansson, G.K. (2009). Inflammation in Atherosclerosis: From Pathophysiology to Practice. J. Am. Coll. Cardiol. *54*, 2129–2138.

Lin, M.-E., Chen, T., Leaf, E.M., Speer, M.Y., and Giachelli, C.M. (2015). Runx2 Expression in Smooth Muscle Cells Is Required for Arterial Medial Calcification in Mice. Am. J. Pathol. *185*, 1958–1969.

Liu, R., Leslie, K.L., and Martin, K.A. (2015). Epigenetic regulation of smooth muscle cell plasticity. Biochim. Biophys. Acta BBA - Gene Regul. Mech. *1849*, 448–453.

Lo Sardo, V., Chubukov, P., Ferguson, W., Kumar, A., Teng, E.L., Duran, M., Zhang, L., Cost, G., Engler, A.J., Urnov, F., et al. (2018). Unveiling the Role of the Most Impactful Cardiovascular Risk Locus through Haplotype Editing. Cell.

Lutgens, S.P.M., Cleutjens, K.B.J.M., Daemen, M.J.A.P., and Heeneman, S. (2007). Cathepsin cysteine proteases in cardiovascular disease. FASEB J. *21*, 3029–3041.

M Drab, H.H. (1997). From totipotent embryonic stem cells to spontaneously contracting smooth muscle cells: A retinoic acid and db-cAMP in vitro differentiation model. FASEB J. Off. Publ. Fed. Am. Soc. Exp. Biol. *11*, 905–915.

MacArthur, C.C., Fontes, A., Ravinder, N., Kuninger, D., Kaur, J., Bailey, M., Taliana, A., Vemuri, M.C., and Lieu, P.T. (2012). Generation of Human-Induced Pluripotent Stem Cells by a Nonintegrating RNA Sendai Virus Vector in Feeder-Free or Xeno-Free Conditions. Stem Cells Int. *2012*, e564612.

Maddocks, S., and Jenkins, R. (2017). Chapter 5 - Carrying Out Q-PCR. In Understanding PCR, (Boston: Academic Press), pp. 53–59.

Majesky, M.W. (2016). Vascular Smooth Muscle Cells. Arterioscler. Thromb. Vasc. Biol. *36*, e82–e86.

Mangino, M., and Spector, T. (2013). Understanding coronary artery disease using twin studies. Heart *99*, 373–375.

Marchand, M., Anderson, E.K., Phadnis, S.M., Longaker, M.T., Cooke, J.P., Chen, B., and Reijo Pera, R.A. (2014). Concurrent Generation of Functional Smooth Muscle and Endothelial Cells via a Vascular Progenitor. Stem Cells Transl. Med. *3*, 91–97.

Marenberg, M.E., Risch, N., Berkman, L.F., Floderus, B., and de Faire, U. (1994). Genetic susceptibility to death from coronary heart disease in a study of twins. N. Engl. J. Med. *330*, 1041–1046.

Mayer, B., Erdmann, J., and Schunkert, H. (2007). Genetics and heritability of coronary artery disease and myocardial infarction. Clin. Res. Cardiol. *96*, 1–7.

McPherson, R., and Tybjaerg-Hansen, A. (2016). Genetics of Coronary Artery Disease. Circ. Res. *118*, 564–578.

McPherson, R., Pertsemlidis, A., Kavaslar, N., Stewart, A., Roberts, R., Cox, D.R., Hinds, D.A., Pennacchio, L.A., Tybjaerg-Hansen, A., Folsom, A.R., et al. (2007). A Common Allele on Chromosome 9 Associated with Coronary Heart Disease. *316*, 5.

McQuillan, D.J., Richardson, M.D., and Bateman, J.F. (1995). Matrix deposition by a calcifying human osteogenic sarcoma cell line (SAOS-2). Bone *16*, 415–426.

Montalescot, G., Members, T.F., Sechtem, U., Achenbach, S., Andreotti, F., Arden, C., Budaj, A., Bugiardini, R., Crea, F., Cuisset, T., et al. (2013). 2013 ESC guidelines on the management of stable coronary artery disease. Eur. Heart J. *34*, 2949–3003.

Myers, R.H., Kiely, D.K., Cupples, L.A., and Kannel, W.B. (1990). Parental history is an independent risk factor for coronary artery disease: The Framingham Study. Am. Heart J. *120*, 963–969.

Myocardial Infarction Genetics and CARDIoGRAM Exome Consortia Investigators (2016). Coding Variation in ANGPTL4, LPL, and SVEP1 and the Risk of Coronary Disease. N. Engl. J. Med. *374*, 1134–1144.

Nabel, E.G., and Braunwald, E. (2012). A Tale of Coronary Artery Disease and Myocardial Infarction. N. Engl. J. Med. *366*, 54–63.

Owens, G.K., Kumar, M.S., and Wamhoff, B.R. (2004). Molecular Regulation of Vascular Smooth Muscle Cell Differentiation in Development and Disease. Physiol. Rev. *84*, 767–801.

Patel, M., and Yang, S. (2010). Advances in reprogramming somatic cells to induced pluripotent stem cells. Stem Cell Rev. Rep. *6*, 367–380.

Proudfoot, D., Skepper, J.N., Hegyi, L., Bennett, M.R., Shanahan, C.M., and Weissberg, P.L. (2000). Apoptosis Regulates Human Vascular Calcification In Vitro Evidence for Initiation of Vascular Calcification by Apoptotic Bodies. Circ. Res. *87*, 1055–1062.

Ramirez, J.-M., Gerbal-Chaloin, S., Milhavet, O., Qiang, B., Becker, F., Assou, S., Lemaître, J.-M., Hamamah, S., and De Vos, J. (2011). Brief Report: Benchmarking Human Pluripotent Stem Cell Markers During Differentiation Into the Three Germ Layers Unveils a Striking Heterogeneity: All Markers Are Not Equal. STEM CELLS *29*, 1469–1474.

Rao, M.S., and Malik, N. (2012). Assessing iPSC reprogramming methods for their suitability in translational medicine. J. Cell. Biochem. *113*, 3061–3068.

Rath, D., Amlinger, L., Rath, A., and Lundgren, M. (2015). The CRISPR-Cas immune system: Biology, mechanisms and applications. Biochimie *117*, 119–128.

Rensen, S.S.M., Doevendans, P.A.F.M., and van Eys, G.J.J.M. (2007). Regulation and characteristics of vascular smooth muscle cell phenotypic diversity. Neth. Heart J. *15*, 100–108.

Reynolds, J.L., Joannides, A.J., Skepper, J.N., McNair, R., Schurgers, L.J., Proudfoot, D., Jahnen-Dechent, W., Weissberg, P.L., and Shanahan, C.M. (2004). Human vascular smooth muscle cells undergo vesicle-mediated calcification in response to changes in extracellular calcium and phosphate concentrations: a potential mechanism for accelerated vascular calcification in ESRD. J. Am. Soc. Nephrol. JASN *15*, 2857–2867.

Riches, K., Angelini, T., Mudhar, G., Kaye, J., Clark, E., Bailey, M., Sohrabi, S., Korossis, S., Walker, P., Scott, D., et al. (2013). Exploring smooth muscle phenotype and function in a bioreactor model of abdominal aortic aneurysm. J. Transl. Med. *11*, 208.

Richter, C., Chang, J.T., and Fineran, P.C. (2012). Function and Regulation of Clustered Regularly Interspaced Short Palindromic Repeats (CRISPR) / CRISPR Associated (Cas) Systems. Viruses *4*, 2291–2311.

Risch, N., and Merikangas, K. (1996). The future of genetic studies of complex human diseases. Science *273*, 1516–1517.

Samani, N.J., Erdmann, J., Hall, A.S., Hengstenberg, C., Mangino, M., Mayer, B., Dixon, R.J., Meitinger, T., Braund, P., Wichmann, H.-E., et al. (2007). Genomewide Association Analysis of Coronary Artery Disease. N. Engl. J. Med. *357*, 443–453.

Sander, J.D., and Joung, J.K. (2014). CRISPR-Cas systems for editing, regulating and targeting genomes. Nat. Biotechnol. *32*, 347–355.

Schunkert, H., Erdmann, J., and Samani, S.N.J. (2019). CARDIoGRAM celebrates its 10th Anniversary. Eur. Heart J. *40*, 1664–1666.

van Setten, J., Isgum, I., Smolonska, J., Ripke, S., de Jong, P.A., Oudkerk, M., de Koning, H., Lammers, J.-W.J., Zanen, P., Groen, H.J.M., et al. (2013). Genome-wide association study of coronary and aortic calcification implicates risk loci for coronary artery disease and myocardial infarction. Atherosclerosis *228*, 400–405.

Singhal, N., Graumann, J., Wu, G., Araúzo-Bravo, M.J., Han, D.W., Greber, B., Gentile, L., Mann, M., and Schöler, H.R. (2010). Chromatin-Remodeling Components of the BAF Complex Facilitate Reprogramming. Cell *141*, 943–955.

Sinha, S., Iyer, D., and Granata, A. (2014). Embryonic origins of human vascular smooth muscle cells: implications for in vitro modeling and clinical application. Cell. Mol. Life Sci. *71*, 2271–2288.

Strong, A., and Musunuru, K. (2017). Genome editing in cardiovascular diseases. Nat. Rev. Cardiol. *14*, 11–20.

Strong, M., Farrugia, A., and Rebulla, P. (2009). Stem cell and cellular therapy developments. Biologicals *37*, 103–107.

Sun, Y., Byon, C.H., Yuan, K., Chen, J., Mao, X., Heath, J.M., Javed, A., Zhang, K., Anderson, P.G., and Chen, Y. (2012). Smooth Muscle Cell–Specific Runx2 Deficiency Inhibits Vascular CalcificationNovelty and Significance. Circ. Res. *111*, 543–552.

Takahashi, K., Tanabe, K., Ohnuki, M., Narita, M., Ichisaka, T., Tomoda, K., and Yamanaka, S. (2007). Induction of Pluripotent Stem Cells from Adult Human Fibroblasts by Defined Factors. Cell *131*, 861–872.

The CARDIoGRAMplusC4D Consortium (2013). Large-scale association analysis identifies new risk loci for coronary artery disease. Nat. Genet. *45*, 25–33.

Thompson, B., and Towler, D.A. (2012). Arterial calcification and bone physiology: role of the bone-vascular axis. Nat. Rev. Endocrinol. *8*, 529–543.

Thomson, J.A., Itskovitz-Eldor, J., Shapiro, S.S., Waknitz, M.A., Swiergiel, J.J., Marshall, V.S., and Jones, J.M. (1998). Embryonic Stem Cell Lines Derived from Human Blastocysts. Science *282*, 1145–1147.

Thomson, M., Liu, S.J., Zou, L.-N., Smith, Z., Meissner, A., and Ramanathan, S. (2011). Pluripotency Factors in Embryonic Stem Cells Regulate Differentiation into Germ Layers. Cell *145*, 875–889.

Tintut, Y., Patel, J., Parhami, F., and Demer, L.L. (2000). Tumor Necrosis Factor-α Promotes In Vitro Calcification of Vascular Cells via the cAMP Pathway. Circulation *102*, 2636–2642.

Tintut, Y., Alfonso, Z., Saini, T., Radcliff, K., Watson, K., Boström, K., and Demer, L.L. (2003). Multilineage Potential of Cells From the Artery Wall. Circulation *108*, 2505–2510.

Topol, E.J., Murray, S.S., and Frazer, K.A. (2007). The Genomics Gold Rush. JAMA *298*, 218–221.

Torpy, J.M., Burke, A.E., and Glass, R.M. (2009). Coronary Heart Disease Risk Factors. JAMA *302*, 2388–2388.

Trillhaase, A., Haferkamp, U., Rangnau, A., Märtens, M., Schmidt, B., Trilck, M., Seibler, P., Aherrahrou, R., Erdmann, J., and Aherrahrou, Z. (2018). Differentiation of human iPSCs into VSMCs and generation of VSMC-derived calcifying vascular cells. Stem Cell Res. *31*, 62–70.

Tziakas Dimitrios N., Chalikias Georgios, Pavlaki Maria, Kareli Dimitra, Gogiraju Rajinikanth, Hubert Astrid, Böhm Elsa, Stamoulis Petros, Drosos Ioannis, Kikas Petros, et al. (2019). Lysed Erythrocyte Membranes Promote Vascular Calcification. Circulation *139*, 2032–2048.

Vasuri, F., Fittipaldi, S., and Pasquinelli, G. (2014). Arterial calcification: Finger-pointing at resident and circulating stem cells. World J. Stem Cells *6*, 540–551.

Villa-Bellosta, R., and Sorribas, V. (2013). Prevention of Vascular Calcification by Polyphosphates and Nucleotides. Circ. J. *77*, 2145–2151.

Visel, A., Zhu, Y., May, D., Afzal, V., Gong, E., Attanasio, C., Blow, M.J., Cohen, J.C., Rubin, E.M., and Pennacchio, L.A. (2010). Targeted deletion of the 9p21 non-coding coronary artery disease risk interval in mice. Nature *464*, 409–412.

Wada, T., McKee, M.D., Steitz, S., and Giachelli, C.M. (1999). Calcification of Vascular Smooth Muscle Cell Cultures Inhibition by Osteopontin. Circ. Res. *84*, 166–178.

Wei, C., Liu, J., Yu, Z., Zhang, B., Gao, G., and Jiao, R. (2013). TALEN or Cas9 – Rapid, Efficient and Specific Choices for Genome Modifications. J. Genet. Genomics *40*, 281–289.

Wilson, P.W.F., D'Agostino, R.B., Levy, D., Belanger, A.M., Silbershatz, H., and Kannel, W.B. (1998). Prediction of Coronary Heart Disease Using Risk Factor Categories. Circulation *97*, 1837–1847.

Wobus, A.M., and Boheler, K.R. (2005). Embryonic Stem Cells: Prospects for Developmental Biology and Cell Therapy. Physiol. Rev. *85*, 635–678.

Xie, C.-Q., Huang, H., Wei, S., Song, L.-S., Zhang, J., Ritchie, R.P., Chen, L., Zhang, M., and Chen, Y.E. (2008). A Comparison of Murine Smooth Muscle Cells Generated from Embryonic versus Induced Pluripotent Stem Cells. Stem Cells Dev. *18*, 741–748.

Yang, H., Curinga, G., and Giachelli, C.M. (2004). Elevated extracellular calcium levels induce smooth muscle cell matrix mineralization in vitro11See Editorial by Towler, p. 2467. Kidney Int. *66*, 2293–2299.

Yu, J., Vodyanik, M.A., Smuga-Otto, K., Antosiewicz-Bourget, J., Frane, J.L., Tian, S., Nie, J., Jonsdottir, G.A., Ruotti, V., Stewart, R., et al. (2007). Induced pluripotent stem cell lines derived from human somatic cells. Science *318*, 1917–1920.

Zhao, Y., Vanhoutte, P.M., and Leung, S.W.S. (2015). Vascular nitric oxide: Beyond eNOS. J. Pharmacol. Sci. *129*, 83–94.

Zwergel, C., Schnekenburger, M., Sarno, F., Battistelli, C., Manara, M.C., Stazi, G., Mazzone, R., Fioravanti, R., Gros, C., Ausseil, F., et al. (2019). Identification of a novel quinoline-based DNA demethylating compound highly potent in cancer cells. Clin. Epigenetics *11*, 68.

6. Appendix

A. Script Python Analysis of Calcein images:

```
"""
Tobias Schöne, 23.07.2019
gets DAPI and green Fl. as TIF
give excel sheet with intensity of fluorescence and pixel count
normalized by DAPI Pixel count
To Do: delete [255 255 255] pixel
"""
import cv2
import numpy as np
import matplotlib.pyplot as plt
from openpyxl import load_workbook
import os
import datetime
today = str(datetime.date.today())
today = today.replace('-', '')
time = str(datetime.datetime.now().time()).replace(":", '_')
time = time[0:time.find('.')]
storage = "//storage.iieg.uni-luebeck.de/public/6_Keyence/Anja/Calcein/Calcein Quantifizierung/"
channels = {"CH1": ["Dapi", 0],
            "CH2": ["Calc", 1]}
threshold_dapi = 35
threshold_calein = 20
wb = load_workbook('./EMPTY.xlsx')
ws = wb.active  # sheet has to be active
ws.cell(1, 1).value = "Dateiname"
ws.cell(1, 2).value = "Intensity\n(raw DAPI)"
ws.cell(1, 3).value = "Pixel count DAPI\n(I(DAPI)/count(DAPI)"
ws.cell(1, 4).value = "norm DAPI"
ws.cell(1, 5).value = "Intensity\n(raw Calcein)"
ws.cell(1, 6).value = "Pixel count Calcein"
ws.cell(1, 7).value = "norm Calcein\n(I(Calcein)/count(DAPI))"
""" get file names """
file_array = []
```

```
for file in os.listdir(storage):
    if ".TIF" in file or ".tif" in file:
        file_array.append(file)
    pass
file_array = sorted(file_array)
print('Files:', len(file_array))
for elem in file_array:
    print(elem)
print("\n\n")
counter = 2
for file in file_array:
    if ".TIF" in file or ".tif" in file:
        image = cv2.imread(storage + file)
        plt.imshow(image)
        # plt.show()
        image_temp = np.asarray(image)
        if "CH1" in file:
            print(counter)
            print(file)
            image_temp[image_temp < threshold_dapi] = 0
            sum_ = np.sum(image_temp)
            pixel_count = np.count_nonzero(image_temp)
            ws.cell(counter, 1).value = file.replace("_CH1.TIF", "")
            ws.cell(counter, 2).value = sum_
            ws.cell(counter, 3).value = pixel_count
            ws.cell(counter, 4).value = round((sum_/pixel_count), 2)
            print("Intensity", sum_, "Pixel count", pixel_count, sum_/pixel_count)
        if "CH2" in file:
            print(file)
            image_temp[image_temp < threshold_calein] = 0
            sum_ = np.sum(image_temp)
            pixel_count_2 = np.count_nonzero(image_temp)
            ws.cell(counter, 5).value = sum_
            ws.cell(counter, 6).value = pixel_count_2
            ws.cell(counter, 7).value = round((sum_/pixel_count), 2)
            counter += 1
            print("Intensity", sum_, "Pixel count", pixel_count_2, sum_/pixel_count, "\n\n")
```

```
wb.save(storage + "%s_Calcein_Quantification.xlsx" % today)
wb.close()
```

B. Analysis of the changes in ALPL, COL1A2 and DNMT expression in GM vs 18i-3-6 cells:

18i-3-6 and GM iPSCs were analyzed regarding their expression of COL1A2, ALPL, and DNMT1. ALPL expression was not significantly changed between both cell lines. COL1A2 and DNMT1 showed statistical differences between both cell lines, however, the difference is biologically neglectable as the changes in expression fold change are too small.

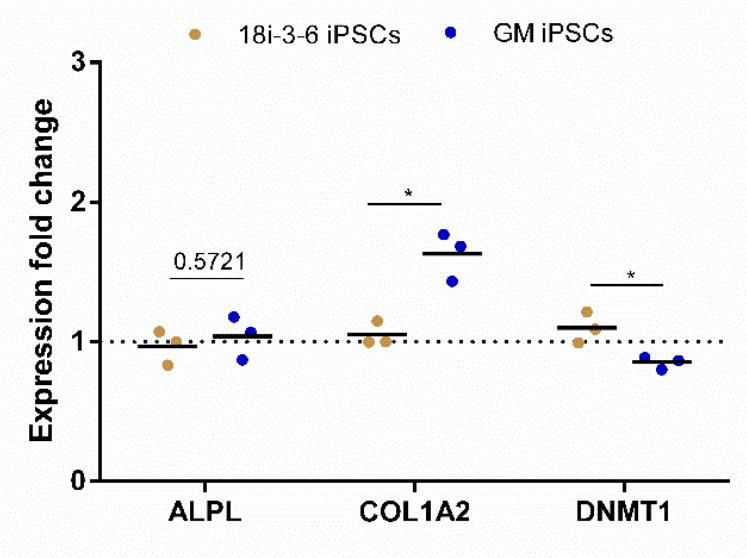

In the case of VSMCs however, we see significantly increased expression of ALPL and DNMT1 in GM cells, but highly decreased expression in COL1A2 in GM cells compared to 18i-3-6 cells.

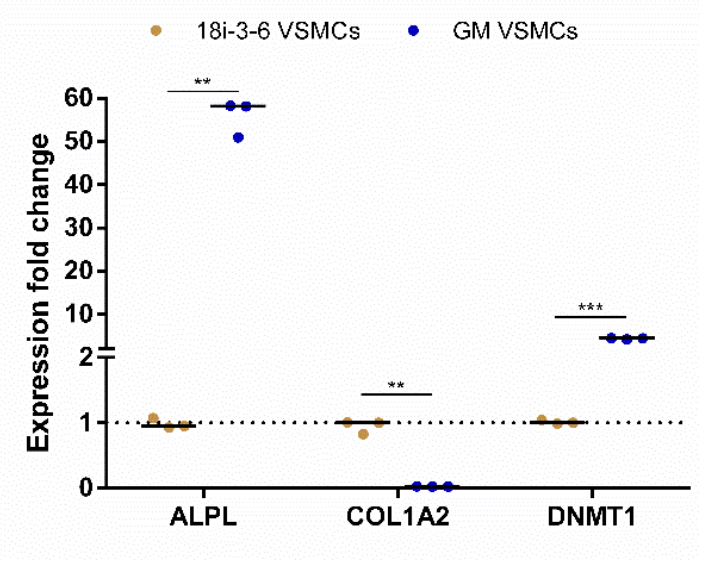

C. Overview of 163 CAD risk loci identified in GWAS

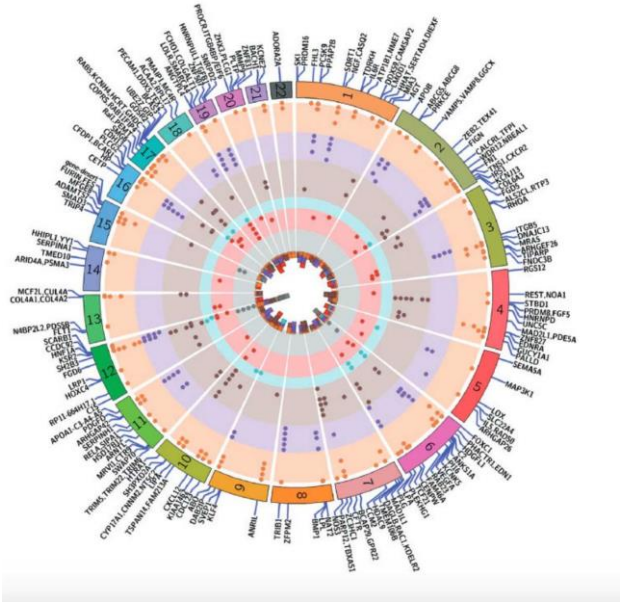

163 GWAS loci associated with CAD (Erdmann & Moretti, 2019).